Steffen Alvermann

Effective Viscoelastic Behaviour of Cellular Auxetic Materials

Monographic Series TU Graz

Computation in Engineering and Science

Series Editors

G. Brenn	Institute of Fluid Mechanics and Heat Transfer
G.A. Holzapfel	Institute of Biomechanics
M. Schanz	Institute of Applied Mechanics
W. Sextro	Institute of Mechanics
O. Steinbach	Institute of Computational Mathematics

Monographic Series TU Graz

Computation in Engineering and Science   Volume 1

Steffen Alvermann

Effective Viscoelastic Behaviour of Cellular Auxetic Materials

---

This work is based on the dissertation *Effective Viscoelastic Behaviour of Cellular Auxetic Materials*, presented by S. Alvermann at Graz University of Technology, Institute of Applied Mechanics in January 2007.
Supervisor: M. Schanz (Graz University of Technology)
Reviewer: M. Schanz (Graz University of Technology), G. E. Stavroulakis (Technical University of Crete)

Bibliographic information published by Die Deutsche Bibliothek.
Die Deutsche Bibliothek lists this publication in the Deutsche Nationalbibliografie; detailed bibliographic data are available at http://dnb.ddb.de.

© 2008 Verlag der Technischen Universität Graz

Cover photo	Vier-Spezies-Rechenmaschine by courtesy of the Gottfried Wilhelm Leibniz Bibliothek – Niedersächsische Landesbibliothek Hannover
Layout	Wolfgang Karl, TU Graz / Universitätsbibliothek
Printed	by TU Graz / Büroservice

Verlag der Technischen Universität Graz
www.ub.tugraz.at/Verlag
ISBN: 978-3-902465-92-4

This work is subject to copyright. All rights are reserved, whether the whole or part of the material is concerned, specifically the rights of reprinting, translation, reproduction on microfilm and data storage and processing in data bases. For any kind of use the permission of the Verlag der Technischen Universität Graz must be obtained.

Abstract

This work is concerned with the calculation of effective, macroscopic material parameters of materials with an inhomogeneous microstructure. On the microscopic scale, the calculation of a representative volume element of the material is done taking dynamical effects into account. This makes it possible to study damping effects on the macroscopic scale. The microstructures to be analyzed are mainly composed of trusses. They are calculated with a newly developed boundary element formulation, which delivers analytical exact results. A special interest is put on microstructures which, because of their deformation mechanism, cause a negative Poisson's ratio of a material on the macroscopic scale (auxetic materials). The calculation of adequate macroscopic material parameters is done with different optimization techniques. Beside the classical gradient-based optimization procedures, also softcomputing methods like Genetic Algorithms and Neural Networks are used. A number of numerical examples are presented where effective viscoelastic material parameters are calculated. The Genetic Algorithm turned out to deliver the most reliable results in the homogenization process, wheras the gradient-based methods may fail due to the existence of local minima in the optimization function.

Zusammenfassung

Die vorliegende Arbeit behandelt die Berechnung effektiver, makroskopischer Eigenschaften von Materialien mit inhomogener Mikrostruktur. Auf mikroskopischer Ebene wird dabei die Berechnung eines repräsentativen Volumenelementes des zu untersuchenden Materials in der Dynamik durchgeführt, um Effekte wie beispielweise die innere Dämpfung des makroskopischen Materials zu erfassen. Die zu untersuchenden Mikrostrukturen sind meist einfache Balkentragwerke, die mit Hilfe einer neuentwickelten Randelementformulierung analytisch exakt berechnet werden. In der vorliegenden Arbeit interessieren insbesondere solche Strukturen, die durch ihre mikroskopische Kinematik negative Querkontraktionszahlen auf makroskopischer Ebene verursachen (auxetische Materialien). Die Berechnung effektiver Materialparameter auf makroskopischer Ebene erfolgt mit Hilfe verschiedener Optimierungsverfahren, wobei neben klassischen Gradientenverfahren auch Softcomputing-Methoden wie Genetische Algorithmen und Neuronale Netze zum Einsatz kommen. Eine Reihe von Beispielrechnungen werden vorgestellt, bei denen effektive viskoelastische Materialparameter verschiedener Mikrostrukturen berechnet werden. Der Genetische Algorithmus liefert dabei die zuverlässigsten Ergebnisse, wohingegen die klassischen Gradientenverfahren teilweise aufgrund lokaler Minima in der Optimierungsfunktion fehlschlagen.

CONTENTS

1 INTRODUCTION

Nearly all common materials undergo a transverse contraction when being stretched in one direction and a transverse expansion when being compressed. The magnitude of this transverse deformation is governed by the Poisson's ratio. Poisson's ratios for various materials are approximately 0.5 for rubbers, 0.3 for common steels, 0.1 to 0.4 for cellular solids such as typical polymer foams, and nearly 0 for cork. These materials, possessing a positive Poisson's ratio, contract laterally when stretched and expand laterally when compressed. Negative Poisson's ratios are theoretically permissible but have not been observed in real materials. Materials with a negative Poisson's ratio behave counter-intuitively, meaning that they become thicker in their perpendicular directions when being stretched. At first sight, this seems impossible because one thinks that the volume of the material must be conserved. However, there is no law of conservation of volume and in fact, all materials with a Poisson's ratio which differs from 0.5 do not 'conserve volume'.

Materials with a negative Poisson's ratio are expected to have interesting mechanical properties such as high energy absorption and fracture resistance which may be useful in applications such as packing material, knee and elbow pads, robust shock absorbing material, filters or sponge mops. Nevertheless, until now, no industrial applications have been realized in terms of products which are ready for mass production. However, a considerable number of patents has been given, which clearly shows the interest of industry in auxetic materials. As an example, the manufacturing process of an auxetic polymeric material was patented in US Patent 6878320 [29]. An example of the practical application of a particular value of Poisson's ratio is the cork of a wine bottle. The cork must be easily inserted and removed, yet it also must withstand the pressure from within the bottle. Rubber, with a Poisson's ratio of 0.5, could not be used for this purpose because it would expand when being compressed into the neck of the bottle and would jam. Cork, by contrast, with a Poisson's ratio of nearly zero, is ideal in this application.

From a continuum mechanics point of view, there is no restriction for Poisson's ratio to be positive. This is known for a long time, but nobody made an effort to investigate this behavior. In fact, the earliest example for a material with a negative Poisson's ratio was published in *Science* in 1987, 'Foam structures with a negative Poisson's ratio' by R.S. LAKES [34]. LAKES converted a synthetic foam from its conventional, positive Poisson's ratio state to one having a negative Poisson's ratio by a relatively simple process [6]. In fact, the fabrication process is published in the Internet in form of a 'cooking recipe' [33]. Since then several new negative Poisson's ratio materials have been developed and fabricated.

A negative Poisson's ratio effect can be explained with the microstructural characteristics of a material. Foams or composite structures having a specific microstructure exhibit this effect. Thus, when studying such materials it is necessary to 'bridge the length scales' or, in other words, to investigate a certain microstructure and try to obtain the behavior of it on a macroscopic scale. The problem of finding a micro-macro transition is subject of many publications. This may be due to the fact that nearly every material exhibits a certain microstructure. On the microscopic scale of a material, one can find heterogeneties such as cracks, inclusions, fibres or others while one a macroscopic scale, the material may be modeled perfectly isotropic. Thus, the bridge between microscopic and macroscopic scale was always of great interest for researchers - either one was interested in finding macroscopic properties of a material with a certain microstructure (homogenization) [37] or there was a need for a microstructural explanation of a macroscopic phenomena (localization). Most papers recently published in the context of micro-macro considerations are concerned with the latter problem, in particular there exist many publications which are concerned with crack identification and the micromechanical implications [49]. In the scope of this work, however, the attention is focused on the homogenization problem. The aim is to predict macroscopic material parameters of specific microstructures which exhibit a negative Poisson's ratio. Since it is expected that such materials have good damping characteristics, the homogenization is done in a dynamic formulation. Dynamic formulation, in this context, means that material parameters for a non-static constitutive equation are calculated. Therefore, it is necessary to make a dynamic calculation of the microstructure.

There is a big manifold of microstructures with a negative Poisson's ratio. The repertoire of such materials includes metallic foams, polymers or honeycomb-like structures. The essence of all these different microstructures is that the effect is always caused by a specific kinematic mechanism. In fact, the effect can easily be shown by certain mechanisms involving simple beam models. An example mechanism is given in Figure 1.1. The beams in this structure are rigidly connected. Due to their arrangement with the 're-entrant' corners at the joints, the whole structure expands when being subjected to a tensional load. Thus, a material with a microstructure of this type would have a negative Poisson's ratio. Although it is hardly possible to fabricate a microstructure with small beams of constant cross-section which are rigidly connected among each other, the ideal beam model is adequate to study the behavior. It must be true that if a certain effect of the microstructure causes a specific behavior on the macroscale, this effect is present at a perfect microstruc-

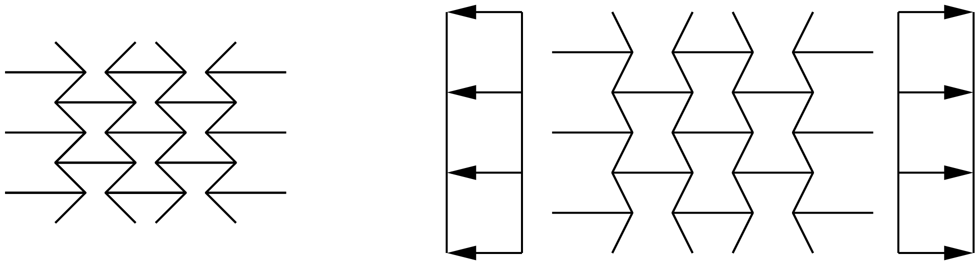

unloaded under tensional load

Figure 1.1: Microstructure of an auxetic material

ture as well as on a real, imperfect microstructure. Moreover, such an effect must be present in a three-dimensional application as well as in a two-dimensional case. Therefore, a calculation procedure for plane frameworks is needed in a first step. This problem is found very commonly in mechanics and has been solved by many authors. Yet, within this work, a new solution is introduced. The calculation of plane truss structures is solved by a boundary integral method, delivering an exact solution in frequency domain. Thus, the calculation of the microstructure is done as precise as possible.

With the results on the microscale, the homogenization is performed. Since homogenization techniques and the corresponding publications are centered on the calculation of static properties, a new method is proposed to calculate effective *dynamic* properties. The homogenization in the static case delivers (under certain assumptions) exact results. In frequency domain, however, this is not possible. For this reason, the homogenization is formulated as an optimization problem, the task is to 'try to find macroscopic material parameters which describe the micromechanical behavior as good as possible'. A number of different optimization procedures are used to solve the problem.

The work is arranged in the following way. Firstly, a presentation of the fundamental equations of continuum mechanics is given, focused on the constitutive equation in the elastic and viscoelastic case. The calculation of plane truss structures using a boundary integral method is presented in chapter 3. Next, the theory of homogenization is given. In chapter 5, the optimization procedure used for the homogenization are described and finally, example calculations are presented in the static and dynamic case.

Throughout this work, Einsteins summation convention is used, i.e., summation is performed if a term has repeated indices in a monomial.

2 CONTINUUM MECHANICS

In this chapter, the basic notations and equations for the description of a continuous medium are summarized. The main focus is put on the constitutive equations for elastic and viscoelastic material behavior. More detailed and extensive elaborations can be found in well-known textbooks, e.g. [19], [11].

2.1 Kinematics of deformations

The term deformation refers to a change in the shape of a continuum between a reference configuration and a current configuration. In the reference configuration, a particle of the continuum occupies a point P with the position vector $\mathbf{x}$ and in the current configuration, this particle occupies a point $\hat{P}$ with the position vector $\hat{\mathbf{x}}$ as shown in Figure 2.1. The difference of the position vectors $\mathbf{x}$ and $\hat{\mathbf{x}}$ is termed displacement, so the components of the displacement vector $\mathbf{u}$ are given by

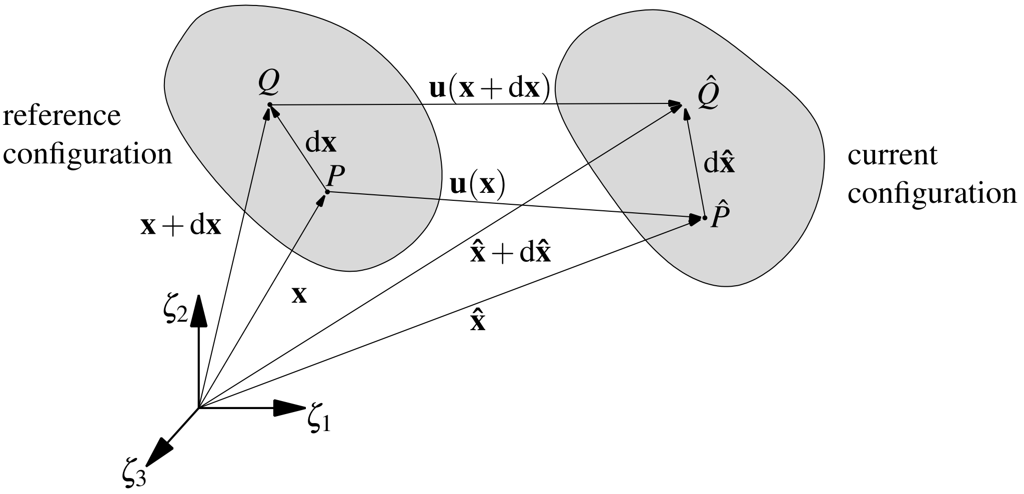

Figure 2.1: Deformation of a body

$$u_i = \hat{x}_i - x_i \quad . \tag{2.1}$$

A neighboring point Q has the position vector $\mathbf{x}+\mathrm{d}\mathbf{x}$ in the reference configuration and $\hat{\mathbf{x}}+\mathrm{d}\hat{\mathbf{x}}$ in the current configuration. The connecting line element $\mathrm{d}\mathbf{x}$ is mapped to the line element $\mathrm{d}\hat{\mathbf{x}}$ via

$$\mathrm{d}\hat{x}_i = F_{ij}\mathrm{d}x_j \quad . \tag{2.2}$$

F_{ij} are the components of the displacement gradient which are in a cartesian coordinate system

$$F_{ij} = u_{i,j} + \delta_{ij} \quad , \tag{2.3}$$

where $(\cdot)_{,i}$ denotes the partial derivative with respect to x_i and δ_{ij} is the Kronecker-delta (see Appendix A.1). To obtain a measurement for the deformation, the square difference in the magnitudes of the line elements are taken

$$\mathrm{d}\hat{x}_k \mathrm{d}\hat{x}_k - \mathrm{d}x_l \mathrm{d}x_l = 2\varepsilon_{ij} \mathrm{d}x_i \mathrm{d}x_j \quad . \tag{2.4}$$

The components ε_{ij} are the components of the so-called Green-Lagrangian strain tensor with

$$\varepsilon_{ij} = \frac{1}{2}\left(F_{ik}F_{kj} - \delta_{ij}\right) = \frac{1}{2}\left(u_{i,j} + u_{j,i} + u_{i,k}u_{k,j}\right) \quad . \tag{2.5}$$

In many technical applications only small deformations occur so that the term $u_{i,k}u_{k,j}$ can be neglected. Doing so, the infinitesimal strain tensor of linear continuum mechanics is obtained with

$$\varepsilon_{ij} = \frac{1}{2}\left(u_{i,j} + u_{j,i}\right) \quad . \tag{2.6}$$

From equation (2.6), it is obvious that the strain tensor is symmetric, i.e.,

$$\varepsilon_{ij} = \varepsilon_{ji} \quad . \tag{2.7}$$

2.2 Equilibrium

The balance of linear momentum postulates that the change of momentum of a body must be equal to the sum of all forces

$$\frac{\mathrm{d}}{\mathrm{d}t}\int\limits_{\hat{\Omega}} \hat{\rho}\dot{\hat{u}}_i \mathrm{d}V = \int\limits_{\hat{\Omega}} \hat{\rho}\hat{f}_i \mathrm{d}V + \int\limits_{\partial\hat{\Omega}} \hat{t}_i \mathrm{d}A \quad . \tag{2.8}$$

In equation (2.8), the density is denoted by ρ, f_i are the components of body forces acting inside the body $\hat{\Omega}$ and t_i are the components of forces acting on the boundary $\partial\hat{\Omega}$ of the body. All quantities refer to the current configuration, denoted by the ˆ symbol. $\hat{t}_i$ can be expressed by Cauchy's theorem

$$\hat{t}_i = \sigma_{ij}\hat{n}_j \tag{2.9}$$

where $\hat{n}_i$ denote the components of the outward normal vector of the surface of the body $\partial\hat{\Omega}$ and σ_{ij} are the components of the Cauchy stress tensor. Equation (2.9) can be inserted in (2.8) and the surface integral can be transformed into a volume integral via Green's theorem. Considering a single material point of body $\hat{\Omega}$ in the current configuration, the equation of dynamic equilibrium

$$\sigma_{ij,j} + \hat{\rho}\hat{f}_i = \rho\ddot{u}_i \tag{2.10}$$

is obtained. In static calculations, the body is not accelerated and thus, inertia terms are neglected. The $\ddot{u}_i$ are zero and equation (2.10) turns into the static equilibrium

$$\sigma_{ij,j} + \hat{\rho}\hat{f}_i = 0 \quad . \tag{2.11}$$

2.3 Constitutive equation

To be able to solve mechanical problems, the constitutive equations have to be added to the set of kinematic and balance equations. Within this work, the linear elastic and linear viscoelastic constitutive equations are used.

2.3.1 Linear elasticity

The linear elastic constitutive equation postulates a linear relationship between each component of stress and strain. As a prerequisite to this relationship, it is necessary to establish the existence of a strain energy density W that is a homogeneous quadratic function of the strain components. The strain energy density function should have coefficients such that $W \geq 0$ in order to insure the stability of the body, with $W(0) = 0$ corresponding to a natural or zero energy state. For Hooke's law it is

$$W = \frac{1}{2} C_{ijkl}\, \varepsilon_{ij}\, \varepsilon_{kl} \quad . \tag{2.12}$$

The constitutive equation, i.e., the stress-strain relation, is obtained by

$$\sigma_{ij} = \frac{\partial W}{\partial \varepsilon_{ij}}, \tag{2.13}$$

yielding the generalized Hooke's law

$$\sigma_{ij} = C_{ijkl} \varepsilon_{kl} \tag{2.14}$$

with the fourth order elasticity tensor C_{ijkl} which has $3^4 = 81$ components. Taking into account the symmetry of the stress and strain tensor, these 81 coefficients are reduced to 36 distinct elastic constants. From the strain energy density, the symmetric material tensor

$$C_{ijkl} = C_{klij} \tag{2.15}$$

obviously yields 21 independent elastic constants in the general case.

Introducing the notation

$$\boldsymbol{\sigma} = \begin{bmatrix} \sigma_{11} & \sigma_{12} & \sigma_{33} \\ & \sigma_{22} & \sigma_{23} \\ \text{sym.} & & \sigma_{33} \end{bmatrix} \rightarrow [\sigma_{11}\ \sigma_{22}\ \sigma_{33}\ \sigma_{12}\ \sigma_{23}\ \sigma_{13}]^T \tag{2.16}$$

for $\boldsymbol{\sigma}$ and

$$\boldsymbol{\varepsilon} = \begin{bmatrix} \varepsilon_{11} & \varepsilon_{12} & \varepsilon_{33} \\ & \varepsilon_{22} & \varepsilon_{23} \\ \text{sym.} & & \varepsilon_{33} \end{bmatrix} \rightarrow [\varepsilon_{11}\ \varepsilon_{22}\ \varepsilon_{33}\ 2\varepsilon_{12}\ 2\varepsilon_{23}\ 2\varepsilon_{13}]^T \tag{2.17}$$

for $\boldsymbol{\varepsilon}$, Hooke's law is often written in matrix form

$$\begin{bmatrix} \sigma_{11} \\ \sigma_{22} \\ \sigma_{33} \\ \sigma_{12} \\ \sigma_{23} \\ \sigma_{13} \end{bmatrix} = \begin{bmatrix} C_{1111} & C_{1122} & C_{1133} & C_{1112} & C_{1123} & C_{1113} \\ & C_{2222} & C_{2233} & C_{2212} & C_{2223} & C_{2213} \\ & & C_{3333} & C_{3312} & C_{3323} & C_{3313} \\ & & & C_{1212} & C_{1223} & C_{1213} \\ & \text{sym.} & & & C_{2323} & C_{2313} \\ & & & & & C_{1313} \end{bmatrix} \begin{bmatrix} \varepsilon_{11} \\ \varepsilon_{22} \\ \varepsilon_{33} \\ 2\varepsilon_{12} \\ 2\varepsilon_{23} \\ 2\varepsilon_{13} \end{bmatrix} \quad . \tag{2.18}$$

The matrix notation (also termed VOIGT's notation) for the tensor equation is commonly found in literature. Equation (2.18) is valid for the most general case of an anisotropic material, i.e., a material with different properties in different directions. If the material properties are equal in all directions, it is called isotropic and the number of independent constants of the material tensor reduces from 21 to 2. Using the Lame constants λ and μ, the stress strain relationship is

$$\begin{bmatrix} \sigma_{11} \\ \sigma_{22} \\ \sigma_{33} \\ \sigma_{12} \\ \sigma_{23} \\ \sigma_{13} \end{bmatrix} = \begin{bmatrix} 2\mu+\lambda & \lambda & \lambda & 0 & 0 & 0 \\ & 2\mu+\lambda & \lambda & 0 & 0 & 0 \\ & & 2\mu+\lambda & 0 & 0 & 0 \\ & & & \mu & 0 & 0 \\ & \text{sym.} & & & \mu & 0 \\ & & & & & \mu \end{bmatrix} \begin{bmatrix} \varepsilon_{11} \\ \varepsilon_{22} \\ \varepsilon_{33} \\ 2\varepsilon_{12} \\ 2\varepsilon_{23} \\ 2\varepsilon_{13} \end{bmatrix} \quad , \tag{2.19}$$

or in indical notation

$$\sigma_{ij} = 2\mu\varepsilon_{ij} + \lambda\delta_{ij}\varepsilon_{kk} \quad . \tag{2.20}$$

In between isotropic and anisotropic material, there exist various types of materials, for example orthotropic materials which have 9 independent constants. For isotropic materials, also other choices of 2 constants are possible, e.g., Young's modulus

$$E = \frac{\mu(2\mu+3\lambda)}{\mu+\lambda} \tag{2.21}$$

and Poisson's ratio

$$\nu = \frac{\lambda}{2(\mu+\lambda)} \quad . \tag{2.22}$$

Solving Hooke's law (2.19) for the strain and using equations (2.21) and (2.22), the complementary relationship

$$\begin{bmatrix} \varepsilon_{11} \\ \varepsilon_{22} \\ \varepsilon_{33} \\ 2\varepsilon_{12} \\ 2\varepsilon_{23} \\ 2\varepsilon_{13} \end{bmatrix} = \frac{1}{E} \begin{bmatrix} 1 & -\nu & -\nu & 0 & 0 & 0 \\ & 1 & -\nu & 0 & 0 & 0 \\ & & 1 & 0 & 0 & 0 \\ & & & (1+\nu) & 0 & 0 \\ & \text{sym.} & & & (1+\nu) & 0 \\ & & & & & (1+\nu) \end{bmatrix} \begin{bmatrix} \sigma_{11} \\ \sigma_{22} \\ \sigma_{33} \\ \sigma_{12} \\ \sigma_{23} \\ \sigma_{13} \end{bmatrix} \tag{2.23}$$

is obtained. In the general, anisotropic case, the complementary relationship is

$$\varepsilon = \mathbf{C}^{-1}\sigma \quad , \tag{2.24}$$

where the inverse of **C** is called flexibility tensor.

Meaning of Poisson's ratio

The physical meaning of the Poisson's ratio ν becomes clear if a body under an uniaxial stress condition is considered, i.e., only $\sigma_{11} \neq 0$. Using the first two rows of equation (2.23),

$$\nu = -\frac{E\varepsilon_{22}}{\sigma_{11}} = -\frac{\varepsilon_{22}}{\varepsilon_{11}} \tag{2.25}$$

is obtained. Figure 2.2 shows a body under this uniaxial stress state. The physical dimension in x_1 direction is ℓ, in x_2 and x_3 direction it is b. The longitudinal deformation is

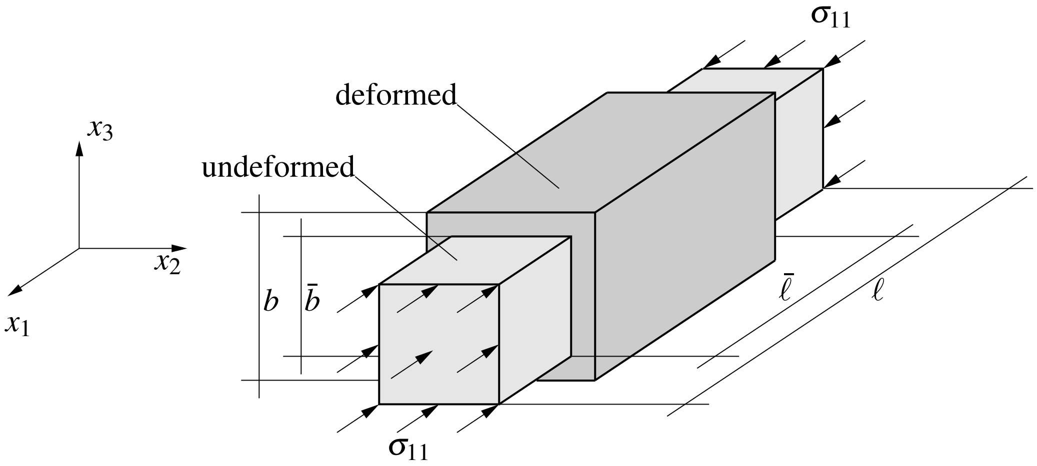

Figure 2.2: Physical meaning of Poisson's ratio

$$\frac{\ell - \bar{\ell}}{\ell} = \varepsilon_{11} \quad , \tag{2.26}$$

and the lateral deformation is

$$\frac{b - \bar{b}}{b} = \varepsilon_{22} \quad . \tag{2.27}$$

Thus, Poisson's ratio is the ratio of the lateral tensile strain to the longitudinal contractile strain.

Admissible values for Poisson's ratio

To derive a range of admissible values for Poisson's ratio of isotropic materials, it is useful to subdivide the stress and strain tensor into a hydrostatic and deviatoric part. The hydrostatic part

$$\boldsymbol{\varepsilon}^{\mathrm{hyd}} = \begin{bmatrix} \varepsilon_m & 0 & 0 \\ 0 & \varepsilon_m & 0 \\ 0 & 0 & \varepsilon_m \end{bmatrix} \quad , \qquad \varepsilon_m = \frac{\varepsilon_{ii}}{3} \tag{2.28}$$

describes a pure volume change and the deviatoric part

$$\boldsymbol{\varepsilon}^{\text{dev}} = \begin{bmatrix} \varepsilon_{11} - \varepsilon_m & \varepsilon_{12} & \varepsilon_{13} \\ \varepsilon_{12} & \varepsilon_{22} - \varepsilon_m & \varepsilon_{23} \\ \varepsilon_{13} & \varepsilon_{23} & \varepsilon_{33} - \varepsilon_m \end{bmatrix} \tag{2.29}$$

describes the change of shape of a body. The stress tensor is subdivided analogously. Using the shear modulus

$$G = \frac{E}{2(1+\nu)} \tag{2.30}$$

and the bulk modulus

$$K = \frac{E}{3(1-2\nu)} \tag{2.31}$$

as independent constants, Hooke's law for the two parts can be expressed with

$$\sigma_{kk}^{\text{hyd}} = 3K\varepsilon_{kk}^{\text{hyd}} \tag{2.32}$$

and

$$\sigma_{ij}^{\text{dev}} = 2G\varepsilon_{ij}^{\text{dev}} \quad . \tag{2.33}$$

The corresponding strain energy functions are

$$W^{\text{hyd}} = \frac{3K}{2}\varepsilon_{ii}^{\text{hyd}}\varepsilon_{jj}^{\text{hyd}} \tag{2.34}$$

and

$$W^{\text{dev}} = G\varepsilon_{ii}^{\text{dev}}\varepsilon_{jj}^{\text{dev}} \quad . \tag{2.35}$$

The strain energy function (2.12) is a homogeneous quadratic form, which means that for a deformed body, both $W^{\text{hyd}} > 0$ and $W^{\text{dev}} > 0$. From this,

$$G = \frac{E}{2(1+\nu)} > 0 \tag{2.36}$$

$$K = \frac{E}{3(1-2\nu)} > 0 \tag{2.37}$$

is obtained, resulting in

$$E > 0 \tag{2.38}$$

$$-1 < \nu < 0.5 \quad . \tag{2.39}$$

The restriction for Young's modulus to be positive could have been suspected from common sense. The possibility for Poisson's ratio to be negative, however, is against an engineer's intuition because it means that a material under compression becomes thinner in cross section.

For non-isotropic materials, Poisson's ratio has no bounds under the prerequisite of positive definiteness of strain energy density, as has been shown in a recent publication [54].

Two-dimensional elasticity Many problems in continuum mechanics can satisfactorily be treated in a two-dimensional theory. Two cases can be distinguished:

- plane stress

  The geometry of the body is that of a plate, i.e., one dimension is much smaller than the other two and the applied load is distributed uniformly over the thickness and act in that plane. The elastic constitutive equation is

$$\sigma_{ij} = \left(C_{ijkl} - \frac{C_{ij33}}{C_{3333}} C_{kl33} \right) \varepsilon_{kl} = Q_{ijkl}\, \varepsilon_{kl} \quad ; \quad i,j,k,l = 1,2 \tag{2.40}$$

  or, written in matrix form

$$\begin{bmatrix} \sigma_{11} \\ \sigma_{22} \\ \sigma_{12} \end{bmatrix} = \begin{bmatrix} Q_{1111} & Q_{1122} & Q_{1112} \\ Q_{2211} & Q_{2222} & Q_{2212} \\ Q_{1211} & Q_{1222} & Q_{1212} \end{bmatrix} \begin{bmatrix} \varepsilon_{11} \\ \varepsilon_{22} \\ \varepsilon_{12} \end{bmatrix} \quad . \tag{2.41}$$

  The Q_{ijkl} are called reduced stiffness factors [1]. Derivations are not given here, the reader is referred to well-known textbooks, e.g. [19], [11].

- plane strain

  The geometry of the body is essentially that of a prismatic cylinder with one dimension much larger than the others. The loads are uniformly distributed with respect to the large dimension and act perpendicular to it. The corresponding equations and derivations can be found in literature.

2.3.2 Linear viscoelasticity

The linear elastic constitutive equation has been elaborated in the previous chapter. This relationship between stress and strain is time-independent, in other words if an elastic material is subjected to a suddenly applied loading state held constant thereafter, it responds instantaneously with a state of deformation which remains constant [11, 17]. The linear viscoelastic constitutive equation, in contrast, exhibits a time-dependent reaction on an applied load state. The phenomena occurring in the reaction of a viscoelastic material are called *creep* and *relaxation*. They can be demonstrated by the so-called standard test for viscoelastic solids: A Heaviside stress $\sigma(t) = \sigma_0 H(t)$ is applied to a material (see Appendix A.2 for the definition of the Heaviside function). The response consists of an instant reaction ε_0 and a creep phase during which the strain continuously increases over the time (see Figure 2.3). At the exact time when the stress load is released, the strain ε is held constant. The stress slowly decreases during the so-called relaxation phase. Consequently, the current stress state is not only determined by the current strain state but also by the history of strain. The same applies to the current strain, which does not only depend on the current stress state but also on the stress history. While the theory of elasticity accounts for materials which have the capacity to store energy and completely release it, the theory of viscoelasticity describes materials in which energy is only stored partially. A certain amount of energy is dissipated during the creep and relaxation phase, i.e., *damping* occurs. Physically, the damping of a material is caused by molecular phenomena, e.g., inner friction.

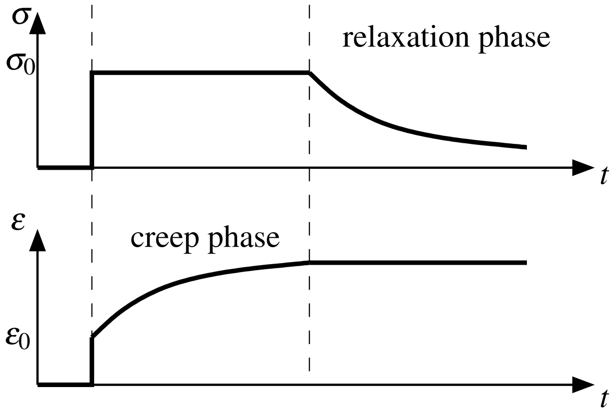

Figure 2.3: Creep and relaxation

Integral formulation

As has been mentioned above, the stress strain relation of a viscoelastic material requires the complete stress-strain history. This memory function of a material can mathematically be described by an hereditary integral. In the one-dimensional case, the viscoelastic constitutive equation reads

$$\varepsilon(t) = \int_0^t J(t-\bar{t})\frac{\mathrm{d}\sigma(\bar{t})}{\mathrm{d}\bar{t}}\mathrm{d}\bar{t} \quad . \tag{2.42}$$

The function $J(t)$ is the so-called creep function. It describes the strain of a of a body which is loaded with a Heaviside stress function as given in Figure 2.4.

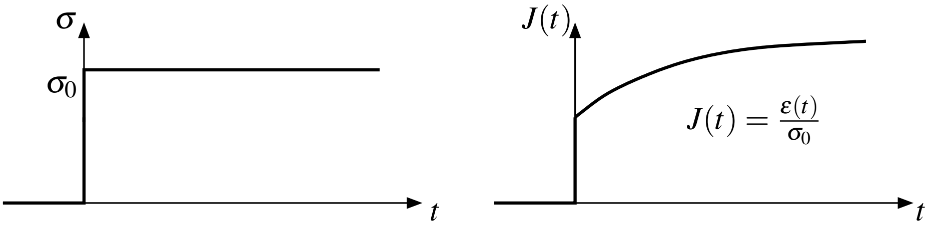

Figure 2.4: Creep function

The hereditary integral in equation (2.42) can be derived by approximating a non-constant stress function $\sigma(t)$ with a sequence of infinitesimal step functions (see Figure 2.5). The approximated stress is

$$\sigma(t) \approx \sum_j \Delta\sigma_j H(t-\bar{t}) \quad . \tag{2.43}$$

Using the rule of linear superposition, the strain yields

$$\varepsilon(t) \approx \sum_j \Delta\sigma_j J(t-\bar{t}) \quad , \tag{2.44}$$

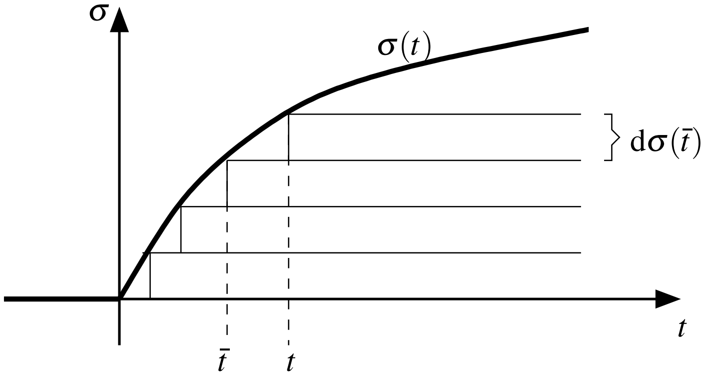

Figure 2.5: Derivation of the hereditary integral

where all stress steps, starting at $t = 0$, are taken into account. Considering infinitesimal small stress steps,

$$\varepsilon(t) = \int_0^t J(t-\bar{t})\mathrm{d}\sigma \quad , \tag{2.45}$$

is obtained, which can be written as ($\mathrm{d}\sigma(\bar{t}) = \frac{\mathrm{d}\sigma(\bar{t})}{\mathrm{d}\bar{t}}\mathrm{d}\bar{t}$)

$$\varepsilon(t) = \int_0^t J(t-\bar{t})\frac{\mathrm{d}\sigma(\bar{t})}{\mathrm{d}\bar{t}}\mathrm{d}\bar{t} \quad . \tag{2.46}$$

In the three-dimensional case, J is, analogously to the theory of elasticity, replaced by a fourth-oder tensor J_{ijkl}. The viscoelastic constitutive equation is then

$$\varepsilon_{ij}(t) = \int_0^t J_{ijkl}(t-\bar{t})\frac{\mathrm{d}\sigma_{kl}(\bar{t})}{\mathrm{d}\bar{t}}\mathrm{d}\bar{t} \quad . \tag{2.47}$$

Rheological models

Another, very descriptive derivation for the theory of viscoelasticity is the usage of rheological models. These models consist of the simple elements spring and dash-pot.

The spring is the representation of Hooke's law in the one-dimensional case, stating that the stress is proportional to the strain, i.e.,

$$\sigma = E\varepsilon \quad . \tag{2.48}$$

The dash-pot is the representation of the viscous material behavior which states that the stress is not proportional to the strain ε, but to the time rate of change $\dot{\varepsilon}$

$$\sigma = \eta\frac{\mathrm{d}\varepsilon}{\mathrm{d}t} = \eta\dot{\varepsilon} \quad . \tag{2.49}$$

Viscous behavior is often found in liquids, therefore, translating equation (2.49) into shear stress and shear strain,

$$\tau = \mu \dot{\gamma} \tag{2.50}$$

describes the constitutive equation of a viscous fluid with the viscosity coefficient μ.

Linear viscoelastic material behavior is a combination of the two simple cases. Springs and dash-pots can be combined in a parallel manner, which results in a KELVIN-VOIGT model (see Figure 2.6). The corresponding differential equation can be derived by considering the equilibrium of forces

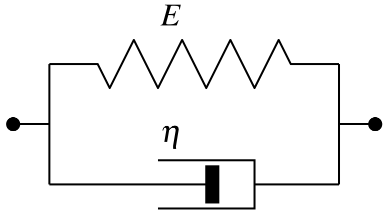

Figure 2.6: KELVIN-VOIGT model

$$\frac{1}{\eta}\sigma + \frac{1}{E}\frac{\mathrm{d}}{\mathrm{d}t}\sigma = \frac{\mathrm{d}}{\mathrm{d}t}\varepsilon \quad . \tag{2.51}$$

If springs and dash-pots are arranged sequentially, the MAXWELL model is obtained (see Figure 2.7). The corresponding differential equation can be derived by considering the compatibility of deformation

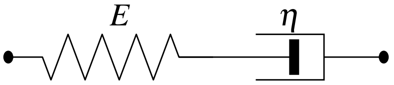

Figure 2.7: MAXWELL model

$$\sigma = E\,\varepsilon + \eta\frac{\mathrm{d}}{\mathrm{d}t}\varepsilon \quad . \tag{2.52}$$

Both models exhibit weaknesses: A stepwise change of strain results in an infinite stress in the KELVIN-VOIGT model and in the MAXWELL MODEL, the stress always relaxes to a value of 0. The most simple model without these deficiencies is the so-called Three-Parameter-Model. It consists of two springs and one dash-pot, see Figure 2.8. The constitutive equation for this model is

$$p\frac{\mathrm{d}}{\mathrm{d}t}\sigma = E\left(\varepsilon + q\frac{\mathrm{d}}{\mathrm{d}t}\varepsilon\right) \quad , \tag{2.53}$$

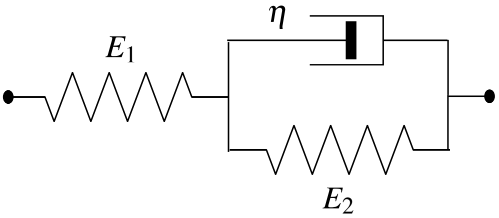

Figure 2.8: Three-Parameter-Model for a solid

with

$$p = \frac{\eta}{E_1 + E_2} \qquad E = \frac{E_1 E_2}{E_1 + E_2} \qquad q = \frac{\eta}{E_2} \quad . \tag{2.54}$$

In general, a further combination of KELVIN-VOIGT and MAXWELL models is possible. An arbitrary number of elements can be chosen. The differential equation of such a model has the form

$$\sum_{k=0}^{N} p_k \frac{\mathrm{d}^k}{\mathrm{d}t^k} \sigma = \sum_{k=0}^{M} q_k \frac{\mathrm{d}^k}{\mathrm{d}t^k} \varepsilon \quad . \tag{2.55}$$

The parameters p_k and q_k can be expressed in terms of spring and dash-pot coefficients, however, the expressions become very complicated if many parameters are involved. A transformation of equation (2.55) into an integral form like equation (2.42) is possible.

Frequency domain formulation

If mechanical systems are loaded harmonically with respect to time, their behavior can be analyzed in frequency domain. The viscoelastic constitutive equation (2.55) then reads

$$\mathcal{F}\{\sigma\} \sum_{k=0}^{N} p_k (i\omega)^k = \mathcal{F}\{\varepsilon\} \sum_{k=0}^{N} q_k (i\omega)^k \quad , \tag{2.56}$$

where $\mathcal{F}$ denotes the Fourier-transformation and ω is the excitation frequency. Thus, the differential equation is replaced by two polynomials and the time-dependence of equation (2.55) is replaced by a frequency-dependence. Equation (2.56) can be solved for $\sigma(\omega)$

$$\sigma(\omega) = \frac{\sum\limits_{k=0}^{N} p_k (i\omega)^k}{\sum\limits_{k=0}^{N} q_k (i\omega)^k} \varepsilon(\omega) = G(i\omega)\, \varepsilon(\omega) = \left[G^{storage}(\omega) + i G^{loss}(\omega) \right] \varepsilon(\omega) \quad , \tag{2.57}$$

where $G(i\omega)$ is the complex modulus which can be split up into a real and imaginary part. The real part $G^{storage}$ is called storage modulus because it accounts for the amount of energy that is stored while the imaginary part G^{loss} is called loss modulus since it accounts for the amount of energy that is lost due to energy dissipation.

Fractional derivatives

In order to adjust the parameters of the proposed viscoelastic constitutive equation to measured data, it can be useful to introduce fractional derivatives [38]. The physical meaning of fractional derivatives within the framework of rheological models can be explained by considering the equation for the spring and the dash-pot. The spring equation

$$\sigma = E\varepsilon = E\frac{\mathrm{d}^{(0)}}{\mathrm{d}t^{(0)}}\varepsilon \tag{2.58}$$

can be interpreted as having a '0-th derivative' of the strain, while the dash-pot equation

$$\sigma = F\dot{\varepsilon} = \eta\frac{\mathrm{d}^{(1)}}{\mathrm{d}t^{(1)}}\varepsilon \quad . \tag{2.59}$$

has the first derivative of ε with respect to time. A more general element can be defined with

$$\sigma = \tilde{\eta}\frac{\mathrm{d}^{\alpha}}{\mathrm{d}t^{\alpha}}\varepsilon \qquad , \quad \alpha \in \mathbb{R}^{+} \tag{2.60}$$

which introduces the order of derivative as an additional parameter. Such an element is also called 'spring-pot' [31]. This model is only suitable to give an idea of the fractional derivative parameter and in a strict sense, one can not speak of a rheological model any more because the involved parameters can not be attributed to springs or dash-pots. Despite this fact, a viscoelastic constitutive equation with fractional derivatives has the advantage that it can adapt a measured material behavior more easily [46].

The generalized viscoelastic constitutive equation is then

$$\sum_{k=0}^{N} p_k \frac{\mathrm{d}^{\alpha_k}}{\mathrm{d}t^{\alpha_k}}\sigma = \sum_{k=0}^{M} q_k \frac{\mathrm{d}^{\beta_k}}{\mathrm{d}t^{\beta_k}}\varepsilon \quad . \tag{2.61}$$

2.4 Auxetic Materials

2.4.1 The term auxetic

The linear elastic constitutive equation of materials was discussed in chapter 2.3.1. In the isotropic case, the behavior of a material can be characterized via two independent parameters, e.g., Young's modulus E and Poisson's ratio ν. From a continuum mechanics point of view, there is no restriction for Poisson's ratio to be positive, see equation (2.39).

The physical meaning of a negative Poisson's ratio is shown in Figure 2.9, where a tensile load is applied to an initially undeformed material (dashed line). If the Poisson's ratio is positive, it exhibits a lateral contraction (see Figure 2.9 a)) while a material with a negative Poisson's ratio expands in lateral direction (see Figure 2.9 b)). Materials with such a counterintuitive behavior are referred to as auxetic materials. The term auxetic

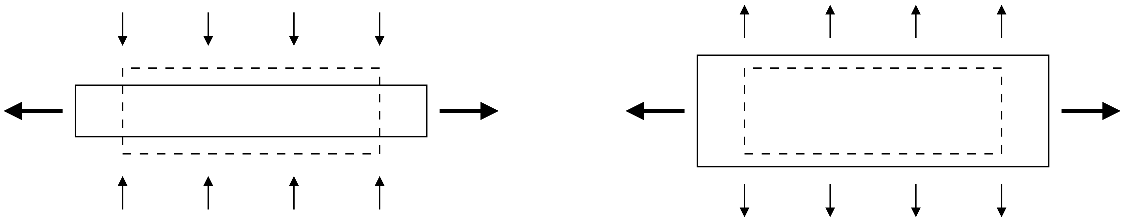

a) Non-auxetic b) Auxetic

Figure 2.9: Schematic deformation of a material

comes from the greek word ’αυχετος’ meaning ’that which may be increased in size’. There are other terms, for example *dilational* which actually means widening. In this context, the term arise because solids with a negative Poisson’s ratio easily undergo volume changes. Another term is *anti-rubber* which is very descriptive because most rubbers have a Poisson’s ratio close to the isotropic upper limit of 0.5. Thus, auxetic materials represent the exact opposite of rubbery materials. An overview of auxetic materials is given in [14, 15]

2.4.2 Origin of auxetic behavior

From a literature review, it can be stated that the auxetic effect is attributed to a nonstandard microstructure [34, 39]. Mostly, simplified models of beam-type microstructures are used. Several models have been discussed for the explanation of the auxetic effect. The most plausible microstructure which allows for the explanation of the auxetic behavior is a non-convex microstructure. Non-convex, in this context, means that the microstructure features re-entrant corners, see Figure 2.10. If a material is composed of these star-shaped cells and pulled in longitudinal direction, the kinematic mechanism causes it to expand laterally. Many other types of microstructures have been proposed (see Figure 2.11). The reader is referred to the publications [14, 47, 51] where a variety of these mechanisms are presented. However, all of them have some kind of re-entrant corners and the causing mechanism is always similar.

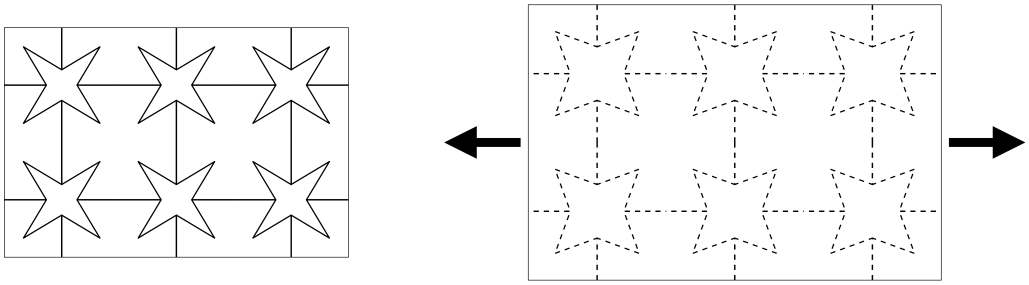

Figure 2.10: Causing mechanism of auxetic material

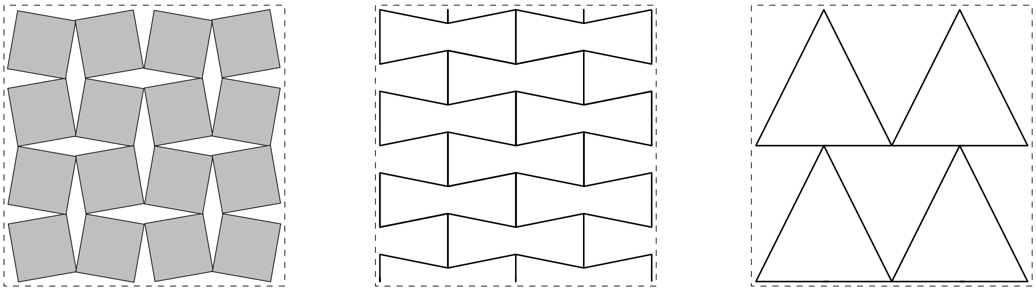

Figure 2.11: Auxetic microstructures

2.4.3 Naturally occurring materials

Our everyday experience tells us that when a material is stretched, it will become thinner in cross-section. Nobody expects a material to increase in cross-section which is not surprising because there are no known examples for natural materials that behave auxetically on the macroscale. On the molecular scale, however, a number of examples exist. The α-cristobalite polymorph of crystalline silica for example is auxetic. A description, including the deformation mechanism is given in [14]. Other examples for Auxetics on the molecular scale exist, for example the single-crystal materials arsenic and cadmium [14]. Until now, however, it was not yet possible to create a material consisting only of auxetic molecules and thus exposing auxetic behavior on the macroscale. Another group of natural auxetic material are biomaterials, although it is difficult to determine exact properties of them in the natural state. Skin, for example, is said to be auxetic [35, 55], as well as cancerous bone with a cellular microstructure [57]. There might be other examples, however, since it is not possible to perform measurements of material constants, auxetic biomaterials remain a rather speculative phenomenon. Moreover, other effects might influence the behavior of these 'materials', such as muscle contraction or chemical reactions.

2.4.4 Man-made auxetic materials and structures

A variety of man-made auxetic materials have been developed and fabricated in recent years. One can distinguish between honeycomb-like structures, open-cell foams and polymeric materials.

Honeycomb-like structures

A representative example for a honeycomb-like structure is the re-entrant honeycomb membrane fabricated by K. EVANS from the University of Exeter. Figure 2.12 shows the material and a schematic model. The polymeric material with cell dimensions of $\approx$ 1mm was fabricated by laser ablation. Similar microstructures could be produced without great

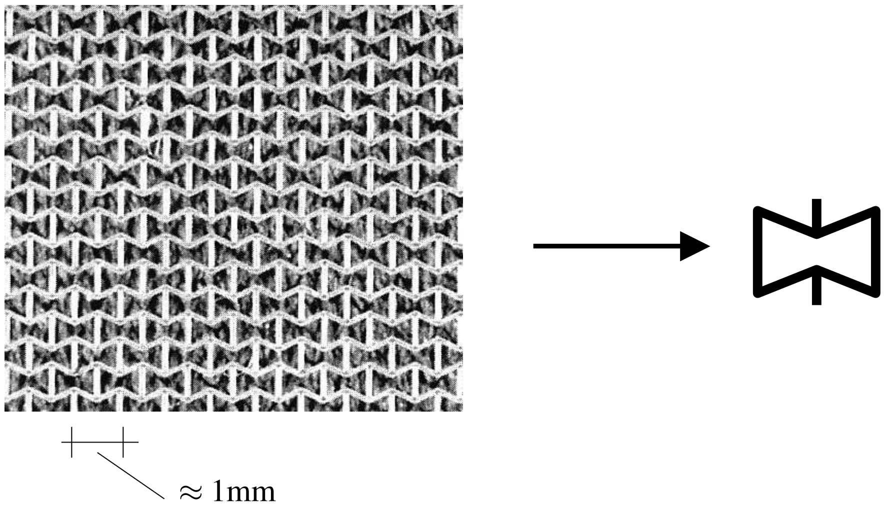

Figure 2.12: Cellular auxetic material

effort, which leads to the possibility of 'tailoring' a material, i.e., producing a microstructure which has specific characteristics, for example a given Poisson's ratio.

Foams

The pioneering work in the field of auxetic foams was done by RODERIC LAKES from the University of Wisconsin, he was the first to introduce a negative Poisson's ratio foam material [34]. The foam was produced from a conventional low density open-cell polymer foam by causing the ribs of each cell to permanently protrude inward, resulting in a reentrant structure. Both conventional and auxetic foams are shown in Figure 2.13.

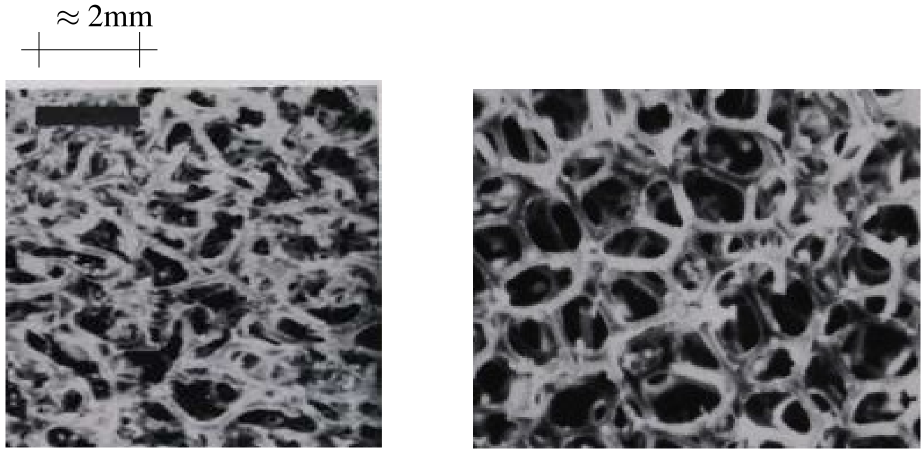

a)

auxetic foam b) non-auxetic foam

Figure 2.13: Auxetic and non-auxetic foam

An analysis of this polymeric cellular material was then given in [7], where the behaviour under torsional vibration was analyzed and compared to a conventional material. Dispersion of standing waves and cut-off frequencies were observed. Furthermore, this wave dispersion was studied in a more detailed paper [8], including a numerical investigation of the material. An industrial application is given in [36]. The auxetic foam was used as a seat cushion material. By investigating the pressure distributions on a seated subject, it was found that the auxetic material exerts a reduced peak pressure.

Polymers

A further group of auxetic materials are liquid crystal polymers (LCPs). Each LCP chain consists of a series of rods interconnected terminally or laterally by flexible spacers, as shown in Figure 2.14. Then, as the structure is stretched, the rods attached laterally rotate perpendicular to the main chain, pushing neighbouring chains apart. This increases the inter-chain distance and may give rise to the auxetic effect.

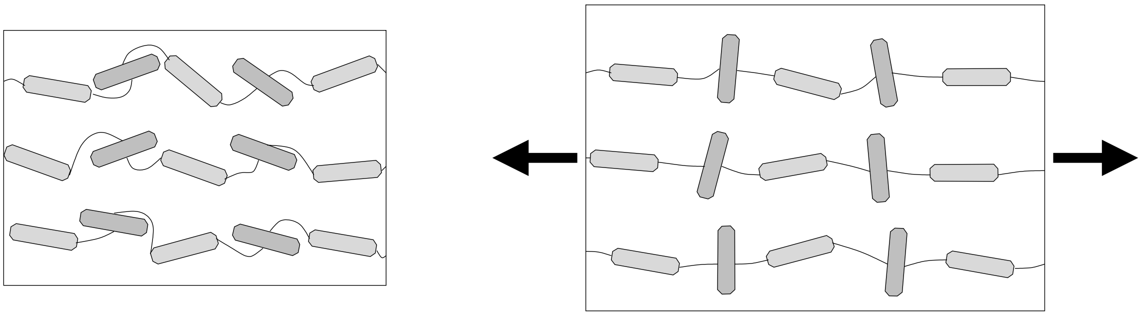

Figure 2.14: Polymeric auxetic material (schematic)

2.4.5 Industrial applications

Potential applications for auxetic materials have been shown in many publications. Since they are suspected to have good damping characteristics, they could be used as structural parts for noise insulation[43, 44, 44]. Another direct application is in seals and gaskets. A conventional gasket tends to be squeezed out between, for example, the flages of a pipe. If the gasket could be made to be auxetic, however, it would contract in on itself, producing a tighter seal. Auxetic materials could also be used in applications where shock absorption is of importance. It is suspected that a variety of auxetic materials have better indentation resistance than their conventional counterparts. The reason is that if an object impacts an auxetic material, material flows into the vicinity of the impact as a result of lateral contraction accompanying the longitudinal compression due to the impacting object. Hence the material densifies under the impact on both the longitudinal and transverse directions, leading to increased indentation resistance. For non-auxetic materials, on the other hand, material ’flows’ away in the lateral direction, leading to a reduction in density and, therefore, a reduction in the indentation resistance.

In [22] for example, a study of the implications of using auxetic materials in the design of smart structures is presented. By using auxetic materials as core and piezoelectric actuators as face layers, the shape control of a sandwich beam is investigated. In [10], a fastener based on negative Poisson’s ratio foam is designed. The insertion of the fastener is facilitated by the lateral contraction which the material exhibits under compression. The removal is then blocked by the elastic expansion under tension.

Auxetic materials research is still at a stage where no specific materials or applications have reached series-production readiness. However, there are many possible applications which show that there might be a great potential in such materials.

3 CALCULATION OF TRUSS STRUCTURES

In the previous chapter, different microstructures were presented which cause materials to have a negative Poisson's ratio. Mostly, beam-type models were used because they provide a very descriptive explanation of the auxetic effect. The beam is one of the most important constructional element in structural mechanics. A constructional element is called beam if one physical dimension is considerably larger than the other two. A beam carries lateral load by bending, if the load is parallel to the axis, one speaks of a bar rather than a beam.

A structure consisting of straight beams connected at joints is called truss. Several studies are known for the calculation of trusses. Since in structural mechanics, the Finite Element Method (FEM) is mostly applied in practice, many publications exist with different element types and formulations for truss structures [4, 58]. As an alternative to the FEM, the Boundary Element Method (BEM) has been developed in recent years for the numerical solution of various engineering mechanic problems. In this chapter, a Boundary Element formulation is presented which provides an exact solution for the calculation of plane truss structures in statics and in frequency domain.

3.1 Basic Equations and Fundamental Solutions

3.1.1 Beam

The most common theory to describe the behavior of a beam is Euler-Bernoulli's theory of bending. Assuming that Young's modulus E and the moment of inertia I are constant over the beam length, it can be written via the well-known fourth order partial differential equation

$$EI\frac{\partial^4}{\partial x^4}w+\rho A\frac{\partial^2 w}{\partial t^2}=q \quad , \tag{3.1}$$

where ρ is the density of the beam material and A is the area of cross-section. The time- and space-dependency of the deflection $w=w(x,t)$ and the vertical load $q=q(x,t)$ was skipped for the sake of brevity in equation (3.1). In static calculations, Euler-Bernoulli's theory of bending is sufficiently accurate, especially for slender beams with a large length/width ratio [3]. However, in the description of beams with a relatively small length/width ratio and in dynamic calculations, the shear deformation and rotatory inertia of a beam requires a more precise theory. Therefore, TIMOSHENKO [52] developed a refined theory of bending in which the deflection w does not only depend on the rotation φ but also on the angle of

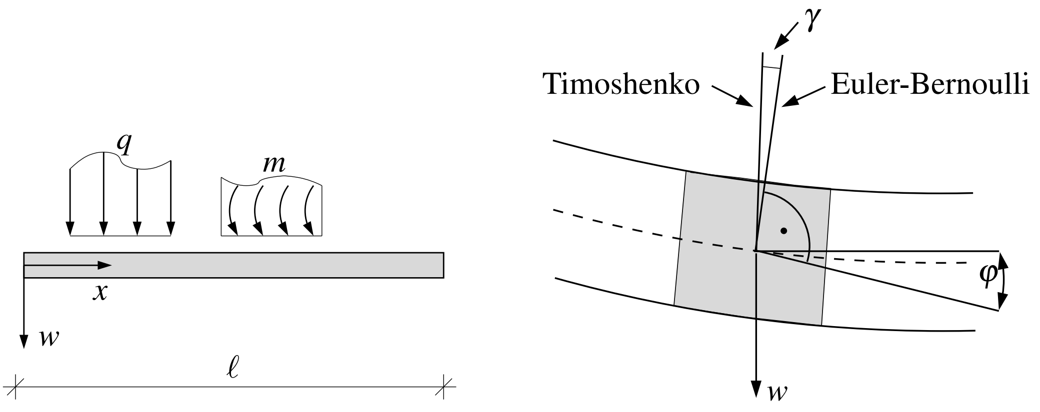

Figure 3.1: Simple beam, shear angle

shear γ at the neutral axis (see Figure 3.1). Thus, the first derivative of the deflection is

$$\frac{\partial}{\partial x} w(x,t) = -\varphi(x,t) + \gamma(x,t) \quad . \tag{3.2}$$

The theory can be written in the following coupled system of differential equations

$$\underbrace{\begin{bmatrix} \kappa GA \frac{\partial^2}{\partial x^2} - \rho A \frac{\partial^2}{\partial t^2} & \kappa GA \frac{\partial}{\partial x} \\ -\kappa GA \frac{\partial}{\partial x} & EI \frac{\partial^2}{\partial x^2} - \kappa GA - \rho I \frac{\partial^2}{\partial t^2} \end{bmatrix}}_{\mathbf{B}_t} \begin{bmatrix} w \\ \varphi \end{bmatrix} = - \begin{bmatrix} q \\ m \end{bmatrix} \quad . \tag{3.3}$$

In equation (3.3), G is the shear modulus and m is a momentum load on the beam (see Figure 3.1). The so-called shear coefficient κ gives the ratio of the average shear strain on a section to the shear strain at the centroid (for details, see, e.g., [53]). Its value is dependent on the shape of cross-section, but also, as pointed out by Cowper [12], on the material's Poisson ratio and, moreover, for dynamic problems on the considered frequency range. Different approximations exist, e.g., that of ROARK for only static deflections with $\kappa = 0.9$ for a circular and $\kappa = 5/6$ for rectangular cross sections [42].

The two coupled differential equations of second order (3.3) can as well be written in one fourth order differential equation by eliminating the state φ

$$\begin{aligned} EI \frac{\partial^4 w}{\partial x^4} + \rho A \frac{\partial^2 w}{\partial t^2} - \rho I (1 + \frac{E}{\kappa G}) \frac{\partial^4 w}{\partial t^2 \partial x^2} + \rho A \frac{\rho I}{\kappa GA} \frac{\partial^4 w}{\partial t^4} \\ = q - \frac{I}{\kappa GA} (E \frac{\partial q}{\partial x^2} - \rho \frac{\partial^2 q}{\partial^2 t}) \quad . \end{aligned} \tag{3.4}$$

Neglecting the shear deformation and rotatory inertia (i.e., $G \to \infty$ and $\rho I \to 0$) in equations (3.3) or (3.4), the Euler-Bernoulli beam equation (3.1) is obtained. Here, however, equation (3.3) is used because this form is more suitable for the following considerations.

For harmonic loadings $q = \hat{q}(x,t)e^{i\omega t}$ and $m = \hat{m}(x,t)e^{i\omega t}$ with the same excitation frequency ω or only one type of excitation, both responses can also assumed to be harmonic with this frequency and their amplitudes $\hat{w}$ and $\hat{\varphi}$ are described by

$$\underbrace{\begin{bmatrix} \kappa GA\frac{\partial^2}{\partial x^2} - \rho A\omega^2 & \kappa GA\frac{\partial}{\partial x} \\ -\kappa GA\frac{\partial}{\partial x} & EI\frac{\partial^2}{\partial x^2} - \kappa GA - \rho I\omega^2 \end{bmatrix}}_{\mathbf{B}_\omega} \begin{bmatrix} \hat{w} \\ \hat{\varphi} \end{bmatrix} = -\begin{bmatrix} \hat{q} \\ \hat{m} \end{bmatrix} \quad . \tag{3.5}$$

The fundamental solutions for Timoshenko's beam theory in frequency domain are the responses of an infinite beam to a unit impulsive force $\hat{q}^*(x) = \delta(x-\xi)$ and to a unit impulsive moment $\hat{m}^*(x) = \delta(x-\xi)$, respectively, at the point ξ. With $\delta(x-\xi)$, the Dirac delta distribution is denoted (see Appendix A.2). Using a short operator notation, the fundamental solution matrix $\mathbf{G}$ is defined by

$$\mathbf{B}_\omega\mathbf{G} = -\mathbf{I}\delta(x-\xi), \tag{3.6}$$

or, in detail,

$$\begin{aligned} &\begin{bmatrix} \kappa GA\frac{\partial^2}{\partial x^2} - \rho A\omega^2 & \kappa GA\frac{\partial}{\partial x} \\ -\kappa GA\frac{\partial}{\partial x} & EI\frac{\partial^2}{\partial x^2} - \kappa GA - \rho I\omega^2 \end{bmatrix} \begin{bmatrix} \hat{w}_q^*(x,\xi) & \hat{w}_m^*(x,\xi) \\ \hat{\varphi}_q^*(x,\xi) & \hat{\varphi}_m^*(x,\xi) \end{bmatrix} \\ &\qquad = -\begin{bmatrix} \delta(x-\xi) & 0 \\ 0 & \delta(x-\xi) \end{bmatrix} \quad . \end{aligned} \tag{3.7}$$

Following the ideas of HÖRMANDER [28], the fundamental solutions can be found from a scalar function ψ via the ansatz

$$\underbrace{\begin{bmatrix} \hat{w}_q^*(x,\xi) & \hat{w}_m^*(x,\xi) \\ \hat{\varphi}_q^*(x,\xi) & \hat{\varphi}_m^*(x,\xi) \end{bmatrix}}_{\mathbf{G}} = \underbrace{\begin{bmatrix} EI\frac{\partial^2}{\partial x^2} - \kappa GA - \rho I\omega^2 & -\kappa GA\frac{\partial}{\partial x} \\ \kappa GA\frac{\partial}{\partial x} & \kappa GA\frac{\partial^2}{\partial x^2} - \rho A\omega^2 \end{bmatrix}}_{\mathbf{B}_\omega^{co}} \psi \tag{3.8}$$

with the matrix of cofactors $\mathbf{B}_\omega^{co}$ of the operator matrix $\mathbf{B}_\omega$ (see Appendix A.3 for the definition of the cofactor matrix). With

$$(\mathbf{B}_\omega)^{-1} = \frac{\mathbf{B}_\omega^{co}}{\det(\mathbf{B}_\omega)} \quad , \tag{3.9}$$

the more convenient form

$$\mathbf{B}_\omega\mathbf{G} = \mathbf{B}_\omega\mathbf{B}_\omega^{co}\psi = \det(\mathbf{B}_\omega)\underbrace{\mathbf{B}_\omega(\mathbf{B}_\omega)^{-1}}_{\mathbf{I}}\psi = -\mathbf{I}\delta(x-\xi) \tag{3.10}$$

is achieved. The two roots of $\det(\mathbf{B}_\omega) = 0$ are

$$\lambda_{1,2} = -\frac{\omega^2}{2}\left[\left(\frac{1}{c_\ell^2} + \frac{1}{c_s^2}\right) \pm \frac{1}{c_\ell^2}\sqrt{\left(1 - \frac{c_\ell^2}{c_s^2}\right)^2 + 4\frac{c_\ell^2 A}{\omega^2 I}}\right] \quad , \tag{3.11}$$

with the longitudinal and shear wave speeds

$$c_\ell = \sqrt{\frac{E}{\rho}} \tag{3.12}$$

$$c_s = \sqrt{\frac{\kappa G}{\rho}} \quad . \tag{3.13}$$

Thus, the problem is reduced to find a solution of the iterated Helmholtz operator

$$\left(\frac{\partial^2}{\partial x^2} - \lambda_1\right)\left(\frac{\partial^2}{\partial x^2} - \lambda_2\right)\psi = -\frac{\delta(x-\xi)}{\kappa GA\,EI} \quad . \tag{3.14}$$

From several publications, e.g., from CHENG et al. [9], one knows its solution

$$\psi = \frac{1}{2\kappa GA\,EI(\lambda_1 - \lambda_2)}\left[\frac{e^{-\sqrt{\lambda_1}r}}{\sqrt{\lambda_1}} - \frac{e^{-\sqrt{\lambda_2}r}}{\sqrt{\lambda_2}}\right] \tag{3.15}$$

with

$$r = \mid x - \xi \mid \quad . \tag{3.16}$$

Finally, the operator $\mathbf{B}_\omega$ is applied on the scalar function ψ. The fundamental solutions due to a unit force impulse and a unit moment impulse at $x = \xi$ are then found to be

$$\begin{aligned}
\hat{w}_q^*(x,\xi) &= \frac{1}{2\kappa GA}\frac{1}{\lambda_1 - \lambda_2}\left[\frac{e^{-\sqrt{\lambda_1}r}}{\sqrt{\lambda_1}}\left(\lambda_1 - \frac{\kappa GA - \rho I\omega^2}{EI}\right)\right. \\
&\quad \left. - \frac{e^{-\sqrt{\lambda_2}r}}{\sqrt{\lambda_2}}\left(\lambda_2 - \frac{\kappa GA - \rho I\omega^2}{EI}\right)\right] && (3.17a) \\
\hat{\varphi}_q^*(x,\xi) &= \frac{1}{2EI}\frac{2H(x-\xi) - 1}{\lambda_1 - \lambda_2}\left[-e^{-\sqrt{\lambda_1}r} + e^{-\sqrt{\lambda_2}r}\right] && (3.17b) \\
\hat{w}_m^*(x,\xi) &= -\hat{\varphi}_q^*(x,\xi) && (3.17c) \\
\hat{\varphi}_m^*(x,\xi) &= \frac{1}{2EI}\frac{1}{\lambda_1 - \lambda_2}\left[\frac{e^{-\sqrt{\lambda_1}r}}{\sqrt{\lambda_1}}\left(\lambda_1 - \frac{\rho A\omega^2}{\kappa GA}\right) - \frac{e^{-\sqrt{\lambda_2}r}}{\sqrt{\lambda_2}}\left(\lambda_2 - \frac{\rho A\omega^2}{\kappa GA}\right)\right] \quad . && (3.17d)
\end{aligned}$$

More detailed derivations of the fundamental solutions are given in [21] or [45].

In the static case, i.e., for $\omega \to 0$, the fundamental solutions simplify to:

$$\begin{aligned}
\hat{w}_q^*(x,\xi) &= \frac{1}{12EI}\left[r^3 - 6\frac{EI}{\kappa GA}r\right] && (3.18a) \\
\hat{\varphi}_q^*(x,\xi) &= -\frac{r^2}{4EI}\left[2H(x-\xi) - 1\right] && (3.18b) \\
\hat{w}_m^*(x,\xi) &= \frac{r^2}{4EI}\left[2H(x-\xi) - 1\right] && (3.18c) \\
\hat{\varphi}_m^*(x,\xi) &= -\frac{r}{2EI} \quad , && (3.18d)
\end{aligned}$$

corresponding to the derivation given in [3].

3.1.2 Bar

If only longitudinal loads act on a beam, it is called bar. The governing equation for the longitudinal deformation $u = u(x,t)$ is of second order

$$EA\frac{\partial^2 u}{\partial x^2} - \rho A\frac{\partial^2 u}{\partial t^2} = -n \quad , \tag{3.19}$$

where $n = n(x,t)$ is the distributed load in axial direction. For time-harmonic loads $n = \hat{n}(x,t)e^{i\omega t}$ with the excitation frequency ω, the response can also be assumed to be time-harmonic. This results in the following differential equation

$$\frac{\partial^2 \hat{u}(x)}{\partial x^2} + \left(\frac{\omega}{c_\ell}\right)^2 \hat{u}(x) = -\frac{\hat{n}(x)}{EA} \tag{3.20}$$

with the longitudinal wave speed c_ℓ, see equation (3.12).

The adequate fundamental solution of the bar equation (3.20), i.e., the axial displacement response of an infinite bar to a unit harmonic axial point force $\hat{n}^*(x) = \delta(x-\xi)$ acting at point ξ, is well-known to be [21]

$$\hat{u}^*(x,\xi) = \frac{-1}{2kEA}\sin(kr) \quad , \qquad k = \frac{\omega}{c_\ell} \, . \tag{3.21}$$

Its correctness can easily be demonstrated, since its first and second derivative, respectively, is

$$\frac{\partial \hat{u}^*(x,\xi)}{\partial x} = \frac{-1}{2EA}\cos(kr)\frac{\partial r}{\partial x} = \frac{-1}{2EA}\cos(kr)[2H(x-\xi)-1] \tag{3.22}$$

$$\frac{\partial^2 \hat{u}^*(x,\xi)}{\partial x^2} = \frac{k}{2EA}\sin(kr) - \frac{\cos(kr)}{EA}\delta(x-\xi) \quad , \tag{3.23}$$

such that

$$\int_0^\ell \left[\frac{\partial^2 \hat{u}^*(x,\xi)}{\partial x^2} + k^2\hat{u}^*(x,\xi)\right] u(x)\mathrm{d}x$$

$$= -\int_0^\ell \frac{\cos(k|x-\xi|)}{EA}\delta(x-\xi)u(x)\mathrm{d}x = \frac{-u(\xi)}{EA} \qquad \text{for } \xi \text{ in } [0,\ell] \, . \tag{3.24}$$

In the static case equation (3.21) simplifies to

$$u^*(x,\xi) = \frac{-r}{2EA} \quad . \tag{3.25}$$

3.2 Integral Equation

The most general methodology to derive from differential equations equivalent integral equations is the method of weighted residuals. The weighted residuum of the beam equation (3.5) is

$$\int_0^{\ell} \left(\mathbf{B}_\omega \begin{bmatrix} \hat{w}(x) \\ \hat{\varphi}(x) \end{bmatrix} + \begin{bmatrix} \hat{q}(x) \\ \hat{m}(x) \end{bmatrix} \right)^T \begin{bmatrix} \hat{w}_q^*(x,\xi) & \hat{w}_m^*(x,\xi) \\ \hat{\varphi}_q^*(x,\xi) & \hat{\varphi}_m^*(x,\xi) \end{bmatrix} \mathrm{d}x = \begin{bmatrix} 0 \\ 0 \end{bmatrix} . \quad (3.26)$$

As weighting function, the matrix of fundamental solutions is chosen. Performing two integrations by part and taking into account the filtering effect of the Dirac distribution, the differential operator $\mathbf{B}_\omega$ is shifted from $\hat{w}(x)$ and $\hat{\varphi}(x)$ on the matrix of fundamental solutions. The following (exact) equation is obtained

$$\begin{aligned} \begin{bmatrix} \hat{w}(\xi) \\ \hat{\varphi}(\xi) \end{bmatrix} &= \int_0^{\ell} \begin{bmatrix} \hat{w}_q^*(x,\xi) & \hat{\varphi}_q^*(x,\xi) \\ \hat{w}_m^*(x,\xi) & \hat{\varphi}_m^*(x,\xi) \end{bmatrix} \begin{bmatrix} \hat{q}(x) \\ \hat{m}(x) \end{bmatrix} \mathrm{d}x \\ &+ \left[\begin{bmatrix} \hat{w}_q^*(x,\xi) & \hat{\varphi}_q^*(x,\xi) \\ \hat{w}_m^*(x,\xi) & \hat{\varphi}_m^*(x,\xi) \end{bmatrix} \begin{bmatrix} \hat{Q}(x) \\ \hat{M}(x) \end{bmatrix} \right. \\ &- \left. \begin{bmatrix} \hat{Q}_q^*(x,\xi) & \hat{M}_q^*(x,\xi) \\ \hat{Q}_m^*(x,\xi) & \hat{M}_m^*(x,\xi) \end{bmatrix} \begin{bmatrix} \hat{w}(x) \\ \hat{\varphi}(x) \end{bmatrix} \right]_{x=0}^{x=\ell} . \quad (3.27) \end{aligned}$$

The corresponding shear force and bending moment terms are given in Appendix B.

The above described transformation of a differential equation into an equivalent integral equation can similarly be applied to the bar equation (3.20). The bar equation, weighted with the fundamental solution (3.21)

$$\int_0^{\ell} \left[\frac{\mathrm{d}^2 \hat{u}(x)}{\mathrm{d}x^2} - h^2 \hat{u}(x) + \frac{\hat{n}(x)}{EA} \right] u^*(x,\xi) \mathrm{d}x = 0 \quad (3.28)$$

is integrated by parts two times over the problem domain, i.e., here, over the bar length ℓ. This gives

$$\begin{aligned} &\left[\hat{u}'(x) u^*(x,\xi) - \hat{u}(x) \frac{\partial u^*(x,\xi)}{\partial x} \right]_0^{\ell} + \int_0^{\ell} \left[\frac{\partial^2 u^*(x,\xi)}{\partial x^2} - h^2 u^*(x,\xi) \right] \hat{u}(x) \mathrm{d}x \\ &= - \int_0^{\ell} \frac{\hat{n}(x)}{EA} u^*(x,\xi) \mathrm{d}x \quad . \quad (3.29) \end{aligned}$$

Taking the filtering effect of the Dirac distribution $\delta(x-\xi)$ into account, the following integral expression for the axial displacement at an arbitrary point $\xi \in [0,\ell]$ is achieved

$$\begin{aligned}\hat{u}(\xi) &= \left[EA\hat{u}'(x)u^*(x,\xi) - \hat{u}(x)EA\frac{\partial u^*(x,\xi)}{\partial x}\right]_{x=0}^{x=\ell} + \int_0^\ell \hat{n}(x)u^*(x,\xi)\mathrm{d}x \\ &= \left[\hat{N}(x)u^*(x,\xi) - \hat{u}(x)\hat{N}^*(x,\xi)\right]_{x=0}^{x=\ell} + \int_0^\ell \hat{n}(x)u^*(x,\xi)\mathrm{d}x \quad . \end{aligned} \tag{3.30}$$

The second boundary state $\hat{N}^*(x,\xi)$ is given in Appendix B.

3.3 Boundary (Element) Equations by Collocation

In beam problems, always two of the state variables $(\hat{w},\hat{\varphi},\hat{M},\hat{Q})$ at each boundary point, i.e., at $x=0$ and $x=\ell$, are unknown, while in a bar problem only one of the state variables $(\hat{u},\hat{N})$ has to be determined. Hence, plane framework problems are, in general, a combination of both, so that three of the six state variables $(\hat{u},\hat{w},\hat{\varphi},\hat{N},\hat{M},\hat{Q})$ are unknown at each of the two boundary points and, consequently, one needs also three boundary equations at these two boundary points. The simplest way to evaluate the above systems (3.27) and (3.30) at these two points, is to perform point collocation at $\xi=0$ and $\xi=\ell$, resulting in

$$\begin{bmatrix} \mathbf{I}-\mathbf{K}(0,0) & \mathbf{F}(0,0) & \mathbf{K}(\ell,0) & -\mathbf{F}(\ell,0) \\ -\mathbf{K}(0,\ell) & \mathbf{F}(0,\ell) & \mathbf{I}+\mathbf{K}(\ell,\ell) & -\mathbf{F}(\ell,\ell) \end{bmatrix} \begin{bmatrix} \mathbf{u}(0) \\ \mathbf{t}(0) \\ \mathbf{u}(\ell) \\ \mathbf{t}(\ell) \end{bmatrix}$$

$$= \int_0^\ell \begin{bmatrix} \mathbf{F}(x,0) \\ \mathbf{F}(x,\ell) \end{bmatrix} \begin{bmatrix} \hat{n}(x) \\ \hat{q}(x) \\ \hat{m}(x) \end{bmatrix} \mathrm{d}x \tag{3.31}$$

with

$$\mathbf{K}(x,\xi) = \begin{bmatrix} \hat{N}^*(x,\xi) & 0 & 0 \\ 0 & \hat{Q}^*_q(x,\xi) & \hat{M}^*_q(x,\xi) \\ 0 & \hat{Q}^*_m(x,\xi) & \hat{M}^*_m(x,\xi) \end{bmatrix} \tag{3.32}$$

$$\mathbf{F}(x,\xi) = \begin{bmatrix} \hat{u}^*(x,\xi) & 0 & 0 \\ 0 & \hat{w}^*_q(x,\xi) & \hat{\varphi}^*_q(x,\xi) \\ 0 & \hat{w}^*_m(x,\xi) & \hat{\varphi}^*_m(x,\xi) \end{bmatrix} \tag{3.33}$$

$$\mathbf{u}(x) = \begin{bmatrix} \hat{u}(x) \\ \hat{w}(x) \\ \hat{\varphi}(x) \end{bmatrix} \tag{3.34}$$

$$\mathbf{t}(x) = \begin{bmatrix} \hat{N}(x) \\ \hat{Q}(x) \\ \hat{M}(x) \end{bmatrix} . \tag{3.35}$$

System (3.31) has the form

$$[\mathbf{E}]\,[\mathbf{d}] = [\mathbf{r}] \tag{3.36}$$

with the 6×12 matrix **E**, the vector of all 12 boundary values **d** and the load vector **r**. In Appendix B, equation (3.31) is given in detailed form. Matrix **E** can be considered as an "element matrix" analogical to an element matrix used in Finite Element calculations. Contrary to the FEM, **E** is not symmetric and also forces and bending moments appear as degrees of freedom. With equation (3.31), a single beam calculation can easily be performed because 6 of the overall 12 boundary values are given as boundary conditions. Thus, the remaining 6 unknown values can be calculated with the 6 available equations. Values for the state variables of inner points can be calculated using (3.27) and (3.30).

3.4 Assembling of System Matrix

Plane truss structures are composed of multiple beams which are connected among each other. It is straightforward to calculate element equation (3.31) for each single beam and transform it into a global coordinate system. Then, taking into account transition conditions at the coupling points of the beams, a system of linear equations for the truss structure can be assembled. At a first glance, it seems that the calculation is not possible because there are only 6 equations for a total of 12 unknown boundary values per beam. However, taking into account the boundary conditions at the supports and transition conditions at the connection points, 6 equations per beam suffice to calculate a truss structure.

3.4.1 Global Coordinates

As a first step to the assembling of a system matrix, it is meaningful to transform the element equation (3.31) into a global coordinate system. Figure 3.2 shows the local and global systems. The local values for the deformation $u_{loc}^{1,2}$, $w_{loc}^{1,2}$, $\varphi_{loc}^{1,2}$ and the forces and bending moments $M_{loc}^{1,2}$, $Q_{loc}^{1,2}$, $N_{loc}^{1,2}$ are transformed into a global coordinate system. The usual sign convention for local values is found in Figure 3.2: At node 1, forces and deformations point into opposite directions, while at node 2, they have the same direction. In the global coordinate system, both forces and also deformations at node 1 and 2 have the

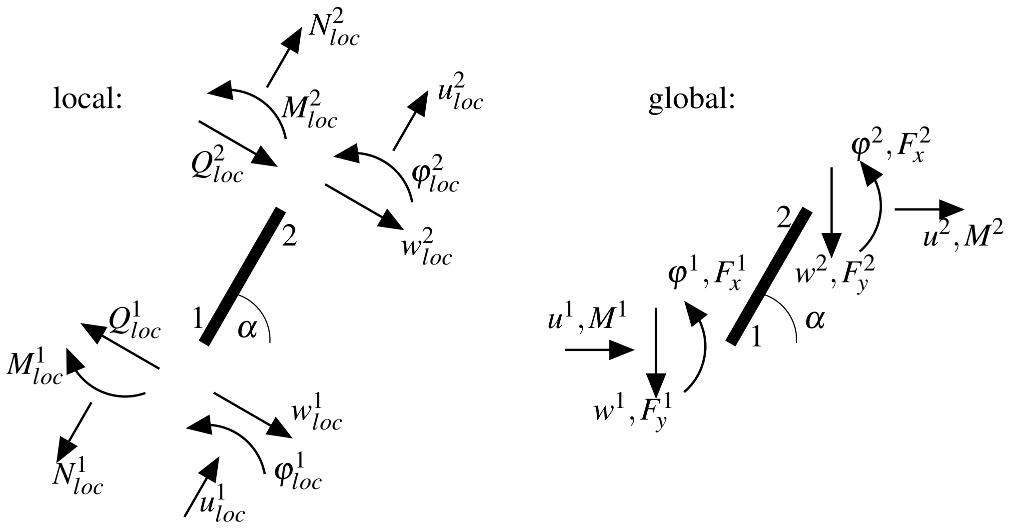

Figure 3.2: Local and global coordinates

same direction. Using the sine and cosine functions, it can be seen that

$$\begin{bmatrix} u^1_{loc} \\ w^1_{loc} \\ \varphi^1_{loc} \\ M^1_{loc} \\ Q^1_{loc} \\ N^1_{loc} \end{bmatrix} = \underbrace{\begin{bmatrix} \cos(\alpha) & -\sin(\alpha) & & & & \\ \sin(\alpha) & \cos(\alpha) & & 0 & & \\ & & 1 & & & \\ & & & -1 & & \\ & 0 & & & -\cos(\alpha) & -\sin(\alpha) \\ & & & & \sin(\alpha) & -\cos(\alpha) \end{bmatrix}}_{\mathbf{T}^1} \begin{bmatrix} u^1 \\ w^1 \\ \varphi^1 \\ M^1 \\ Q^1 \\ N^1 \end{bmatrix} \tag{3.37}$$

and

$$\begin{bmatrix} u^2_{loc} \\ w^2_{loc} \\ \varphi^2_{loc} \\ M^2_{loc} \\ Q^2_{loc} \\ N^2_{loc} \end{bmatrix} = \underbrace{\begin{bmatrix} \cos(\alpha) & -\sin(\alpha) & & & & \\ \sin(\alpha) & \cos(\alpha) & & 0 & & \\ & & 1 & & & \\ & & & -1 & & \\ & 0 & & & \cos(\alpha) & \sin(\alpha) \\ & & & & -\sin(\alpha) & \cos(\alpha) \end{bmatrix}}_{\mathbf{T}^2} \begin{bmatrix} u^2 \\ w^2 \\ \varphi^2 \\ M^2 \\ Q^2 \\ N^2 \end{bmatrix} \quad . \tag{3.38}$$

Incorporating equations (3.37) and (3.38) into (3.36), an element equation in global coordinates is obtained

$$\underbrace{[\mathbf{E}] \begin{bmatrix} \mathbf{T}^1 & \mathbf{0} \\ \mathbf{0} & \mathbf{T}^2 \end{bmatrix}}_{\tilde{\mathbf{E}}} [\tilde{\mathbf{d}}] = [\tilde{\mathbf{r}}] \quad . \tag{3.39}$$

The vector $\tilde{\mathbf{d}}$ contains all 12 boundary values in global coordinates. The load vector $\tilde{\mathbf{r}}$ can be transformed analogically.

3.4.2 Assembling

The assembling of the system matrix is done in the following way:

- rows:
  The element equations of the single beams are arranged row-wise, i.e., the first six rows of the system matrix contain entries of equations for element 1, rows 7 through 12 are occupied by entries of element equation 2 and so on.
- columns:
  The columns of the system matrix represent the unknown boundary values of the beam ends (nodes). It depends on the boundary and transition conditions which unknowns are represented, however, the first columns represent unknowns of node 1, then 2 and so on.

Which unknowns are used in the columns and how exactly they are arranged (*"according to the boundary/transition conditions"*) is demonstrated by the following examples.

3.4.3 Boundary Conditions

As a first example, a single beam problem with rigid supports on both ends is considered, see Figure 3.3. The deformation values are all set to 0, except for the deflection $\bar{w}$ on the right hand side. No further loads act on the system, so the load vector on the right hand side is **0**. Figure 3.4 shows how the boundary conditions are incorporated into the element matrix. On the left hand side, the element matrix $\tilde{\mathbf{E}}$ (see equation (3.39)) is shown with different hatchings for the columns of deformations and forces of nodes 1 and 2. On the right hand side, the Figure shows the system matrix (denoted by **A**) and load vector (denoted by **f**).

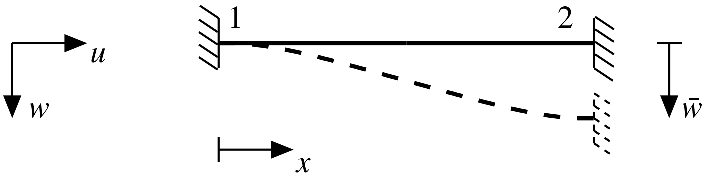

Figure 3.3: Single beam example

The columns of the deformation values of the matrix $\tilde{\mathbf{E}}$ are deleted, except for the column of w_2 which is multiplied with $\bar{w}$ and put into the load vector on the right hand side. The columns for $M_1, Q_1, N_1, M_2, Q_2, N_2$ remain as unknowns in the system matrix **A** which now has 6 rows and 6 columns. The non-symmetric system can be solved with a standard solver for linear equations, e.g. LU-decomposition. With equations (3.27) and (3.30), deformation values at arbitrary points along on the beam can be calculated.

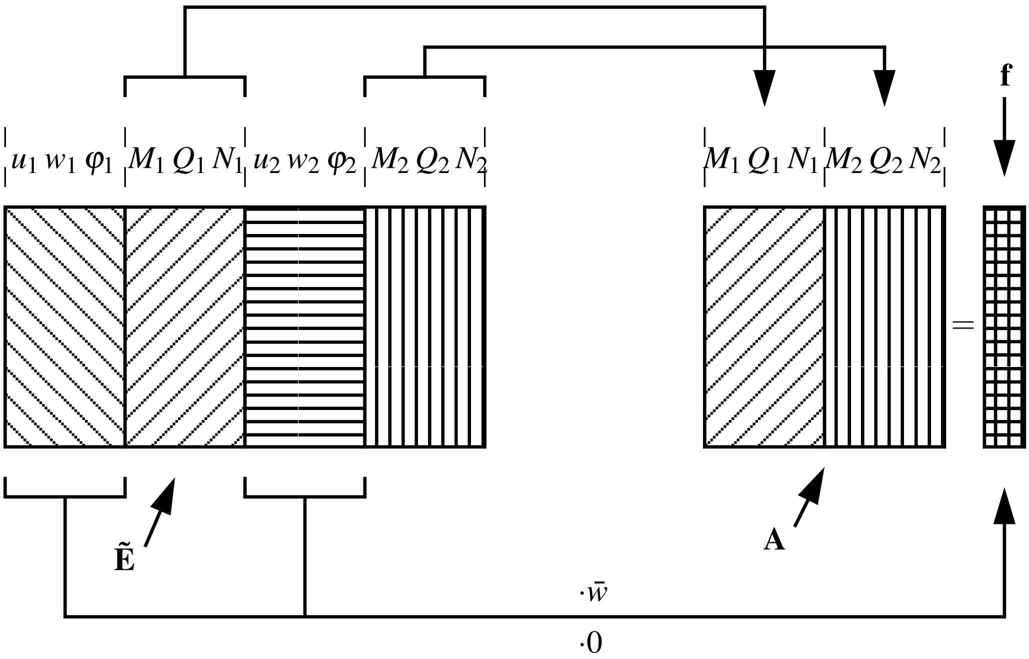

Figure 3.4: Assembling of system matrix

3.4.4 Transition Conditions

The application of transition conditions at the connection points of truss structures is more complicated than in a deformation-based calculation procedure like the FEM. This is due to the fact that in the boundary element equation (3.31), forces and bending moments appear as degrees of freedom. If a rigid connection of n beams is considered (see Figure 3.5), the deformation values of all beam ends must be equal, i.e.,

$$u_1 = u_2 = \cdots = u_n \tag{3.40a}$$

$$w_1 = w_2 = \cdots = w_n \tag{3.40b}$$

$$\varphi_1 = \varphi_2 = \cdots = \varphi_n \quad . \tag{3.40c}$$

The forces and bending moments, however, must satisfy the condition that their sums are 0, so

$$\sum F_x = 0 = F_{x1} + F_{x2} + \ldots F_{xn} \tag{3.41a}$$

$$\sum F_y = 0 = F_{y1} + F_{y2} + \ldots F_{yn} \tag{3.41b}$$

$$\sum M = 0 = M_1 + M_2 + \ldots M_n \quad . \tag{3.41c}$$

The example in Figure 3.6 is considered to demonstrate the assembling. For all three beams, element matrices $\tilde{\mathbf{E}}$ and load vectors $\tilde{\mathbf{r}}$ are set up in a global coordinate system. The six equations of each element are arranged on top of each other in the system matrix. With $\mathbf{u}_n(x)$ and $\mathbf{t}_n(x)$, deformation and force vectors of beam n are denoted, see also equations

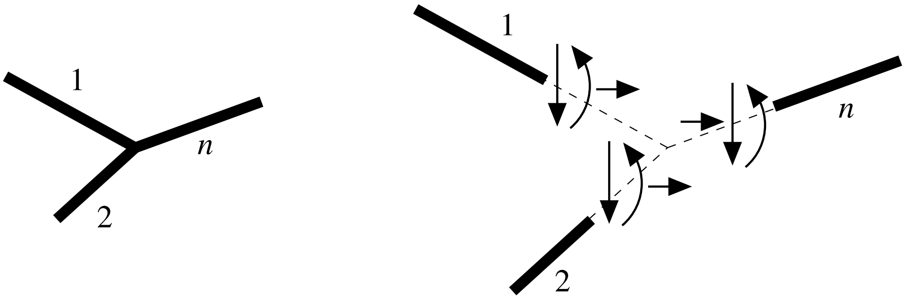

Figure 3.5: Transition conditions of a rigid connection

(3.34) and (3.35). Again, according to the given boundary conditions of the beams, entries of the element matrices are deleted or shifted to the right hand side. In this case, entries $\mathbf{u}_1(0)$, $\mathbf{u}_2(\ell)$ and $\mathbf{t}_3(\ell)$ are deleted, since they are known to be 0. The complementary state variables $\mathbf{t}_1(0)$, $\mathbf{t}_2(\ell)$ and $\mathbf{u}_3(\ell)$ are put into the system matrix. At the connection point, deformation values must be equal, so the entries of $\mathbf{u}_1(\ell)$, $\mathbf{u}_2(0)$ and $\mathbf{u}_3(0)$ are put into the same columns of the system matrix $\mathbf{A}$. In order to satisfy the condition that the sum of forces and bending moments at the connection point must be 0, the following is done: matrix block of $\mathbf{t}_1(\ell)$ is put into the system matrix with a negative sign. Entries of $\mathbf{t}_2(0)$ and $\mathbf{t}_3(0)$ are then written below these two blocks. Thus,

$$-\mathbf{t}_1(\ell) = \mathbf{t}_2(0) + \mathbf{t}_3(0) \tag{3.42}$$

is satisfied. In the system matrix, only $\mathbf{t}_2(0)$ and $\mathbf{t}_3(0)$ appear as degrees of freedom, but $\mathbf{t}_1(\ell)$ can easily be calculated via (3.42). Figure 3.7 shows the prescribed procedure schematically. The resulting system of linear equations is quadratic and thus can be computed with an adequate solver.

3.4.5 Combined Transition/Boundary Conditions

In an arbitrary truss structure, a combination of boundary and transition conditions may occur. Figure 3.8 shows such a case: at the connection point of two beams is a vertical

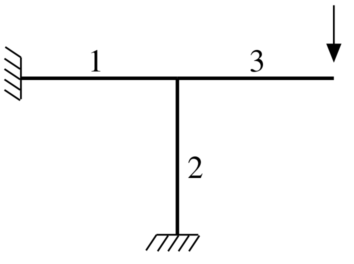

Figure 3.6: Simple truss structure

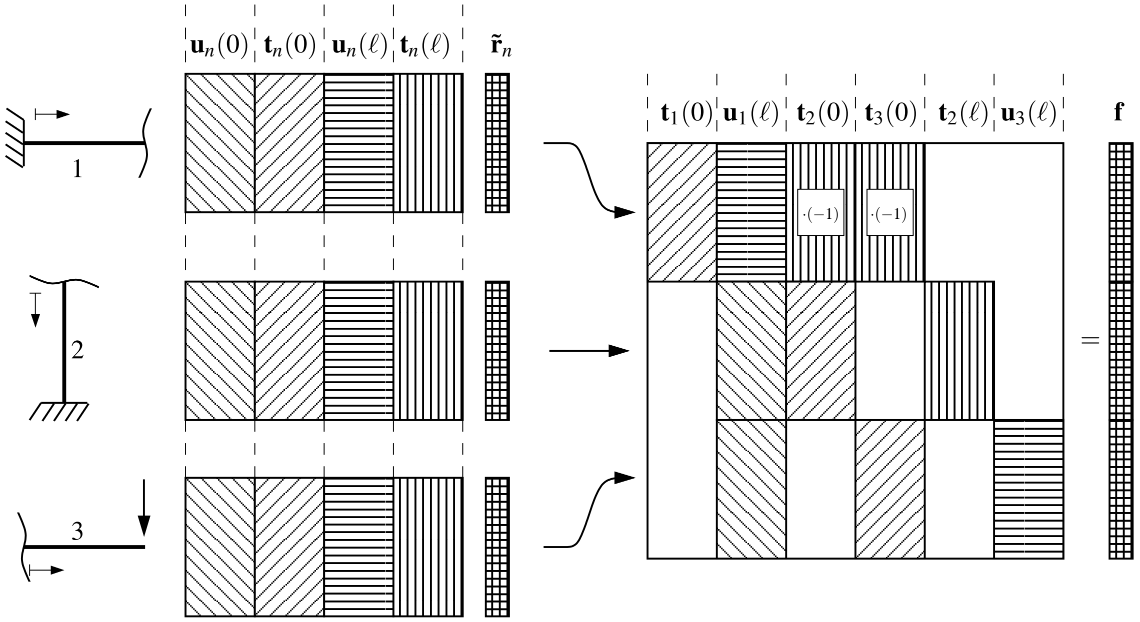

Figure 3.7: Assembling of system matrix

support. Firstly, the two beams are treated as if there was no support, i.e., the matrix

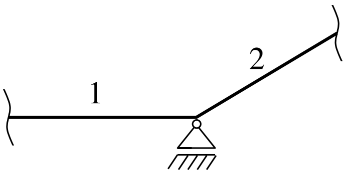

Figure 3.8: Connection point of two beam with a vertical support

entries for the deformation are put in the same columns. Entries for the forces and bending moments are also put in the same columns, entries of beam 1 are multiplied with -1, see Figure 3.9. After this, the support at the connection point is considered. The deflection is set to 0 here, thus, the entries for w can be erased. The blank column is used for the unknown force at the connection point. For this, the following is done: a load of size 1 is put on the right end of the left beam. The resulting load vector is inserted into the free columns of the system matrix. The resulting system can be solved. In principle, the load can as well be put on the left end of the right beam.

3.4.6 Solving the System Matrix

In general, the system matrix is fully populated and not symmetric. It is not possible to generate a symmetric matrix with the prescribed method, however, if the element equa-

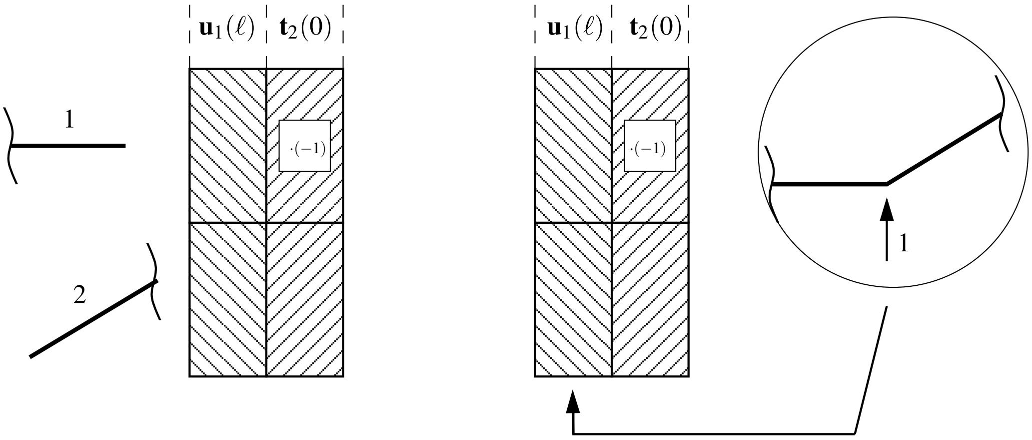

Figure 3.9: Assembling of system matrix

tions (rows in system matrix) and the degrees of freedom (columns in system matrix) are arranged in a specific way, a banded system matrix can be obtained. This is a clear parallel to the Finite Element Method, where one also has local element matrices, which are put into a symmetric, banded system matrix. The example structure shown in Figure 3.10 is used to explain the implication of a ”good” element numbering. The structure consists of

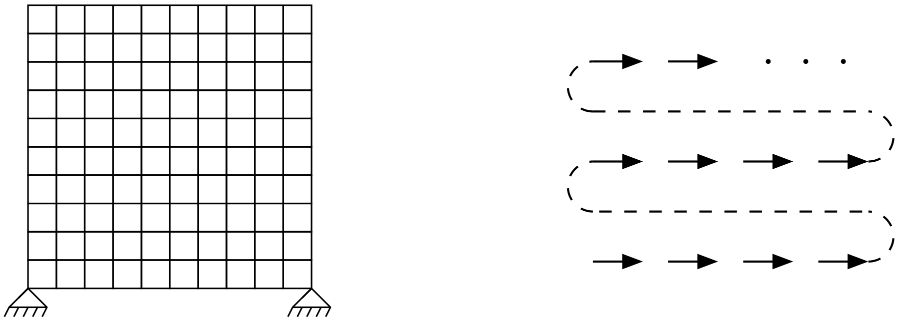
a) example structure b) discretization

Figure 3.10: Example structure and discretization scheme

10×10 square cells with four beams on the edges. The system matrix for the 220 beams and 121 nodes is assembled for two different discretizations. In the first discretization, the numbering of the elements is done randomly and in the second one, node numbers and beam numbers start at the left bottom of the structure, going up line-wise as shown in Figure 3.10. The resulting system matrices are shown in Figure 3.11. If the discretization is done randomly, matrix entries are scattered over the entire matrix. To be precise, there are groups of entries: the six equations of one element (six lines) and degrees of freedom of one node (columns) form one group. The second system matrix exhibits a banded structure. Since the element numbering is done line-wise, there is a band of entries on the diagonal of the matrix. Below the diagonal, there is another band of entries because the element entries of one line of elements are connected with the neighboring lines of elements.

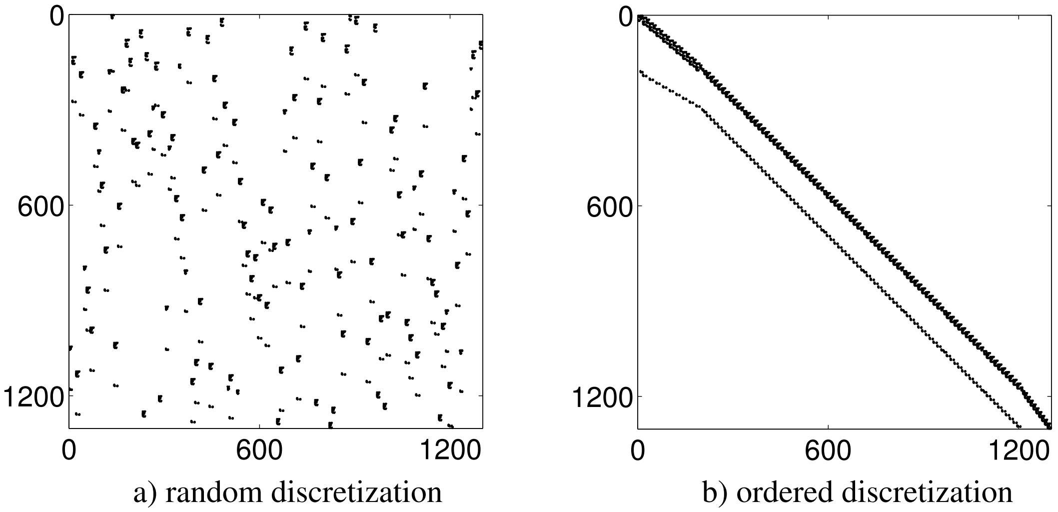

a) random discretization b) ordered discretization

Figure 3.11: Occupancy of system matrix

In this discretization, the bandwidth of the system matrix is determined by the maximum difference of node numbers of a beam element. However, it must be emphasized that this statement can not be generalized like in the FEM.

3.4.7 Example Calculation

The following plane truss structure (see Figure 3.12) is considered which consists of six rigidly connected beams. The beams consist of steel (Young's modulus $E = 2.1 \cdot 10^{11}$ N/m^2, Poisson's ratio $\nu = 0.3$, and material density $\rho = 7850$ kg/m^3) with a rectangular cross section A with $b = h = 0.1$m. The shear coefficient is chosen to be $\kappa = 5/6$. The

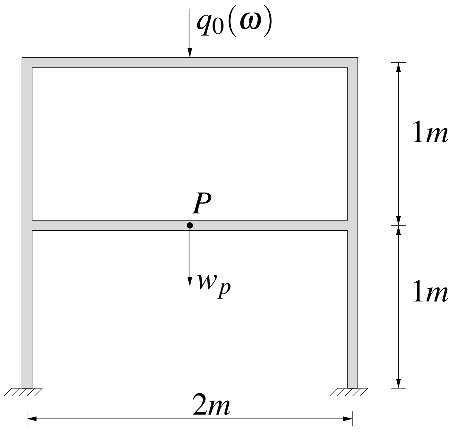

Figure 3.12: Plane frame of six rigidly fixed beams: Geometry, support, and loading

excitation is a frequency-dependent point load of intensity $q_0(\omega) = 1000$ N acting at the centre of the upper beam.

Euler-Bernoulli / Timoshenko

Firstly, a comparison is made between Euler-Bernoulli's theory of bending and Timoshenko's theory of bending. The truss structure is calculated with the prescribed boundary element method for both theories. Euler-Bernoulli results can easily be obtained by setting $\kappa GA \to \infty$. The truss structure is calculated up to a frequency of 900 Hz, increasing the excitation frequency in steps of 10 rad/sec (≈ 1.592 Hz). For comparison, the deflection response w_P at the center point P on the first frame floor is plotted in Figure 3.13 for both theories over the considered frequency range. The static deflection ($\omega \to 0$) is $3.242 \cdot 10^{-6}$m for Euler-Bernoulli's theory and $3.100 \cdot 10^{-6}$m for Timoshenko's theory of bending, which is a difference of less than 5%. Thus, the shear deformation is negligible, which could be expected because the beams have a length/width ratio of of 10 and 20, respectively. This statement about static calculations can be found in many publications, for example [3]: "... the difference of beam reactions determined by Euler-Bernoulli's and by Timoshenko's beam theory depends on the actual geometry, but is in general very small.".

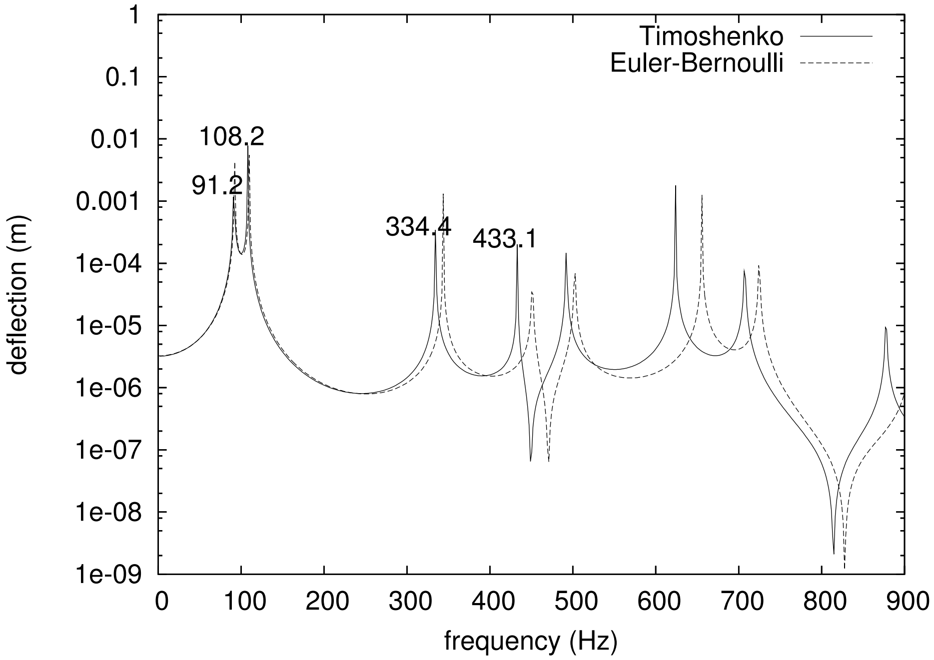

Figure 3.13: Comparison between Euler-Bernoulli and Timoshenko theory

In a frequency range up to 300Hz, there is still no significant difference between both theories. However, in higher frequencies, starting from the third eigenfrequency, a shift of eigenfrequencies can be observed. The shift is small at the third eigenfrequency but increases for the higher frequencies.

BEM / FEM

Since the Finite Element Method is the most established numerical procedure for the calculation of engineering structures, a comparison is made between the prescribed Boundary Element Method and the FEM. Two Finite Element calculations are performed using 32 and 64 Timoshenko beam elements. As stiffness matrix, a cubic Lagrange-element with 4 degrees of freedom (derived from an 8-degrees of freedom element via static condensation) is used (see Appendix C). The mass matrix takes into account the rotatory inertia, a detailed derivation of the element is given in [30]. In longitudinal direction, linear shape functions are used, the resulting element matrix can also be found in [30]. In Figure 3.14, the results of the BEM and FEM calculations are shown. Again, the deflection w_P at the center point P on the first frame floor is plotted versus the excitation frequency. As can be seen, the BEM and FEM results show a good agreement up to a frequency of approximately 250 Hz. With a higher excitation frequency, however, the FEM results become inaccurate. The coarse FEM descretization with 32 elements is less precise than the finer

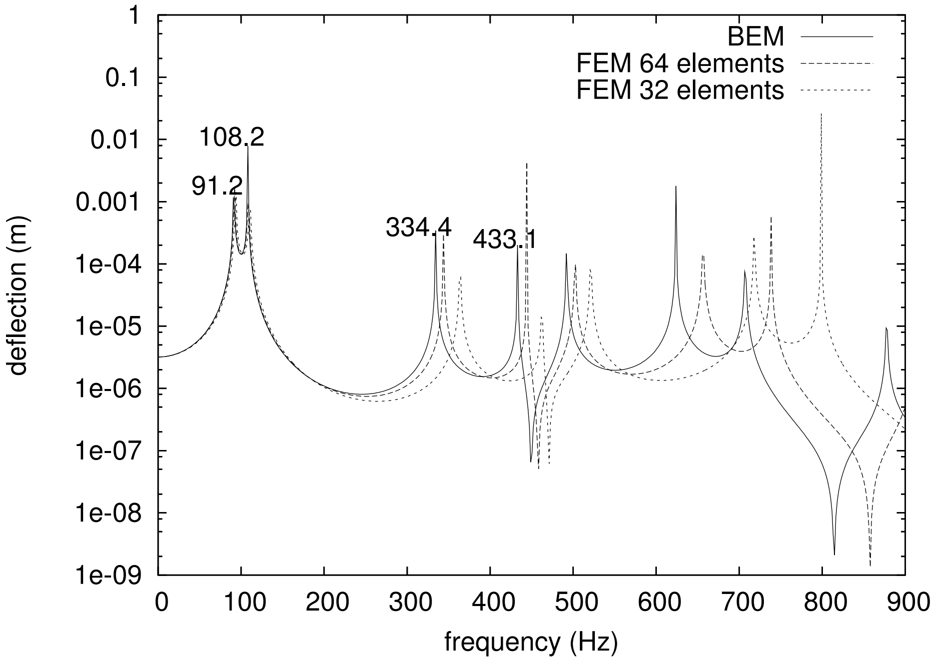

Figure 3.14: Comparison between BEM and FEM

discretization with 64 elements - a typical result of the FEM where the solution usually converges to the exact solution when the mesh is made finer.

More results concerning the comparison between the proposed method and the FEM can be found in [21, 2].

4 MICROMECHANICS AND HOMOGENIZATION

Nearly all materials present a certain heterogeneous microstructure, although they seem to be homogeneous on a macroscopic scale. Heterogeneities such as cracks, cavities, inclusions, laminations, grain boundaries or irregular crystal lattices may occur on a microscopic scale but still the macroscopic behavior can be homogeneous. A good example for such a material is steel, which clearly has a heterogeneous microstructure but exhibits an isotropic behavior on the macroscale. If one were to attempt to perform a direct numerical simulation of such a heterogeneous material, the consideration of all microscale details would require an extremely fine spatial discretization. The resulting system of equations would contain literally billions of numerical unknowns and would be beyond the capacity of computing machines for the foreseeable future. Furthermore, a complete, detailed description of a micro-heterogeneous structure is in many cases not possible or necessary. For these reasons, *homogenization* techniques were developed which aim at predicting the overall, effective behavior of heterogeneous structures. The literature on the homogenization problem is very extensive. A good overview can be found in [37, 60, 20].

4.1 Representative Volume Element

The principle of homogenization can be explained as follows. A body Ω with a characteristic length scale L is considered (see Figure 4.1). The surface of Ω is termed Γ which is subdivided into Γ_t and Γ_u with $\Gamma = \Gamma_u \cup \Gamma_t$. On Γ_u, the displacements are prescribed and on Γ_t, the tractions are prescribed. The body consists of a material with a microstructure which has a characteristic length scale ℓ. Microstructure ingredients such as matrix-inclusions, granular micro-topologies, etc. have the characteristic length scale d (see Figure 4.1).

For the analysis on the macroscopic length scale L, the body Ω is replaced by a similar but quasi-homogeneous body Ω^*. The body Ω^* is bounded by the same external boundaries Γ_t and Γ_u with the same prescribed tractions and displacements but contrary to Ω, it consists of a homogeneous material with yet unknown properties. The aim of the homogenization process is to calculate the properties of Ω^* such that its mechanical behavior is equivalent to that of Ω. Thus, the microstructure is replaced by a homogeneous medium which represents the smeared microstructural behavior.

In order to find properties of the homogeneous material, a specific portion of the microstructure is considered. From this portion, the properties of the corresponding homogeneous material are calculated. Since the homogeneous material must have approximately

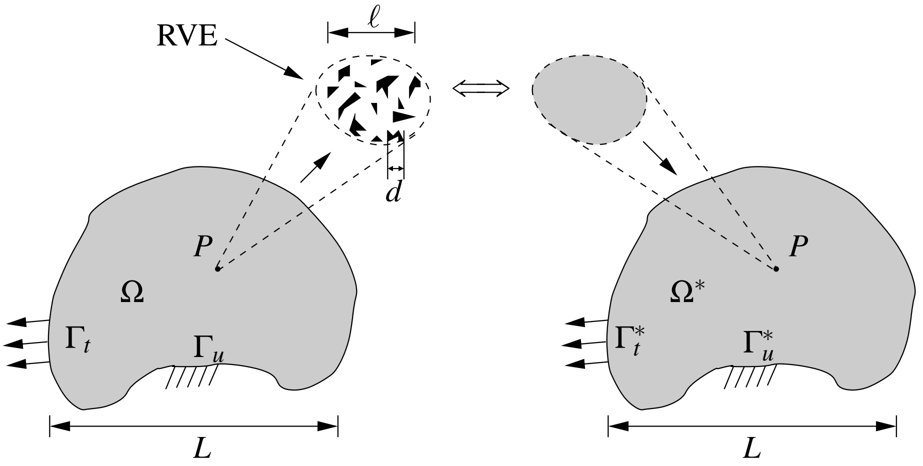

Figure 4.1: Principle of homogenization

the same mechanical properties as the microheterogeneous body Ω, this portion must include all important details of the microstructure. Therefore, it is called *Representative Volume Element* (RVE). For the volume element to be representative, all microstructural details must be included in a statistically correct manner, otherwise the RVE does not reflect the microstructure correctly and the homogeneous properties to be calculated will also not be correct. Thus, the size of the RVE must be large enough to contain all necessary information for the description of the given microstructure so the characteristic length scale d has to be much smaller than ℓ. On the other hand, the size of the RVE can not be too big because it is assumed to be a material point on the macroscopic scale L. Thus, for the choice of an appropriate RVE the condition

$$d \ll \ell \ll L \tag{4.1}$$

must be fulfilled. This condition is termed scale separation. Many authors also speak of a structural hierarchy [32] of materials. The scale difference that is required depends on many factors, so no numerical value can be given.

Besides the scale separation, the condition of macroscopic homogeneity must be fulfilled. This means that the microscopic details must be distributed homogeneously within the body Ω. If this is not the case, no appropriate RVE can be found and it does not make sense to calculate effective properties. An example for a macroscopically inhomogeneous material is a graded material, i.e., a material which has a continuous variation of material properties.

Within the scale consideration shown in Figure 4.1, a material point on the macroscale is assigned a volume portion on the microscale. To define a homogeneous mechanical equivalent to the heterogeneous RVE, the volume average of the volume V of the stress and strain, respectively is taken

$$\langle \sigma_{ij} \rangle = \frac{1}{V} \int\limits_V \sigma_{ij}(x)\,\mathrm{d}V \tag{4.2}$$

$$\langle \varepsilon_{ij} \rangle = \frac{1}{V} \int\limits_V \varepsilon_{ij}(x)\,\mathrm{d}V \quad , \tag{4.3}$$

where the symbol $\langle \cdot \rangle$ denotes that $\langle \sigma_{ij} \rangle$ and $\langle \varepsilon_{ij} \rangle$ are averaged quantities.

If the homogeneous material is assumed to be purely elastic, the constitutive equation on the macroscale is

$$\langle \sigma_{ij} \rangle = C^*_{ijkl} \langle \varepsilon_{kl} \rangle \quad , \tag{4.4}$$

with the effective elasticity tensor C^*_{ijkl} which is is defined as the relation between the two averaged quantities $\langle \sigma_{ij} \rangle$ and $\langle \varepsilon_{kl} \rangle$.

4.2 Classical homogenization approaches

4.2.1 Voigt - Reuss bounds

A classical technique to determine effective properties of microstructured materials is the computation of upper and lower bounds according to VOIGT [56] and REUSS [41]. The theory is based on HILL's condition which states that the strain energy on the microscale must be equal to the strain energy on the macroscale. Thus,

$$\langle W^{micro} \rangle \overset{!}{=} W^{macro} \tag{4.5}$$

$$\frac{1}{2} \langle \boldsymbol{\sigma}(x) \colon \boldsymbol{\varepsilon}(x) \rangle \overset{!}{=} \frac{1}{2} \langle \boldsymbol{\sigma}(x) \rangle \colon \langle \boldsymbol{\varepsilon}(x) \rangle \tag{4.6}$$

must be satisfied (see equation (2.12) for the definition of the strain energy).

Within the computation of VOIGT bounds for the material properties, the RVE is subjected to a number of reference deformation states. It is assumed that the microscopic strain state is equal in every spatial point of the RVE, i.e.,

$$\langle \varepsilon_{ij} \rangle = \varepsilon_{ij}(x) = const \quad . \tag{4.7}$$

The implication of this assumption can be pictured by considering a one-dimensional two-phase material. The state of strain is assumed to be uniform over the whole RVE, which can only be accomplished by re-ordering the two phases of the material in parallel manner (see Figure 4.2). As boundary conditions, the displacements along boundaries are prescribed. The VOIGT bound provides upper bounds for the sought material parameters.

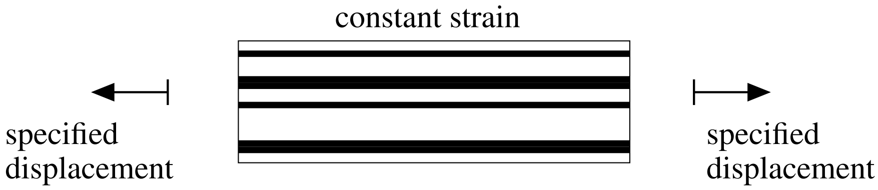

Figure 4.2: Intuitive interpretation of Voigt approximation

An analogous approach was introduced by Reuss. Contrary to Voigt, the state of stress is assumed to be constant, i.e.,

$$\langle \sigma_{ij} \rangle = \sigma_{ij}(x) = const \quad . \tag{4.8}$$

The interpretation of this approach is shown in Figure 4.3. Since the stress is assumed to be constant over the RVE, the two phases are put in series and the traction is prescribed along the boundaries. The Reuss bound provides lower bounds for the sought material parameters.

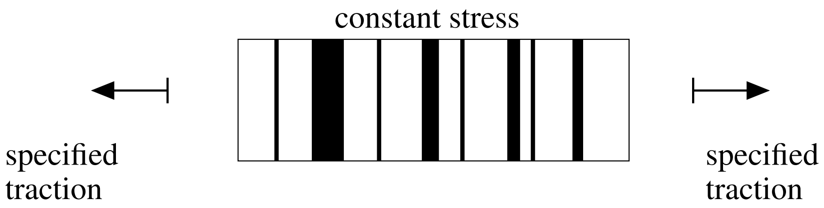

Figure 4.3: Intuitive interpretation of Reuss approximation

For the special case of materials with n phases which have piecewise constant properties, the Voigt and Reuss bounds can be calculated as [37]

$$\mathbf{C}^{*}_{(Voigt)} = \sum_{\alpha=1}^{n} c_\alpha \mathbf{C}_\alpha \tag{4.9}$$

$$\mathbf{C}^{*-1}_{(Reuss)} = \sum_{\alpha=1}^{n} c_\alpha \mathbf{C}^{-1}_\alpha \quad , \tag{4.10}$$

where $\mathbf{C}_i$ are the properties of the phases and c_i are the volume fractions of the phases. The real properties of the material lie in-between these bounds

$$\mathbf{C}^{*}_{(Reuss)} < \mathbf{C}^{*} < \mathbf{C}^{*}_{(Voigt)} \quad . \tag{4.11}$$

The quality of these bounds heavily depends on the considered microstructure. For fiber reinforced materials, for example, the Voigt bound may even deliver an exact solution. This is the case if the fibers are aligned in one direction and are perfectly bonded. The Voigt bound then delivers the exact solution for the Young's modulus in direction of the fibers. Perpendicular to this direction, the REUSS bound would deliver an exact solution. In the general case (i.e., the fibers are not aligned), however, the VOIGT and REUSS bounds are only rough estimates of the material properties.

4.2.2 Hashin - Shtrikman bounds

Improved bounds for effective material behavior have been developed by HASHIN and SHTRIKMAN. Details of the derivation and proofs can be found in the literature [23, 59] . The approach is based on variational principles using the concept of polarization of micro-macro mechanical fields. They represent the tightest possible bounds. In case of a two phase material with piecewise constant material properties, the bounds of the effective bulk modulus

$$K_1 + \frac{c_2}{\frac{1}{K_2 - K_1} + \frac{3c_1}{3K_1 - 4G_1}} \leq K^* \leq K_2 + \frac{c_1}{\frac{1}{K_1 - K_2} + \frac{3c_2}{3K_2 - 4G_2}} \tag{4.12}$$

and the bounds of the effective shear modulus

$$G_1 + \frac{5G_1 c_2}{\frac{5G_1}{G_2 - G_1} + \frac{6c_1(K_1 + 2G_1)}{3K_1 + 4G_1}} \leq G^* \leq G_2 + \frac{5G_2 c_1}{\frac{5G_2}{G_1 - G_2} + \frac{6c_2(K_2 + 2G_2)}{3K_2 + 4G_2}} \tag{4.13}$$

are derived, where the elastic constants K_n and G_n and the volume fraction c_n of the constituents for $n = 2$ materials serve as input data.

The VOIGT - REUSS and HASHIN - SHTRIKMAN bounds are classical homogenization techniques for multi-phase microstructures. In this context they are mentioned for the sake of completeness because cellular materials posses at least one phase with a vanishing stiffness. Therefore, the lower bounds for both bounding techniques are 0, e.g.

$$\mathbf{C}^*_{(Reuss)} \rightarrow \mathbf{0} \tag{4.14}$$

for the REUSS bound. This makes the bounding techniques unsuitable for cellular materials.

4.2.3 Strain energy based homogenization

BECKER and HOHE have developed a homogenization procedure for the determination of material parameters of cellular materials. An overview is given in [24, 27]. Like the VOIGT - REUSS bounds, the procedure is also based on a strain energy approach. Equivalence of the mechanical behavior of the Representative Volume Element and the effective medium is assumed, if the average strain energy density is equal for both volume elements

$$\frac{1}{V} \int\limits_{\Omega_{RVE}} W(\varepsilon_{ij}) \mathrm{d}\Omega_{RVE} \overset{!}{=} \frac{1}{V} \int\limits_{\Omega_{RVE}} W^*(\varepsilon^*_{ij}) \mathrm{d}\Omega_{RVE} \tag{4.15}$$

where W and W^* denote the strain energy of the heterogeneous and homogeneous medium for equivalent strain states. Equivalence of the micro and macro strain states ε_{ij}, ε^*_{ij} is assumed if the volume average of the infinitesimal strain tensors is equal

$$\frac{1}{V}\int\limits_{\Omega_{RVE}} \varepsilon_{ij} \mathrm{d}\Omega_{RVE} = \frac{1}{V}\int\limits_{\Omega_{RVE}} \varepsilon^*_{ij} \mathrm{d}\Omega_{RVE} \quad . \tag{4.16}$$

If a linear elastic behavior of the material on the macroscale is assumed, the following values for the tensorial components are derived

$$C_{ijkl} = \begin{cases} 2W^*(\varepsilon_{(ij)})\frac{1}{\varepsilon^{*2}_{(ij)}} & \text{if } i=j, k=l, i=k \\ \frac{1}{2}W^*(\varepsilon_{(ij)})\frac{1}{\varepsilon^{*2}_{(ij)}} & \text{if } i\neq j, k\neq l, i=k, j=l \\ \begin{array}{l}\big(W^*(\varepsilon_{(ij)},\varepsilon_{(kl)}) - W^*(\varepsilon_{(ij)}) \\ \qquad -W^*(\varepsilon_{(kl)})\big)\,\frac{1}{\varepsilon^*_{(ij)}\varepsilon^*_{(kl)}}\end{array} & \text{if } i=j, k=l, i\neq k \\ \begin{array}{l}\frac{1}{4}\big(W^*(\varepsilon_{(ij)},\varepsilon_{(kl)}) - W^*(\varepsilon_{(ij)}) \\ \qquad -W^*(\varepsilon_{(kl)})\big)\,\frac{1}{\varepsilon^*_{(ij)}\varepsilon^*_{(kl)}}\end{array} & \text{if } i\neq j, k\neq l, i\neq k \text{ or } j\neq l \\ \begin{array}{l}\frac{1}{2}\big(W^*(\varepsilon_{(ij)},\varepsilon_{(kl)}) - W^*(\varepsilon_{(ij)}) \\ \qquad -W^*(\varepsilon_{(kl)})\big)\,\frac{1}{\varepsilon^*_{(ij)}\varepsilon^*_{(kl)}}\end{array} & \text{if } i=j, k\neq l \end{cases} \quad . \tag{4.17}$$

$W^*(\varepsilon_{(ij)},\varepsilon_{(kl)})$ denotes the strain energy density in the Representative Volume Element subjected to a strain state where all components of the strain tensor except $\varepsilon_{(ij)}$ and $\varepsilon_{(kl)}$ are equal to 0. The brackets () denote that no summation is performed. Thus, the Representative Volume Element is considered to be deformed by a number of reference strain states for which the strain energy has to be evaluated. The procedure was developed for cellular materials, where the cell walls consist of straight beams. Deformations and strain energy can be calculated analytically in this case. A generalization for more general microstructure geometries is given in [25, 26].

4.2.4 Surface average based approach

Within the scale consideration shown in Figure 4.1, a material point on the macroscale is assigned a volume portion on the microscale. To define a homogeneous mechanical equivalent to the heterogeneous RVE, a surface average based approach is used. The stress distribution in the Representative Volume Element consisting of the given microstructure is assumed to be equivalent to a stress distribution of the effective medium if

$$\frac{1}{\Gamma}\int\limits_{\Gamma^i_{RVE}} \mathbf{t}_i \,\mathrm{d}\Gamma = \frac{1}{\Gamma}\int\limits_{\Gamma^i_{RVE}} \langle \mathbf{t}_i \rangle \,\mathrm{d}\Gamma \tag{4.18}$$

holds, where $\mathbf{t}_i$ is the traction vector on the surface Γ of the Representative Volume Element and Γ^i is a certain part of its boundary. Equation (4.18) describes a redistribution of the stress components along the surface of the Representative Volume Element during the homogenization process. A second equivalence condition interrelates the strain states on the microscopic and macroscopic scale. An average strain state for the Representative Volume Element is defined by means of the difference in the displacements of opposite surfaces of the volume element. If the difference in the displacements of opposite surfaces is not constant along the surface, the surface integral of this quantity is taken. Thus, the macroscopic strain can be expressed by

$$\langle \varepsilon_{ij} \rangle = \frac{1}{2V} \int\limits_{\Gamma_{RVE}} \left(u_i n_j + u_j n_i \right) \, \mathrm{d}\Gamma, \tag{4.19}$$

where V denotes the volume of the RVE and n_i are the components of the outward normal vector on Γ_{RVE}. Thus, the heterogeneous microstructure is smeared over the RVE (see Figure 4.4). With the averaged stress and strain, the effective macroscopic material properties are calculated via

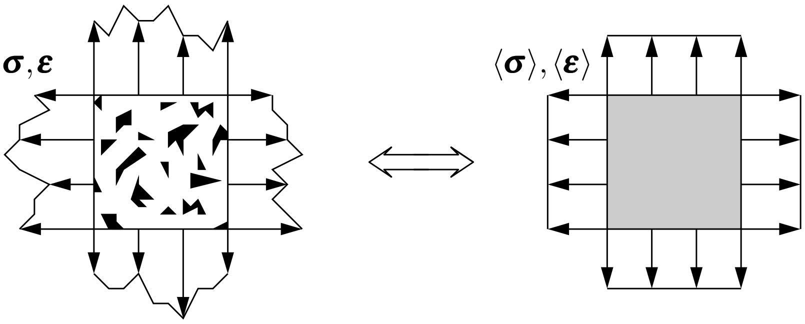

Figure 4.4: Stress and strain on the micro- and macroscale

$$\langle \sigma_{ij} \rangle = C^{*}_{ijkl} \, \langle \varepsilon_{kl} \rangle \quad , \tag{4.20}$$

with the effective elasticity tensor C^{*}_{ijkl} which is defined as the relation between the two averaged quantities $\langle \sigma_{ij} \rangle$ and $\langle \varepsilon_{kl} \rangle$.

The advantage of this approach is that it only requires the tractions and deformations on the boundary of the RVE. No energetic considerations like in the strain energy based homogenization are made. Thus, it can not only be applied in the static case, but also in dynamics. Since the materials discussed in this work are assumed to have a periodic microstructure, it is meaningful to do a dynamic calculation in frequency domain. The reason is that in frequency domain, periodic boundary conditions can be applied to the RVE. In time domain, this is not possible because wave propagation phenomena take place. Thus, if a wave is running through the RVE, the tractions and displacements on one edge are different from the tractions and displacements on the opposing edge. It is not possible to fulfill the periodicity, which is postulated from the fact that the material consists of equally shaped cells. In a frequency domain calculation, in contrast, the RVE is situated in a steady state where periodicty can be fulfilled.

Calculation on Microscale

The aim of homogenization is to calculate effective properties, which in the elastic case means that the components of C^*_{ijkl} of equation (4.4) need to be found. C^*_{ijkl} has 21 independent components in the general, anisotropic case. The RVE is subjected to a number of strain states. A useful choice of load states is

$$\langle\sigma_{ij}\rangle \quad \text{or} \quad \langle\varepsilon_{kl}\rangle = \begin{bmatrix} \beta & 0 & 0 \\ 0 & 0 & 0 \\ 0 & 0 & 0 \end{bmatrix}, \begin{bmatrix} 0 & 0 & 0 \\ 0 & \beta & 0 \\ 0 & 0 & 0 \end{bmatrix}, \begin{bmatrix} 0 & 0 & 0 \\ 0 & 0 & 0 \\ 0 & 0 & \beta \end{bmatrix},$$
$$\begin{bmatrix} 0 & \beta & 0 \\ \beta & 0 & 0 \\ 0 & 0 & 0 \end{bmatrix}, \begin{bmatrix} 0 & 0 & 0 \\ 0 & 0 & \beta \\ 0 & \beta & 0 \end{bmatrix}, \begin{bmatrix} 0 & 0 & \beta \\ 0 & 0 & 0 \\ \beta & 0 & 0 \end{bmatrix} \quad . \qquad (4.21)$$

The RVE can either be subjected to a strain load where the stress is computed or vice versa. The load factor β can be chosen arbitrarily. The states in (4.21) assure that all unknowns in C^*_{ijkl} can be computed. If the cases are not independent, linear combinations of the equations occur and there are not enough equations to compute all tensor components of C^*_{ijkl} [13].

In 2-D, 3 independent load cases suffice. To assure that all material parameters can be determined, the three loadcases shown in Figure 4.5 can be applied. If the plane stress case is considered, all Q_{ijkl} of equation (2.41) can be calculated. This can easily be seen, because the three loadcases correspond to the three rows of equation (2.41).

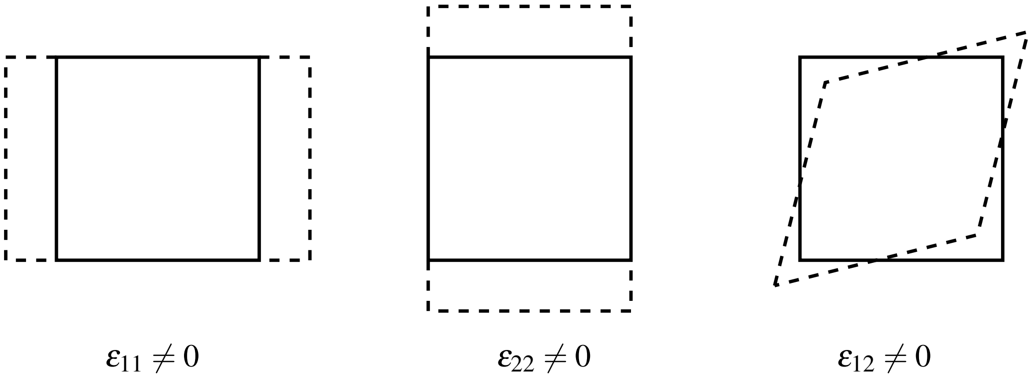

Figure 4.5: Independent load cases in 2-D

Boundary Conditions

The cellular structures are assumed to be periodic, i.e., they consist of equally shaped unit cells. If the microstructure is deformed, neighboring cells undergo the same deformation pattern. The whole macroscopic body consists of identical parts that fit into each other. In Figure 4.6, a two-dimensional unit cell is shown in deformed and undeformed state. The

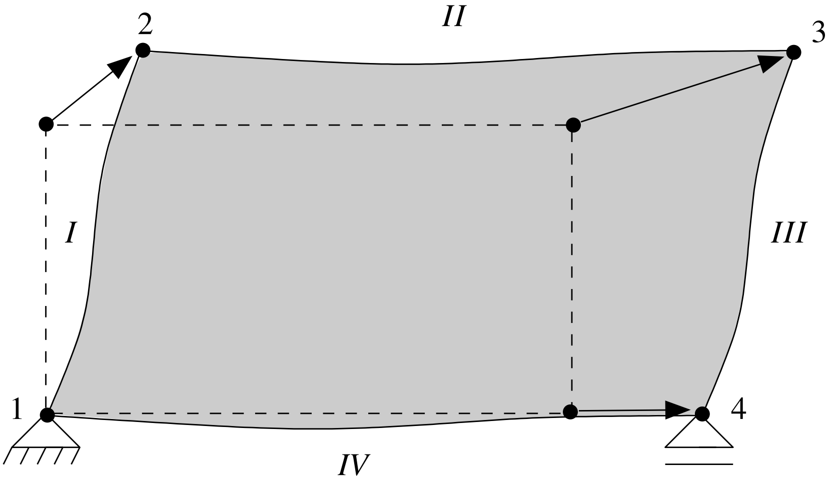

Figure 4.6: Periodic boundary conditions

corner nodes are named with arabic numbers 1 to 4 and the edges are named with roman numbers *I* to *IV*. Periodic boundary conditions are achieved by pairing opposite faces and linking the corresponding degrees of freedom with each pair of faces. Thus, for the displacement vectors **u** of the nodes or edges, the following symbolic equations must be fulfilled

$$\mathbf{u}_{II} = \mathbf{u}_{IV} + \mathbf{u}_2 \quad ; \quad \mathbf{u}_{III} = \mathbf{u}_I + \mathbf{u}_4 \quad ; \quad \mathbf{u}_3 = \mathbf{u}_2 + \mathbf{u}_4 \quad . \tag{4.22}$$

The displacements at the 'slave faces', *II* and *III*, are determined by those of the "master faces", *I* and *IV*, and of the 'master nodes' 2 and 4. See also [24, 5] for a more detailed description. If the stresses **t** are discretized in addition to the displacements like in the method described in chapter 3, they have to fulfill anti-periodic conditions, i.e.,

$$\mathbf{t}_{II} = -\mathbf{t}_{IV} \quad ; \quad \mathbf{t}_{III} = -\mathbf{t}_I \quad ; \qquad . \tag{4.23}$$

For unit cells which are symmetric in an undeformed and deformed state, the periodic boundary conditions simplify to symmetric boundary conditions (see Figure 4.7). Due

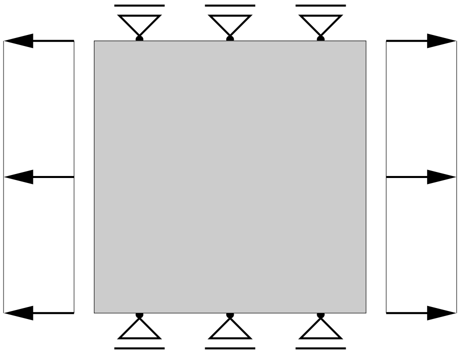

Figure 4.7: Periodic boundary conditions due to symmetry

to the symmetry of unit cell and boundary conditions, the deformations on the left edge correspond to the deformations on the right edge and the tractions on the upper edge are equal to the tractions on the lower edge.

The periodicity of the boundary conditions needs to be fulfilled in a static calculation as well as in a dynamic calculation. This makes a dynamic calculation in frequency domain meaningful.

4.2.5 Unit Cell versus RVE

Within this work, cellular solids are considered which consist of simple beams. Such structures are found quite often in literature, they can represent sandwich cores or simplified models of foam-like materials. As has been mentioned before, it is assumed that the material is periodic, i.e., it consists of equally shaped cells. For sandwich cores, this assumption is well justified, real materials, of course, have an imperfect microstructure, where neighbouring cells have a slightly different geometry. The cork tree, for example, consists of hexagonal cells as can be seen in Figure 4.8. A model for this material is also shown in Figure 4.8. The model consists of perfect hexagonal cells, neglecting small imperfections of the real material. In order to calculate effective, homogeneous material properties, this model would be sufficiently accurate to represent the microstructure. If the assumption of periodicity is made, it is very easy to find a RVE, because if the microstructure consists of identical units, the smallest unit contains all information and is therefore representative. In statics, effective properties can be calculated from this single unit cell. In a frequency domain calculation, however, one unit cell does not suffice to obtain representative results. The reason is that higher modes of deformation may occur when using a different number of unit cells. This can be explained by considering the example given in Figure 4.9. A unit cell is loaded with a force on the left and right hand side. The cell is calculated in frequency domain, i.e., the load is harmonic and thus, the resulting strain

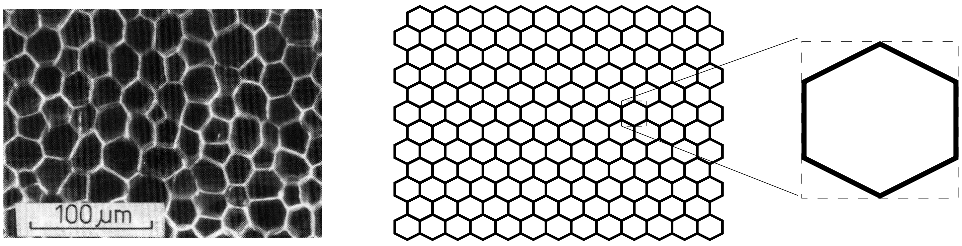

Figure 4.8: Microstructure of cork, idealized model and unit cell

$$\varepsilon = \frac{\Delta \ell}{\ell} \tag{4.24}$$

is also harmonic. Another calculation is done using 3 × 3 cells. Both strains are plotted over a frequency range of $0..10^6$ Hz in logarithmic scale, see Figure 4.10. On the left hand side, the whole frequency range is plotted, whereas on the right hand side, only a small

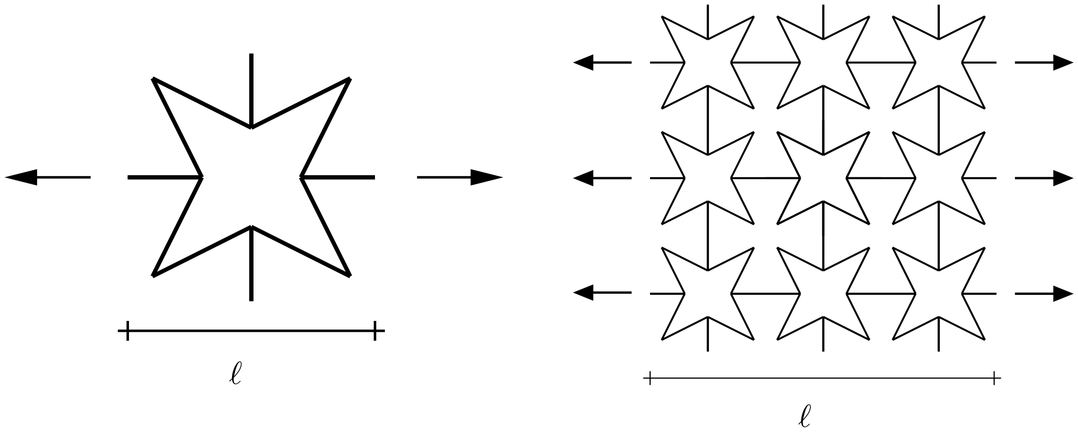

Figure 4.9: Example calculation of 1 and 3 × 3 unit cells

range is plotted. It can be seen that the results from both calculations are not identical. At approximately $3.4 \cdot 10^5$ Hz, an eigenfrequency is missing in the single unit cell calculation and at $2.3 \cdot 10^5$ Hz, the eigenfrequencies of both calculations are different. Therefore, it is necessary to calculate multiple unit cells to obtain characteristic microscale results. A simple and pragmatic approach is to calculate a specific number of unit cell and then average the results.

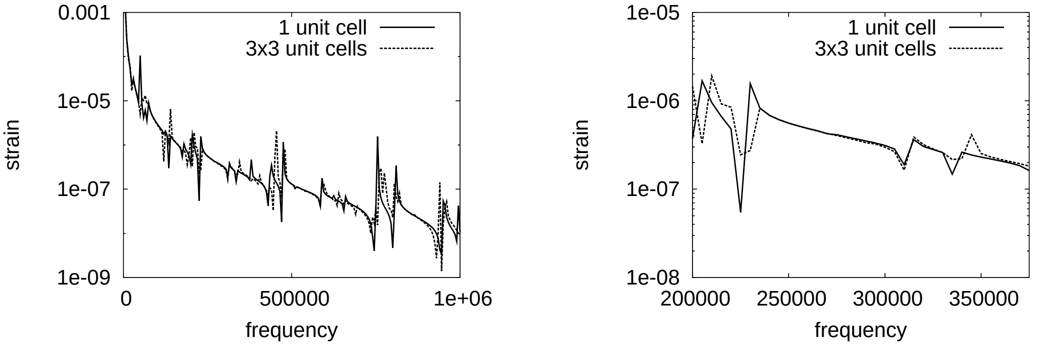

Figure 4.10: Strain of 1 and 3 × 3 unit cells

5 OPTIMIZATION

The term optimization refers to the study of problems in which one seeks to minimize or maximize a function by systematically choosing the values of variables from an allowed set. In the context of this work, optimization techniques are used to obtain macroscopic material parameters, i.e, 'try to find material parameters on the macroscopic scale which describe the micromechanical properties as good as possible'.

Within the scope of this work, the Simplex Method and the Sequential Quadratic Programming Method are used. They represent gradient-based optimization techniques. These algorithms often exhibit weaknesses in non-convex problems, which means that they can run into local minima of the search space. Therefore, two global optimization techniques, a Genetic Algorithm and a Neural Network are also applied to the optimization problem.

5.1 Simplex Algorithm

The Simplex Algorithm is a classical optimization algorithm. Subject to constraints, an optimization function $f(x_1, x_2, \ldots, x_n)$ is minimized or maximized. The method uses the concept of a simplex, which is a polytope of $(n+1)$ vertices in n dimensions: a line segment on a line, a triangle on a plane, a tetrahedron in three-dimensional space and so forth. The simplex is defined by the constraints.

A starting point is chosen, which is the first vertex of the simplex. The vertex of the simplex with the largest function value is reflected in the center of gravity of the remaining vertices and the function value at this new point is compared with the remaining function values. Depending on the outcome of this test the new point is accepted or rejected, a further expansion move may be made, or a contraction may be carried out. When no further progress can be made the sides of the simplex are reduced in length and the method is repeated [40].

5.2 SQP - Sequential Quadratic Programming

Sequential quadratic programming methods are the standard general purpose algorithms for solving nonlinear optimization problems.

In general, the optimization task can be stated by

$$\min f(\mathbf{x}) \tag{5.1a}$$
$$g_j(\mathbf{x}) = 0, \quad j = 1, \ldots, m_e \tag{5.1b}$$
$$g_j(\mathbf{x}) \geq 0, \quad j = m_e + 1, \ldots, m \tag{5.1c}$$
$$\mathbf{x}_{\text{lower}} \leq \mathbf{x} \leq \mathbf{x}_{\text{uppper}} \tag{5.1d}$$

where $f(\mathbf{x})$ is the function to be minimized and equations (5.1b-5.1d) are constraints. A solution of the nonlinear optimization problem can be obtained by considering the related Lagrange-function, which is defined as

$$L(\mathbf{x}, \mathbf{u}) = f(\mathbf{x}) - \sum_{j=1}^{m} u_j g_j(\mathbf{x}) \tag{5.2}$$

with the Lagrange-multipliers u_j. The SQP-method is an iterative approach. In the k-th iteration step a new solution point $\mathbf{x}_{k+1}$ is calculated via

$$\mathbf{x}_{k+1} = \mathbf{x}_k + \alpha_k \mathbf{d}_k \quad . \tag{5.3}$$

The parameter α_k is the positive step size and $\mathbf{d}_k$ is the search direction. To obtain $\mathbf{d}_k = (\mathbf{x} - \mathbf{x}_k)$, the quadratic subproblem

$$\min \left(\mathbf{g}^T (\mathbf{x} - \mathbf{x}_k) + \frac{1}{2} (\mathbf{x} - \mathbf{x}_k)^T \mathbf{H}_k (\mathbf{x} - \mathbf{x}_k) \right) \tag{5.4}$$

needs to be solved with

$$g_i(\mathbf{x}_k) + \frac{\partial g_i(\mathbf{x}_k)}{\partial x_i} = 0 \qquad i = 1, \ldots, m_e \tag{5.5}$$
$$g_i(\mathbf{x}_k) + \frac{\partial g_i(\mathbf{x}_k)}{\partial x_i} \geq 0 \qquad i = m_e + 1, \ldots, m \quad . \tag{5.6}$$

The quadratic subproblem is obtained by approximating the Lagrange-function with a Taylor-series, neglecting higher order terms. It can be solved using any Quadratic Programming method. In equation (5.4), $\mathbf{H}_k$ denotes the Hessian matrix. Often, $\mathbf{H}_k$ is approximated with the BROYDEN-FLETCHER-GOLDFARB-SHANNON (BFGS) procedure

$$\mathbf{H}_{k+1} = \mathbf{H}_k \frac{\mathbf{H}_k \mathbf{s}_k \mathbf{s}_k \mathbf{H}_k}{\mathbf{s}_k^T \mathbf{H}_k \mathbf{s}_k} + \frac{\mathbf{y}_k \mathbf{y}_k^T}{\mathbf{y}_k^T \mathbf{s}_k} \tag{5.7}$$

with

$$\mathbf{s}_k = \mathbf{x}_{k+1} - \lambda_k \tag{5.8}$$
$$\mathbf{y}_k = \nabla_x L(\mathbf{x}_{k+1}, \lambda_k) - \nabla_x L(\mathbf{x}_k, \lambda_k) \quad , \tag{5.9}$$

where λ_k is an estimate of a Lagrange-multiplier. After the computation of the descent direction $\mathbf{d}_k$ an appropriate step length parameter α_k must be determined. This can be done by defining a merit function, which is minimized. Usually, the extended Lagrangian function

$$L(\mathbf{x},\mathbf{u},\mathbf{s}) = f(\mathbf{x}) + \sum_{i=m_e+1}^{m} u_i(g_i(\mathbf{x}) - s_i) + \frac{1}{2}\sum_{i=m_e+1}^{m} u_i(g_i(\mathbf{x}) - s_i)^2 \quad . \tag{5.10}$$

is used. Other merit functions are also possible. An extensive overview of SQP-methods is given in [18] or [48].

5.2.1 Local Minima

The problem of local minima in optimization can be explained with a simple example. The function

$$f(x) = \frac{1}{4}x^4 - \frac{13}{3}x^3 + 25x^2 - 56x + 60 \tag{5.11}$$

shall be minimized within the limits

$$0 < x < 10 \quad . \tag{5.12}$$

With simple differentiation the function's minima are found to be at $(2, \frac{52}{3})$ and $(7, \frac{83}{12})$. For the minimization, the MATLAB-routine `fmincon`, which uses a Sequential Quadratic Programming Method, is used. The starting point is chosen to be $x_{start} = 3.9$. With a requested precision of 10^{-5}, the iteration stops after only 7 steps, the search path of the algorithm is shown in Figure 5.1. As can be observed, the gradient-based method always searches a new point in the direction of the function's slope. Due to the chosen starting point, the algorithm runs into the local minimum at $x = 2$, the global minimum at $x = 7$ is not found. This is a general problem of gradient-based optimization procedures: Depending on the starting point, these algorithms can run into local minima. On the other hand, the search is relatively quick.

5.3 Genetic Algorithm

Genetic Algorithms are stochastic search techniques that use principles inspired by evolutionary biology such as inheritance, mutation, natural selection, and recombination. The fundamental idea is to randomly create a number of solutions for a problem, select the best ones and modify them with techniques adopted from nature to obtain an optimal solution.

At the beginning of a Genetic Algorithm, a *population* with a specific number of candidate solutions (*individuals*) is generated. The individuals represent the solutions of an optimization problem. In general they can be created randomly, however, if there is information for admissible solutions (restrictions, etc.) it is advisable to use it in order to quicken the optimization. An individual is made up of a number of *chromosomes* (sometimes also termed

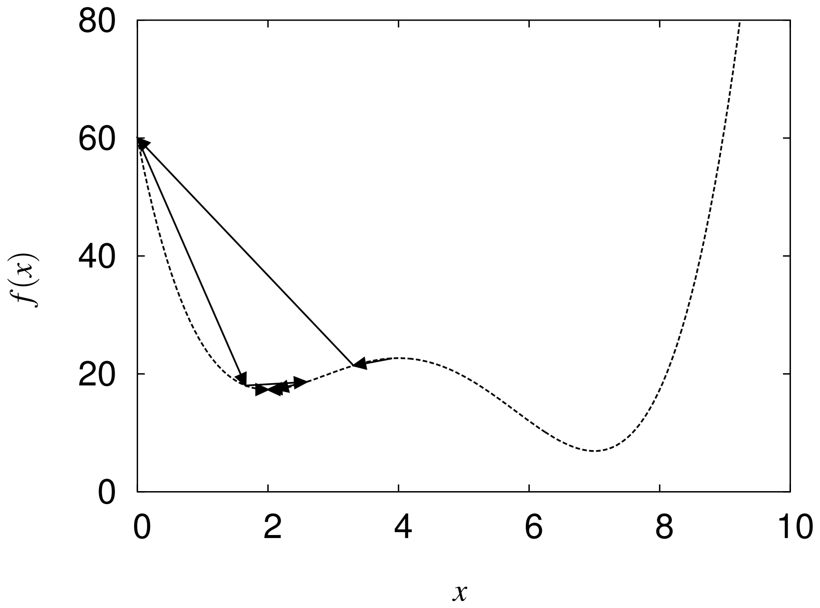

Figure 5.1: Local minimum of SQP optimization

genomes) which represent a particular aspect of the solution. One common approach is to encode solutions as binary strings with each chromosome containing either 1 or 0 (see Figure 5.2). The binary code can represent integers or real-valued parameters of the solution. Another, similar approach is to encode solutions directly with integers or decimal numbers (one number $\hat{=}$ one chromosome). This coding can often be 'intuitively closer to the problem space' [16].

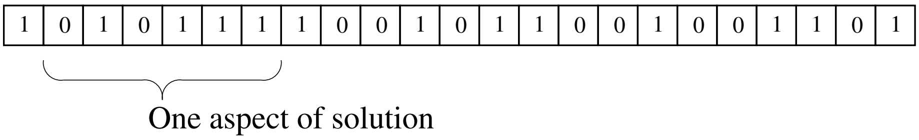

Figure 5.2: Binary coded individual

After the creation of the first population, each individual is evaluated according to a *fitness function*, i.e., for every individual, a fitness value is calculated which rates the 'quality' of the individual. For a minimization problem, a very low fitness value reflects a good quality, whereas for a maximization problem it reflects a poor quality. Next, the population is sorted by the fitness value - the individual with the best fitness takes in first place, followed by the second-best and so on. A number n of the poorest individuals are usually eradicated (*survival of the fittest*), these individuals are not allowed to produce offspring while the better ones constitute the parent population for the next generation. The forming of the offspring generation is done using any or all of the genetic operators:

- Selection
  individuals are chosen for later breeding. Common procedures for selection are:
  - Proportional fitness
    an individuals chance to reproduce is proportional to its fitness value
  - Tournament selection
    randomly selected individuals in a subgroup compete and the fittest one is selected
- Recombination
  selected individuals are recombined. Usually, chromosome exchange and crossover are used:
  - Chromosome exchange
    between two individuals, the m-th chromosome is exchanged with a probability q_{ce}.
  - One-point-crossover
    with a probability q_{co}, two selected individuals exchange chromosome groups from a specific chromosome position A to the end (see Figure 5.3).

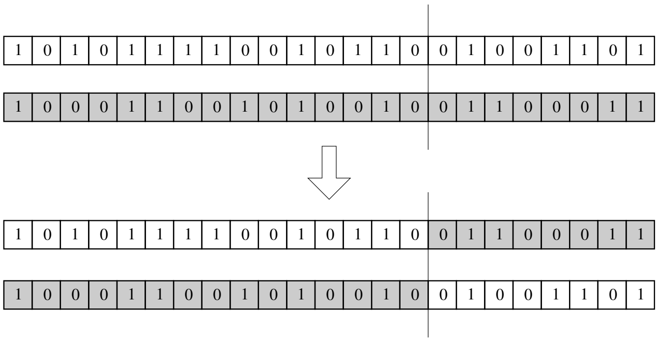

Figure 5.3: One-point-crossover

  - Two-point-crossover
    with a probability q_{co}, two selected individuals exchange chromosome groups from a specific position A to a position B (see Figure 5.4).
- Mutation
  The value of a chromosome is mutated with a probability p_{mu}, thus, for a binary-coded individual one chromosome value is changed from 1 to 0 or vice-versa (see Figure 5.5).

Next to the individuals that are generated by recombination or mutation, also newly created individuals can be added to the new generation or the best individuals of the parent generation are left unchanged and added to the new generation (*elite selection strategy*). Once the new population is created, one iteration step is completed and the new individuals

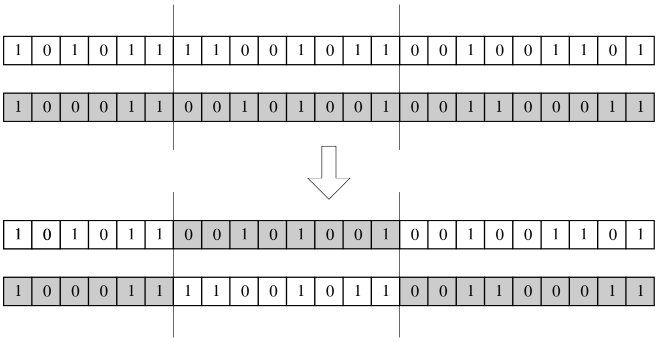

Figure 5.4: Two-point-crossover

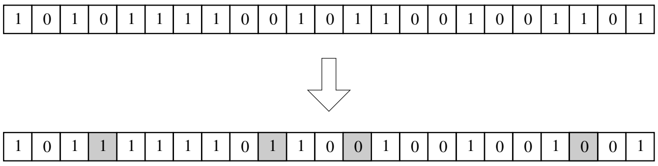

Figure 5.5: Mutation

are evaluated and used to create the following generation. The iteration is halted if a specific number of iterations is exceeded or if the best individual of a generation has reached a specific fitness. Figure 5.6 shows the above described steps in a flowchart.

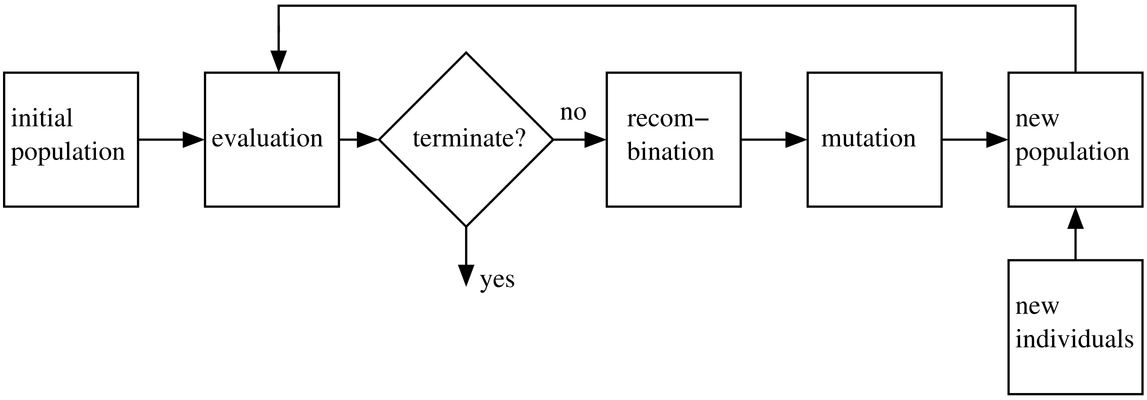

Figure 5.6: Genetic algorithm

Genetic algorithms are often applied as an approach to solve global optimization problems. They are in particular useful in problem domains that have a complex fitness landscape as recombination is designed to move the population away from local minima that a traditional gradient-based algorithm might run into. There exist many different forms of Genetic Algorithms and the user usually has to set a broad range of parameters.

5.4 Neural Network

Neural networks are composed of simple elements, *neurons*, operating in parallel. The network function is determined primarily by the connections between the neurons. These connections are adjusted or weighted during a training or learning phase so that a particular input leads to a specific output. When the training is finished, the adjusted network can be used to solve a problem. See Figure 5.7 for the training of the Neural Network. The training phase is much more time-consuming than the actual application, which makes a neural network particularly suitable for real-time applications.

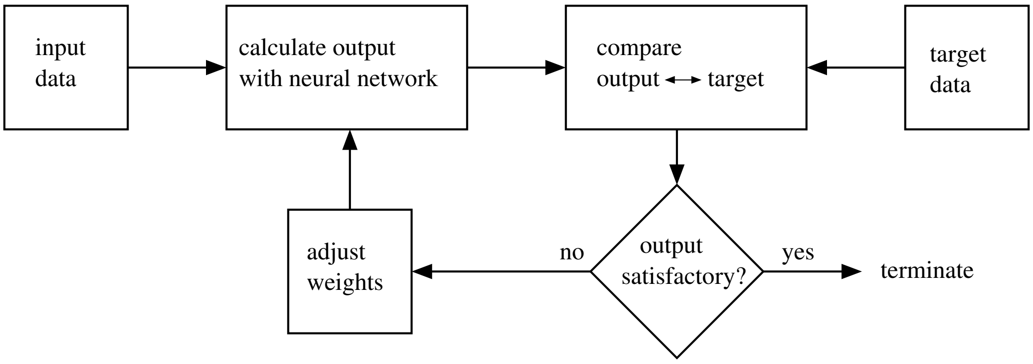

Figure 5.7: Training of Neural Network

Neural networks are inspired from nature. The human brain consists of a large number of neurons which perform a simple 'calculation' and give their output to other neurons. The biological neurons are 'adjusted' (trained) and act in a parallel manner. Figure 5.8 is a schematic drawing of a Neural Network that consists of an input layer, a hidden layer and an output layer. The input layer consists of n_{in} neurons, corresponding to one set of input data with n_{in} elements. The number of neurons in the hidden layer can be chosen somewhat arbitrarily. Theoretically, it is possible to construct a Neural Network with more than one hidden layer although most applications feature only a single hidden layer. The output layer consists of n_{out} neurons, corresponding to an output data set with n_{out} elements.

The neurons of the layers have weighted connections among each other. Thus, one neuron of the hidden layer has n_{in} weighted inputs, as can be seen in Figure 5.9. The output of the neuron is calculated via

$$a_1^2 = f^1(n) \quad , \tag{5.13}$$

where n is the sum of all outputs of the input layer

$$n = \sum_{i=1}^{n_{in}} a_i \cdot w_{1,i} + b \quad , \tag{5.14}$$

f is a transfer function and b is a bias. Typical choices for f are the *sigmoid* function $f = 1/(1+e^{-x})$ or the *tangens hyperbolicus* function. The transfer function f is employed for the network to be able to identify nonlinear interrelationships.

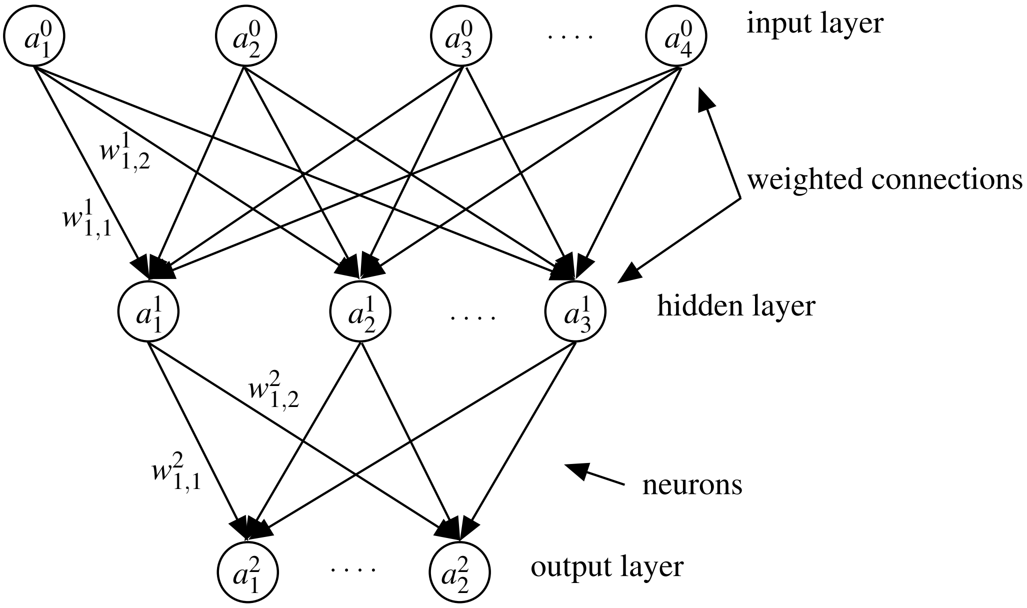

Figure 5.8: Neural Network with one hidden layer

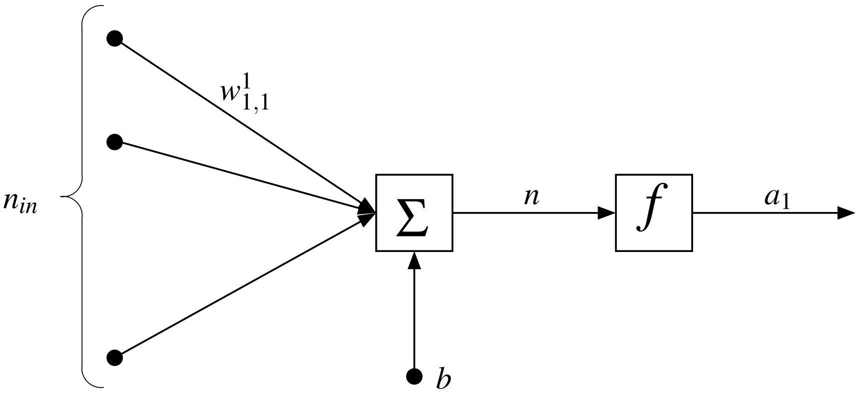

Figure 5.9: Single neuron

The training of the Neural Network can be done using the backpropagation algorithm. The summary of the technique is as follows:

- Present a training sample to the Neural Network.
- Compare the network's output to the desired output from that sample. Calculate the error in each output neuron.
- For each neuron, calculate what the output should have been, and a scaling factor, how much lower or higher the output must be adjusted to match the desired output.
- Adjust the weights of each neuron to lower the local error.
- Repeat the steps above on the neurons at the previous level.

The training is finished if certain criteria are fulfilled, for example if a specific error tolerance is reached or if the number of iterations exceeds a given value. As the algorithm's name implies, the errors (and therefore the learning) propagate backwards from the output nodes to the inner nodes. So backpropagation is used to change the network's modifiable weight accordingly to the error.

The advantage of a Neural Network is the very quick application. After the very time-consuming training, the application of the Network is much quicker than other optimization procedures.

6 EFFECTIVE PROPERTIES IN STATICS

The surface average based homogenization strategy proposed in section 4.2.4 is now realized in the static case using the optimization techniques given in chapter 5. Since in statics, an analytic solution of the homogenization problem is possible, the analysis is mainly done to test the different optimization procedures with respect to what they can accomplish and what advantages and disadvantages they have. The following example calculations are done in the two-dimensional case, the generalization to the 3-D case is possible without further considerations. Firstly, a number of beam-type microstructures are examined. Secondly, a plate is considered with a star-shaped hole.

6.1 Beam-type microstructures

In order to calculate effective properties of a material, the components Q_{ijkl} of the linear elastic constitutive equation have to be determined. The plane stress case is considered on the macroscopic scale, so the 6 distinct Q_{ijkl} of

$$\begin{bmatrix} \sigma_{11} \\ \sigma_{22} \\ \sigma_{12} \end{bmatrix} = \begin{bmatrix} Q_{1111} & Q_{1122} & Q_{1112} \\ Q_{2211} & Q_{2222} & Q_{2212} \\ Q_{1211} & Q_{1222} & Q_{1212} \end{bmatrix} \begin{bmatrix} \varepsilon_{11} \\ \varepsilon_{22} \\ \varepsilon_{12} \end{bmatrix} \tag{6.1}$$

are sought.

Three different unit cells (see Figure 6.1) are used for the numerical study. The cell walls consist of steel with a Young's modulus of $E = 2.1 \times 10^{11}\mathrm{N/m}^2$ and a quadratic cross-section of $A = 10^{-8}\mathrm{m}^2$. The unit cells are calculated with the boundary element formulation described in chapter 3. In the static case, a Finite Element formulation could have

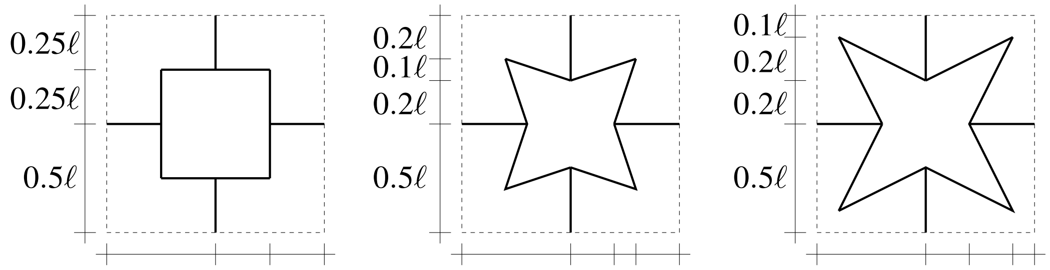

Figure 6.1: Microstructures for numerical study

been applied as well because a FEM calculation with shape functions of order three (e.g. Hermite-polynomials) gives exact results in the static case. The unit cells are subjected to the three independent load cases shown in section 4.2.4 (see Figure 4.5). As boundary conditions, the deformation at the boundary points are prescribed and the forces at these points are calculated. Thus, as a result on the microscale, a set of stresses $(\sigma_{11}, \sigma_{22}, \sigma_{12})$ and strains $(\varepsilon_{11}, \varepsilon_{22}, \varepsilon_{12})$ is obtained for each loadcase.

After the calculation on the microscale, an optimization procedure is used to obtain adequate material parameters Q_{ijkl} of equation (6.1). The optimization is formulated as a minimization problem, i.e., certain parameters need to be found to minimize a target function. An optimal solution is found if the function value is 0. As target function, the mean square error between the stress on micro- and macroscale is used

$$f = \sum_{n=1}^{3} \left(\sigma_{11n}^{micro} - \sigma_{11n}^{macro}\right)^2 + \left(\sigma_{22n}^{micro} - \sigma_{22n}^{macro}\right)^2 + \left(\sigma_{12n}^{micro} - \sigma_{12n}^{macro}\right)^2 . \tag{6.2}$$

In equation (6.2), n denotes the loadcase, so the difference of stress is summed up over all three loadcases. The stress components on the microscale σ_{ijn}^{micro} have to be calculated only once – with respect to the optimization they are constant input data. The stress on the macroscopic scale σ_{ijn}^{macro}, however, is calculated repeatedly for different Q_{ijkl} in the course of the optimization via equation (6.1).

In the following sections, results are presented for the four different optimization strategies.

Genetic Algorithm

Each individual of a Genetic Algorithm has a fitness value which reflects the individuals quality. The fitness value is calculated from a fitness function which in the present case is the target function f in equation (6.2). The material parameters Q_{ijkl} represent the chromosomes of the individuals. There are a total of 9 Q_{ijkl}, however, due to the symmetry, 6 of them are independent. Therefore, each individual consists of 6 chromosomes.

A Genetic Algorithm has a broad range of parameters that need to be set. Parameters such as population size or type of genetic operators need to be chosen. For the present application, the following parameters were used:

- A population size of 100 individuals is chosen
- The starting population is created randomly
- New individuals are created via 2-point-crossover
- The mutation of an individual is done accordingly to the standardized normal distribution
- 50 individuals are created newly in one generation, the remaining 50 are created as offspring of the previous generation

- The optimization is stopped after a maximum of 500 iterations or if the best fitness value is smaller than 10^{-5}

These parameters were determined in a trial-and-error process and have shown to deliver good results. Figure 6.2 shows the performance of the Genetic Algorithm. The fitness value of the best individual of a generation is plotted versus the number of generations. The plot is done for the star-shaped cell on the right hand side of Figure 6.1. Since the starting population is generated randomly, three optimization runs were done. At the beginning of the optimization, the progress of the algorithm is good, but after 40 – 50 generations, the improvement of the fitness value is rather small. The sought material parameters were all found with the Genetic Algorithm, see Table 6.1. The deviation from the exact solution is given in Table 6.2. The exact solution can be calculated by solving the constitutive equation (6.1) for the sought Q_{ijkl}. This is done for the three independent loadcases. In the first loadcase, for example, only the strain ε_{11} is not equal to 0, so the corresponding equation is

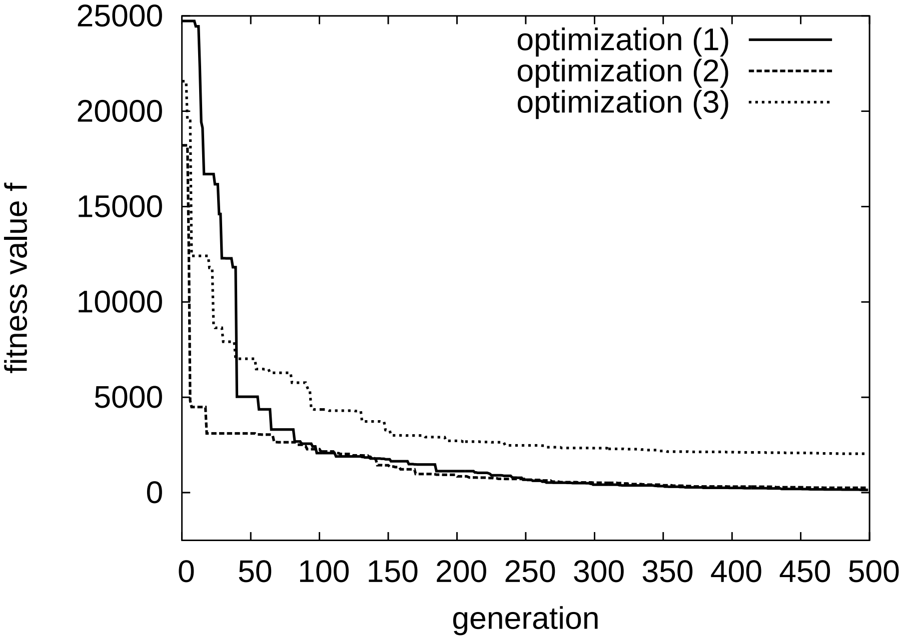

Figure 6.2: Performance of Genetic Algorithm

$$\begin{bmatrix} \sigma_{11} \\ \sigma_{22} \\ \sigma_{12} \end{bmatrix} = \begin{bmatrix} Q_{1111} & Q_{1122} & Q_{1112} \\ Q_{2211} & Q_{2222} & Q_{2212} \\ Q_{1211} & Q_{1222} & Q_{1212} \end{bmatrix} \begin{bmatrix} \varepsilon_{11} \\ \varepsilon_{22} = 0 \\ \varepsilon_{12} = 0 \end{bmatrix} . \tag{6.3}$$

Equation (6.3) can be solved for Q_{1111}, Q_{2211} and Q_{1211}.

Neural Network

A Neural Network is now used to determine effective properties of the given microstructures. In a first step, a Neural Network needs to be created and trained to solve the given problem.

Training of Neural Network

For the training, adequate examples must be given and on the basis of these examples, the network is trained. One training example consists of the following components:

- Learning data
  The three loadcases given in Figure 4.5 are used with only one strain component not equal to 0 at a time. For each loadcase (given ε_{ij}), the corresponding stress is calculated using equation (6.1). The resulting 9 values (3 loadcases × 3 stress components) for the stress form one set of learning data.
- Learning targets
  The learning targets consist of the 6 Q_{ijkl} which had to be chosen in equation (6.1) to generate the learning data. The Q_{ijkl} are chosen somewhat arbitrarily, however, it is meaningful to systematically cover a certain admissible range.

The choice of training examples is very important. For example, if the sought values for Q_{ijkl} lie outside the range of the training examples, the Neural Network can not be trained properly and will deliver poor results. In the present application, the choice of training examples is difficult since à priori, no prediction can be made whether a component Q_{ijkl} has the value 1 or 10^6.

Training: calculations with equation (6.1)

$$\left.\begin{array}{ccc} \text{learning data} & & \text{targets} \\ \left.\begin{array}{ccc} \boxed{\begin{array}{ll} \sigma_{11}, \sigma_{22}, \sigma_{12} & (\text{LF } 1) \\ \sigma_{11}, \sigma_{22}, \sigma_{12} & (\text{LF } 2) \\ \sigma_{11}, \sigma_{22}, \sigma_{12} & (\text{LF } 3) \end{array}} & \longleftrightarrow & \boxed{\begin{array}{ll} Q_{1111} & Q_{2222} \\ Q_{1122} & Q_{1112} \\ Q_{2212} & Q_{1212} \end{array}} \end{array}\right\} \begin{array}{l}\text{1 set of}\\ \text{learning}\\ \text{data}\end{array} \\ \vdots & & \vdots \end{array}\right\} \begin{array}{l} n^6 \quad \text{sets} \\ \text{of} \\ \text{learning} \\ \text{data} \end{array}$$

Figure 6.3: Training data of Neural Network

Figure 6.3 shows the data for the training of the Neural Network. Another problem is the fact that chosen values for Q_{ijkl} have to be combined among each other. If n different values for one component are chosen, all combinations for the other 5 components must be made. Thus, the whole training set consists of n^6 examples, so the training becomes very extensive.

For the present application, the following parameters for the training of the Neural Network have proved to deliver good results:

- A backpropagation network is used with one hidden layer.
- In the training phase, 3 different values for the components Q_{ijkl} are used. With 6 independent Q_{ijkl}, there are a total of $3^6 = 729$ combinations.
- As transfer functions, linear functions are used.

The backpropagation method is used to determine the weights of the neurons. In Figure 6.4, three typical training runs are shown. For the initial weights, random numbers were chosen, so the training was different in the three runs.

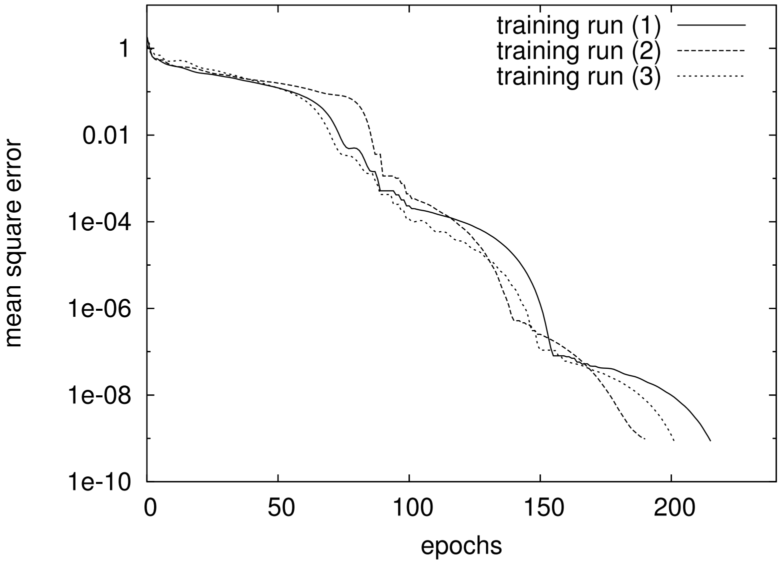

Figure 6.4: Training of Neural Network

Application of Neural Network

After the training of the Neural Network, it is applied to the parameter identification. The unit cells are subjected to the three independent load cases shown in Figure 4.5. The resulting 9 stress values are the input data for the Neural Network. The output of the Neural Network, of course, consists of the 6 unknown Q_{ijkl} (see Figure 6.5). The sought material parameters were found, see Table 6.1. The deviation from the exact solution is given in Table 6.2.

Simplex Algorithm

The Simplex Algorithm uses an optimization function $f(\mathbf{x})$ with n independent variables $(\mathbf{x} = x_1, x_2, ... x_n)$. Equation (6.2) is used here for the homogenization. The six independent

Application of Neural Network: Calculation on Unit Cell

input data		sought parameters	
$\sigma_{11}, \sigma_{22}, \sigma_{12}$ (lc 1) $\sigma_{11}, \sigma_{22}, \sigma_{12}$ (lc 2) $\sigma_{11}, \sigma_{22}, \sigma_{12}$ (lc 3)	$\longleftrightarrow$	$Q_{1111} = ?$ $Q_{2222} = ?$ $Q_{1122} = ?$ $Q_{1112} = ?$ $Q_{2212} = ?$ $Q_{1212} = ?$	$\}$ 1 set of data

Figure 6.5: Data for application of Neural Network

Q_{ijkl} are the sought variables of the optimization function. The function *nag_opt_simplex* (e04ccc) of the NAG-library [50] was used for the implementation. The following parameters were used:

- Random values are used as starting points
- The optimization stops if $f < 10^{-5}$ or a maximum of 10000 iterations is reached
- Formulation as *unconstrained problem*, i.e., no constraints for values of Q_{ijkl} are made

Figure 6.6 shows typical optimization runs. The mean square error is plotted versus the number of iterations. A comparatively large number of iterations is needed until an acceptable value for the mean square error is reached. However, one iteration step only needs

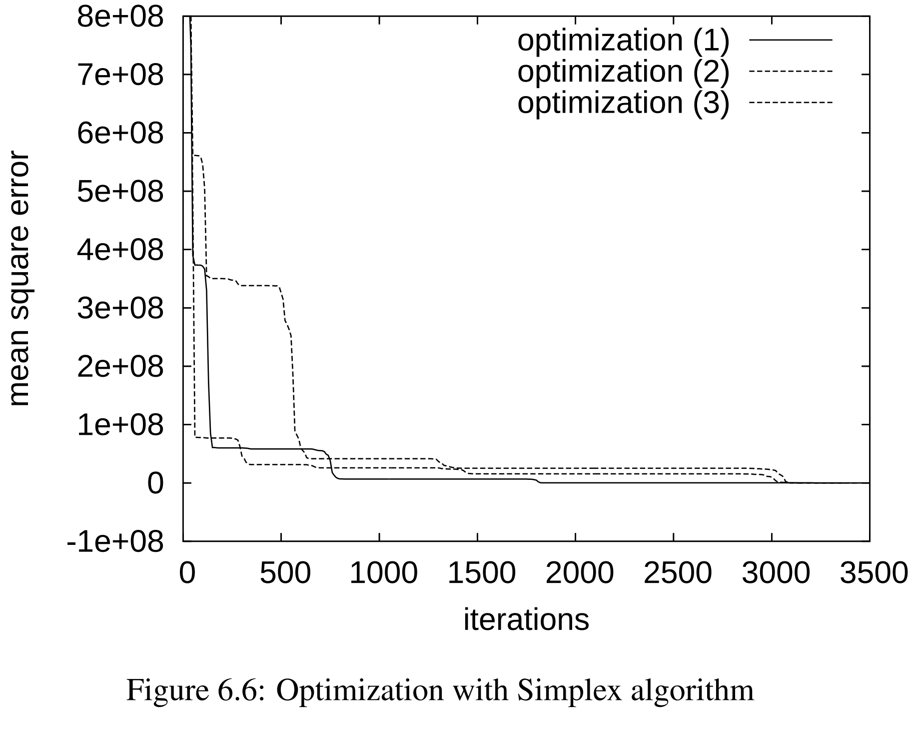

Figure 6.6: Optimization with Simplex algorithm

a little computing time. The sought material parameters were found with the Simplex Algorithm, see Table 6.1.

SQP: Sequential Quadratic Programming

Analogously to the Simplex Algorithm, equation (6.2) is used as optimization function for the Sequential Quadratic Programming method. The method does not only need the optimization function itself, but also the first derivatives of it. Equation (6.2) can be differentiated with respect to the 6 Q_{ijkl}, so no numerical procedures like Finite Differences have to be used. The function *nag_opt_nlin_sqp* (e04unc) of the NAG-library was used for the implementation. The following parameters were used:

- Random values are used as starting points
- The optimization stops if $f < 10^{-5}$ or a maximum of 10000 iterations is reached
- Formulation as *unconstrained problem*, i.e., no constraints for values of Q_{ijkl} are made

Figure 6.7 shows typical optimization runs. The mean square error is plotted versus the number of iterations. Since the derivatives of the optimization function (6.2) are used, the SQP method only needs very few iteration steps until the postulated value for the

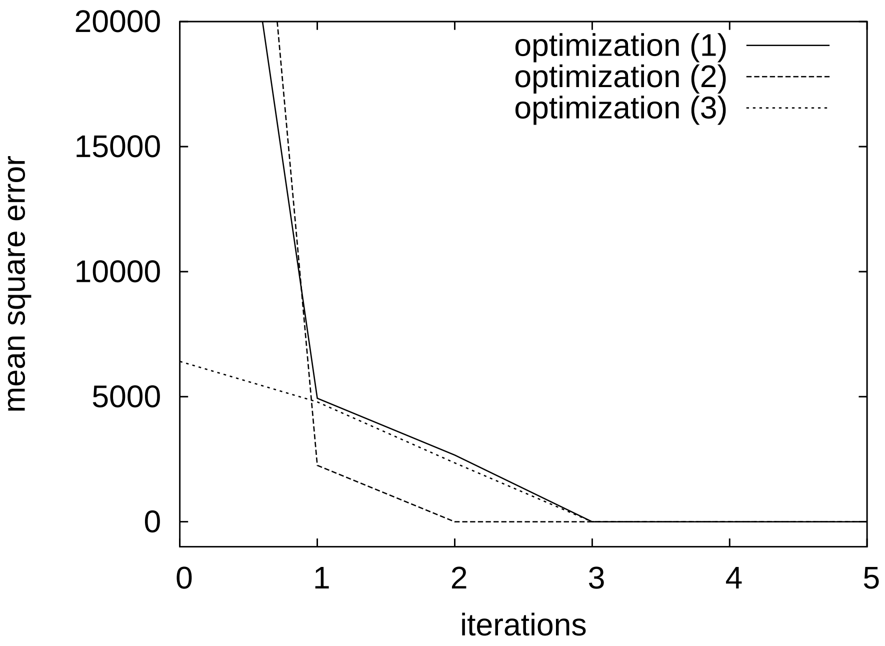

Figure 6.7: Optimization with SQP method

mean square error is reached. The sought material parameters were found with the SQP algorithm, see Table 6.1.

Discussion of results

The calculation of effective parameters of the 3 given microstructures was successfully accomplished by all optimization procedures. The calculated parameters are given in Table 6.1. The correctness of the found Q_{ijkl} were verified using equation (6.1). Due to the

microstructure (1)

	Gen. Alg.	Neur. Net	Simplex	SQP
Q_{1111}	$8.3307\cdot 10^{2}$	$8.3307\cdot 10^{2}$	$8.3307\cdot 10^{2}$	$8.3307\cdot 10^{2}$
Q_{1122}	$4.9789\cdot 10^{2}$	$4.9789\cdot 10^{2}$	$4.9789\cdot 10^{2}$	$4.9789\cdot 10^{2}$
Q_{1112}	$1.6636\cdot 10^{-7}$	$-4.0000\cdot 10^{-10}$	$-4.9000\cdot 10^{-10}$	$-2.2205\cdot 10^{-19}$
Q_{2222}	$8.3307\cdot 10^{2}$	$8.3307\cdot 10^{2}$	$8.3307\cdot 10^{2}$	$8.3307\cdot 10^{2}$
Q_{2212}	$1.0595\cdot 10^{-7}$	$-1.0720\cdot 10^{-7}$	$-1.3000\cdot 10^{-10}$	$-4.4409\cdot 10^{-19}$
Q_{1212}	$3.0141\cdot 10^{-3}$	$3.0150\cdot 10^{-3}$	$3.0150\cdot 10^{-3}$	$3.0150\cdot 10^{-3}$

microstructure (2)

	Gen. Alg.	Neur. Net	Simplex	SQP
Q_{1111}	$4.1349\cdot 10^{2}$	$4.1349\cdot 10^{2}$	$4.1349\cdot 10^{2}$	$4.1349\cdot 10^{2}$
Q_{1122}	$-3.2750\cdot 10^{-1}$	$-3.2750\cdot 10^{-1}$	$-3.2750\cdot 10^{-1}$	$-3.2750\cdot 10^{-1}$
Q_{1112}	$-5.6623\cdot 10^{-8}$	$2.2500\cdot 10^{-8}$	$-1.0000\cdot 10^{-11}$	$-4.4409\cdot 10^{-19}$
Q_{2222}	$4.1349\cdot 10^{2}$	$4.1349\cdot 10^{2}$	$4.1349\cdot 10^{2}$	$4.1349\cdot 10^{2}$
Q_{2212}	$-5.0256\cdot 10^{-8}$	$-1.2300\cdot 10^{-8}$	$-2.1000\cdot 10^{-10}$	$8.8818\cdot 10^{-19}$
Q_{1212}	$1.5120\cdot 10^{-3}$	$1.5119\cdot 10^{-3}$	$1.5119\cdot 10^{-3}$	$1.5119\cdot 10^{-3}$

microstructure (3)

	Gen. Alg.	Neur. Net	Simplex	SQP
Q_{1111}	$2.1149\cdot 10^{2}$	$2.1149\cdot 10^{2}$	$2.1149\cdot 10^{2}$	$2.1149\cdot 10^{2}$
Q_{1122}	$-8.1308\cdot 10^{1}$	$-8.1308\cdot 10^{1}$	$-8.1308\cdot 10^{1}$	$-8.1308\cdot 10^{1}$
Q_{1112}	$3.9604\cdot 10^{-8}$	$-5.0000\cdot 10^{-10}$	$8.0000\cdot 10^{-11}$	$-5.4210\cdot 10^{-23}$
Q_{2222}	$2.1149\cdot 10^{2}$	$2.1149\cdot 10^{2}$	$2.1149\cdot 10^{2}$	$2.1149\cdot 10^{2}$
Q_{2212}	$2.1499\cdot 10^{-8}$	$1.0000\cdot 10^{-9}$	$-2.4000\cdot 10^{-10}$	$4.3368\cdot 10^{-22}$
Q_{1212}	$1.5119\cdot 10^{-3}$	$1.5119\cdot 10^{-3}$	$1.5119\cdot 10^{-3}$	$1.5119\cdot 10^{-3}$

Table 6.1: Results of optimization

symmetry of the unit cells, the components Q_{1111} and Q_{2222} are always equal, i.e., the stiffness in horizontal and vertical direction is the same. Moreover, the components Q_{1112} and Q_{2212} are always 0.

microstructure (1)

	exact solution	Gen. Alg.	Neur. Net	Simplex	SQP
Q_{1111}	$8.3307 \cdot 10^{2}$	-	-	-	-
Q_{1122}	$4.9789 \cdot 10^{2}$	-	-	-	-
Q_{1112}	0	$< 10^{-6}$	$< 10^{-9}$	$< 10^{-9}$	$< 10^{-18}$
Q_{2222}	$8.3307 \cdot 10^{2}$	-	-	-	-
Q_{2212}	0	$< 10^{-6}$	$< 10^{-6}$	$< 10^{-9}$	$< 10^{-18}$
Q_{1212}	$3.0150 \cdot 10^{-3}$	$< 10^{-6}$	-	-	-

microstructure (2)

	exact solution	Gen. Alg.	Neur. Net	Simplex	SQP
Q_{1111}	$4.1349 \cdot 10^{2}$	-	-	-	-
Q_{1122}	$-3.2750 \cdot 10^{-1}$	-	-	-	-
Q_{1112}	0	$< 10^{-7}$	$< 10^{-7}$	$< 10^{-10}$	$< 10^{-18}$
Q_{2222}	$4.1349 \cdot 10^{2}$	-	-	-	-
Q_{2212}	0	$< 10^{-7}$	$< 10^{-7}$	$< 10^{-9}$	$< 10^{-18}$
Q_{1212}	$1.5119 \cdot 10^{-3}$	$< 10^{-6}$	-	-	-

microstructure (3)

	exact solution	Gen. Alg.	Neur. Net	Simplex	SQP
Q_{1111}	$2.1149 \cdot 10^{2}$	-	-	-	-
Q_{1122}	$-8.1308 \cdot 10^{1}$	-	-	-	-
Q_{1112}	0	$< 10^{-7}$	$< 10^{-9}$	$< 10^{-10}$	$< 10^{-22}$
Q_{2222}	$2.1149 \cdot 10^{2}$	-	-	-	-
Q_{2212}	0	$< 10^{-7}$	$< 10^{-8}$	$< 10^{-9}$	$< 10^{-21}$
Q_{1212}	$1.5119 \cdot 10^{-3}$	-	-	-	-

Table 6.2: Results of optimization: deviation from exact solution

As expected, all optimization procedures have determined the sought material parameters correctly. Since numerical procedures were used, the solutions are only correct to a certain precision. Therefore, the components Q_{1112} and Q_{2212} are not *exactly* 0.

The numerical cost to obtain a solution was quite different. The Simplex method, which is the least complicated of all procedures, needed a large number of (quick) iterations. In comparison to that, the SQP method was much faster, which is logical because the first derivatives of the optimization function is used by the method. Thus, more information about the problem is given to the algorithm, resulting in a significant improvement in performance. The Genetic Algorithm also delivered good results, although it was not as quick as the SQP method.

The Neural Network was, compared to the first three procedures, rather difficult to use for the given problem. Firstly, the training of the Network is numerically very expensive. Secondly, it is hard to find suitable training examples. The number of training examples increases rapidly the more values for the single components Q_{ijkl} are used because all combinations of the components have to be made. However, once the training is complete the Neural Network delivers good, quick results. It depends on the intended application whether the use of a Neural Network is meaningful: If the computation of parameters needs to be done for a lot of different microstructures, it makes sense to train a Neural Network once and then apply it many times. On the other hand, if only a single computation of material parameters is needed, the other optimization procedures are definitely more suitable.

6.2 Plane stress microstructure

The calculation of effective static properties is now done for a plate in plane stress. The microstructure given in Figure 6.8 is considered. The calculation of the plate is done with

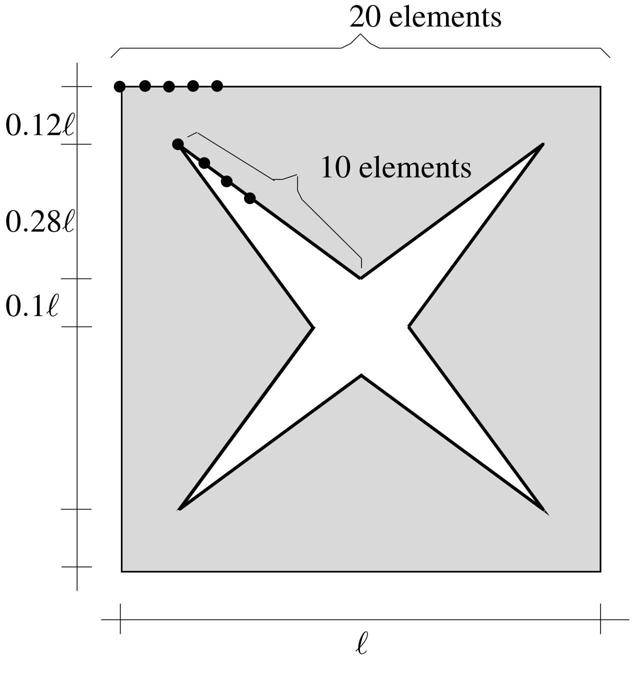

Figure 6.8: Microstructure for numerical study

the Boudary Element Method, a discretization of 20 elements on the outer edges and 10 elements on one part of the inner edge according to Figure 6.8 is used. The material of the plate is steel with a Young's modulus of $E = 2.1 \times 10^{11}\mathrm{N/m}^2$ and a Poisson's ratio of 0.3. The plate is loaded with a prescribed displacement of 0.05ℓ on the left and right hand side, while the upper and lower edges can deform freely, see Figure 6.9. These homogeneous boundary conditions do not fulfill the periodicity conditions, because neighbouring cells do not undergo the same deformation pattern. This is neglected, however, because both the deformation and the tractions on the cell edges are averaged. Thus, after the averaging process, periodicity is fulfilled. The averaging is pictured in Figure 6.10. With this, analogously to the beam-type microstructures, a set of averaged stresses and strains is obtained. In the present case, only the stress σ_{11}^{micro} and the strains ε_{11}^{micro} and ε_{22}^{micro} are not equal to 0

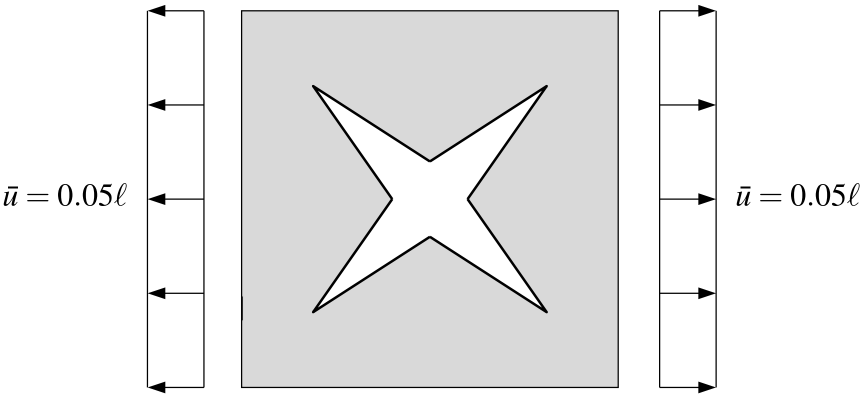

Figure 6.9: Loadcase of microstructure

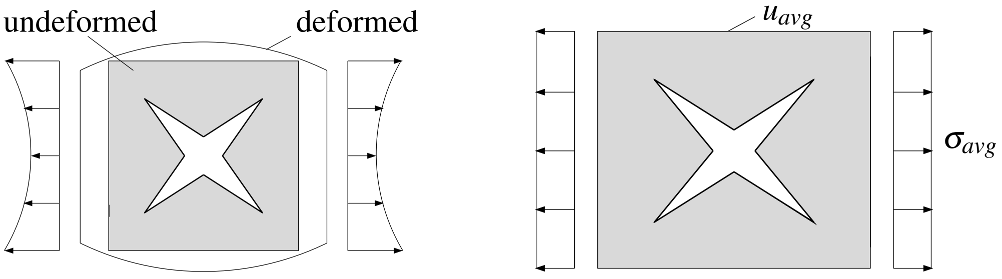

Figure 6.10: Averaging of deformation and tractions

$$\sigma_{11}^{micro} \neq 0, \quad \varepsilon_{11}^{micro} \neq 0, \quad \varepsilon_{11}^{micro} \neq 0 \tag{6.4}$$

$$\sigma_{22}^{micro} = 0, \quad \sigma_{12}^{micro} = 0, \quad \varepsilon_{12}^{micro} = 0 \quad . \tag{6.5}$$

These stresses and strains are the input data for the optimization process, where effective properties are calculated. On the macroscopic scale, the constitutive equation

$$\sigma_{ij}^{macro} = \frac{E}{(1+\nu)}\,\varepsilon_{ij}^{macro} + \frac{\nu E}{(1+\nu)(1-2\nu)}\,\delta_{ij}\,\varepsilon_{kk}^{macro} \tag{6.6}$$

is applied. Analogously to the beam-type microstructures, an optimization process is applied to obtain adequate material parameters on the macroscopic scale. From the results of the beam-type microstructures, it can be stated that the Genetic Algorithm delivers the most reliable results, so it is applied as optimization procedure. The target function for the optimization is identical to the one used for the beam-type cells, however, here only one loadcase is used so equation (6.2) simplifies

$$f = \left(\sigma_{11}^{micro} - \sigma_{11}^{macro}\right)^2 + \left(\sigma_{22}^{micro} - \sigma_{22}^{macro}\right)^2 + \left(\sigma_{12}^{micro} - \sigma_{12}^{macro}\right)^2 . \qquad (6.7)$$

The stresses σ_{ij}^{micro} are constant input data with respect to the optimization procedure, whereas σ_{ij}^{macro} are repeatedly calculated during the optimzation process via equation (6.7).

A Genetic Algorithm is used to solve the optimization problem. The fitness function (6.7) has the 2 paramters E and ν as unknown values, so each individual consists of 2 chromosomes. The following settings were used for the Genetic Algorithm:

- A population size of 100 individuals is chosen
- The starting population is created randomly
- New individuals are created via 1-point-crossover
- The mutation of an individual is done accordingly to the standardized normal distribution
- 50 individuals are created newly in one generation, the remaining 50 are created as offspring of the previous generation
- The optimization is stopped after a maximum of 1000 iterations or if the best fitness value is smaller than 10^{-5}

The parameters were determined in a trial-and-error process and have shown to deliver good results.

Figure 6.11 shows the performance of the Genetic Algorithm. The fitness value of the best individual of a generation is plotted versus the number of generations. Since the starting population is generated randomly, three optimization runs were done.

All three optimization runs were successful. A Youngs's modulus of $7.50 \times 10^{10} \mathrm{N/m^2}$ and a Poisson's ratio of -0.143 was calculated. This result was verified using the constitutive equation (6.6) and the averaged stresses and strains on the microscale.

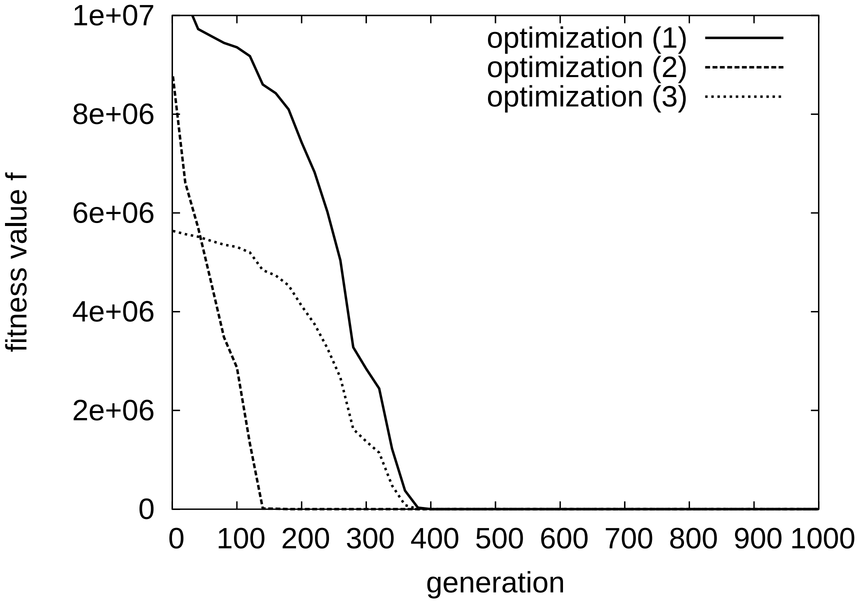

Figure 6.11: Performance of Genetic Algorithm

7 EFFECTIVE PROPERTIES IN DYNAMICS

In this chapter, the prescribed homogenization strategy is realized in the dynamic case, i.e., the microstructure is calculated in frequency domain with a harmonic excitation. Due to inertia, the response of the unit cell is frequency dependent: if a harmonic stress is given, the strain is frequency dependent and vice-versa. The frequency dependence is also given on the macroscopic scale, thus, a frequency dependent macroscopic constitutive equation is required. Here, a viscoelastic constitutive equation is chosen on the macroscale.

In statics, it has been shown that the homogenization problem can be solved analytically. The stress and strain can be calculated and the constitutive equation can be solved for the unknown material parameters. The same can be done in frequency domain as well, but only if one specific frequency ω is considered at a time. It is possible to calculate stress and strain for an excitation frequency ω and obtain material parameters for this frequency. This can be done repeatedly, so material parameters for a number of frequencies can be computed. However, it is desirable to not only have material parameters for a specific frequency but for a whole frequency range. Thus, the aim is to obtain parameters of a consitutive equation like

$$\sigma(\omega) = \frac{\sum\limits_{k=0}^{N} q_k (i\omega)^k}{\sum\limits_{k=0}^{N} p_k (i\omega)^k} \varepsilon(\omega) \quad , \tag{7.1}$$

see also equation (2.57). p_k and q_k are parameters which cover a large frequency range. To obtain adequate values for these parameters, it is necessary to calculate the stress $\sigma^{micro}(\omega)$ and strain $\varepsilon^{micro}(\omega)$ on the microscale for a number of frequencies, covering a specific range. Either the stress is given and the strain is calculated or vice-versa. In the macroscopic constitutive equation, e.g., equation (7.1) the parameters p_k and q_k have to be found to correspond to the microscale results. For example, if a microscopic strain $\varepsilon^{micro}(\omega)$ is prescribed, the frequency response $\sigma^{micro}(\omega)$ must correspond to a macroscopic stress $\sigma^{macro}(\omega)$, where $\sigma^{macro}(\omega)$ is a function of the material parameters p_k and q_k, i.e.,

$$\sigma^{micro}(\omega) \overset{!}{=} \sigma^{macro}(\omega, p_k, q_k) \quad . \tag{7.2}$$

To satisfy equation (7.2), the mean square error between stress on the micro- and macroscale is taken and the difference is minimized

$$\left(\sigma^{micro}(\omega) - \sigma^{macro}(\omega, p_k, q_k)\right)^2 \to 0 \quad . \tag{7.3}$$

At this point, an optimization procedure is required. The parameters of the constitutive equation must be chosen such that the difference between micro- and macroscale are as small as possible. Since the stress on the microscale can only be calculated for discrete frequencies the mean square error of equation (7.3) is summed up over a number of discrete frequency steps

$$f = \sum_{\omega_{start}}^{\omega_{end}} \left(\sigma^{micro}(\omega) - \sigma^{macro}(\omega, p_k, q_k)\right)^2 \to 0 \quad . \tag{7.4}$$

If a microscopic stress is given, the stress must be replaced by the strain in equations (7.3) and (7.4).

From the results in the static case, it can be stated that the Neural Network is not suitable to solve the optimization problem. The reason is that in the training phase, training examples must be chosen with specific values for the sought material parameters. In order to cover a range for p_k and q_k, a very large number of training examples would be necessary. Thus, only the gradient-based optimization procedures and the Genetic Algorithm are used for the optimization.

The chapter consists of 3 parts. Firstly, effective properties are calculated within a small frequency range, i.e., from the static case ($\omega \to 0$) up to the first eigenfrequency. Secondly, a broader frequency range is covered. For both frequency ranges, beam-type microstructures are analyzed. In the last section, a plate in plane stress state is investigated.

7.1 Beam cells in small frequency range

The microstructure shown in Figure 7.1 is used for the following considerations. The cell is analzed in frequency domain. A harmonic strain in one direction is applied to the cell (see also Figure 7.1). The procedure presented in chapter 2 is used for the calculation because it delivers exact results.

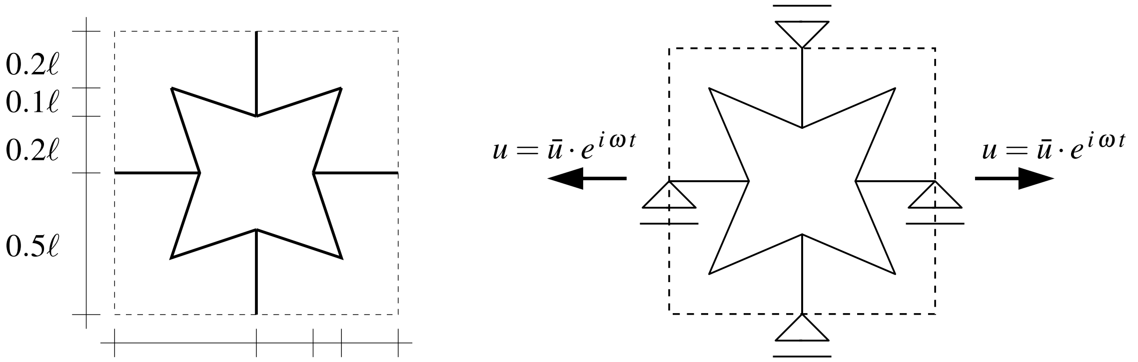

Figure 7.1: Geometry and load case of the unit cell

Since the considered microstructure is assumed to be periodic, the opposing nodes of the cell must have the same deformation and the forces of the node pairs must be equal in magnitude but opposite in direction. Due to the symmetry of the cell periodicity is fulfilled, e.g., the reaction force of the node on the left hand side corresponds to the applied load on the right hand side.

The cell consists of beams with a quadratic cross section of $0.1 \cdot \ell \times 0.1 \cdot \ell$. The microstructure material is steel with a Young's modulus of $E = 2.1 \cdot 10^{11}\mathrm{N/m^2}$. The frequency response for an applied displacement amplitude of $\bar{u} = 0.001\ell$ is calculated on a logarithmic scale up to a frequency of 18 kHz.

On the macroscale, the one-dimensional constitutive equation

$$\sigma(\omega) = G(i\omega)\,\varepsilon(\omega) = \frac{\sum\limits_{k=1}^{N} q_k (i\omega)^k}{\sum\limits_{k=1}^{M} p_k (i\omega)^k}\,\varepsilon(\omega) \tag{7.5}$$

is used (see also equation (2.55)). Equation (7.5) has to be fulfilled for a frequency range $0..\omega_{max}$. Contrary to the static (1-D) case, a larger number of parameters have to be determined. The number of parameters is somewhat arbitrary, it depends on the considered frequency range how many parameters have to be used. For the present case, it has turned out that a total $M+N = 14$ parameters are sufficient to deliver good results for the considered frequency range.

For the formulation of the homogenization problem as an optimization problem, the mean square error technique is used. The square difference of the stress on micro- and macroscale must be 0 for the optimal parameters on the macroscale

$$f = \sum_{\omega=0}^{\omega_{max}} \left(\sigma^{micro}(\omega) - \sigma^{macro}(\omega, p_k, q_k)\right)^2 \to 0 \quad . \tag{7.6}$$

7.1.1 Genetic Algorithm

The fitness value of the individuals quality is calculated via equation (7.6). A total number of $M+N = 14$ parameters is used, so each individual consists of 14 chromosomes. In a trial and error process, the following parameters of the Genetic Algorithm have shown to be suitable for the present application:

- A population size of 1000 individuals is chosen
- The starting population is created randomly
- New individuals are created via 2-point-crossover
- The mutation of an individual is done accordingly to the standardized normal distribution
- 250 individuals are created newly in one generation, the remaining 750 are created as offspring of the previous generation

- The optimization is stopped after a maximum of 50000 iterations or if the best fitness value $f < 10^{-5}$.

The proceeding of the optimization is shown in Figure 7.2. Since the first generation is created randomly and also during the optimization, genetic operators are applied randomly, the proceeding of the optimization is different in all the optimization runs. The fitness value of the best individual is plotted versus the number of generations. It can be seen that in all three cases, a relatively small fitness values was obtained, however, after a different number of generations. The obtained values for p_k and q_k are given in Table 7.1. Contrary to the static case, there is more than one set of parameters which describes the behavior accurately. Figure 7.3 shows the behavior on the micro- and macroscale. The modulus $G(\omega)$ is plotted versus the frequency. On the microscale (solid line), $G(\omega)$ is

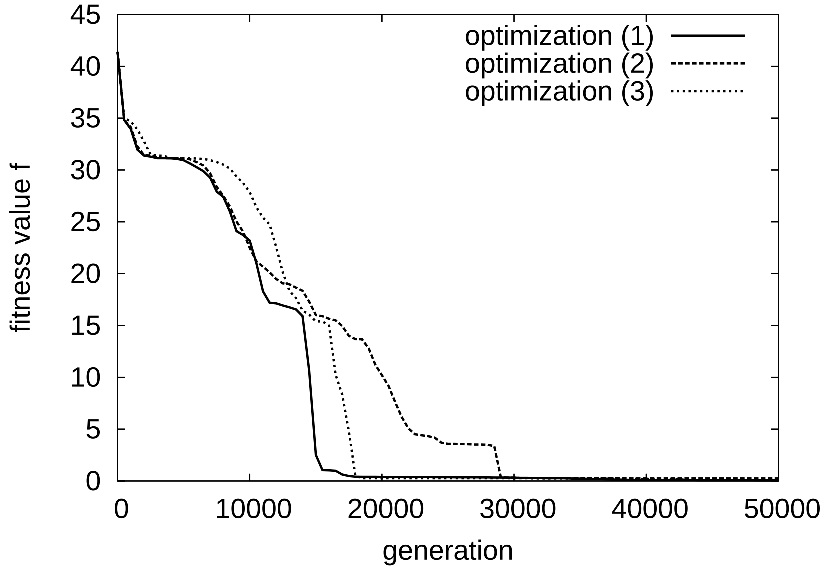

Figure 7.2: Optimization with Genetic Algorithm

$$G(\omega) = \frac{\sigma^{micro}}{\varepsilon^{micro}} \tag{7.7}$$

with the stress and strain $\sigma^{micro}, \varepsilon^{micro}$ of the unit cell, whereas for the three macroscale results, equation (7.5) was solved for $\varepsilon(\omega)$ and plotted for the three optimization runs with the respective parameters p_k and q_k given in Table 7.1.

7.1.2 Simplex Algorithm

The Simplex Algorithm is used to determine the macroscale parameters. The optimization function (7.5) with the 14 parameters is minimized. Like in the static case, the function *nag_opt_simplex* (e04ccc) of the NAG-library was used with the following settings:

optimization (1) $f = 0.02996$

k	q_k	p_k
1	$1.7617 \cdot 10^{1}$	$1.5469 \cdot 10^{7}$
2	$2.2672 \cdot 10^{2}$	$1.8152 \cdot 10^{8}$
3	$-1.7471 \cdot 10^{-14}$	$1.2785 \cdot 10^{5}$
4	$1.8300 \cdot 10^{0}$	$1.4790 \cdot 10^{6}$
5	$3.3705 \cdot 10^{-3}$	$1.0693 \cdot 10^{4}$
6	$4.2695 \cdot 10^{-3}$	$3.0166 \cdot 10^{3}$
7	$1.7815 \cdot 10^{-19}$	$4.0734 \cdot 10^{1}$

optimization (2) $f = 0.08141$

k	q_k	p_k
1	$4.9398 \cdot 10^{0}$	$4.1763 \cdot 10^{6}$
2	$4.0007 \cdot 10^{2}$	$3.8899 \cdot 10^{8}$
3	$-1.6224 \cdot 10^{-14}$	$4.3765 \cdot 10^{5}$
4	$2.1568 \cdot 10^{0}$	$2.7570 \cdot 10^{6}$
5	$1.2825 \cdot 10^{-16}$	$6.7831 \cdot 10^{3}$
6	$2.9828 \cdot 10^{-3}$	$4.8445 \cdot 10^{3}$
7	$5.0153 \cdot 10^{-5}$	$2.0826 \cdot 10^{1}$

optimization (3) $f = 0.02313$

k	q_k	p_k
1	$7.6350 \cdot 10^{-5}$	$6.3904 \cdot 10^{1}$
2	$2.0017 \cdot 10^{2}$	$1.6060 \cdot 10^{8}$
3	$-7.0055 \cdot 10^{-14}$	$4.0609 \cdot 10^{5}$
4	$1.1501 \cdot 10^{0}$	$1.1117 \cdot 10^{6}$
5	$4.4045 \cdot 10^{-16}$	$5.5493 \cdot 10^{3}$
6	$1.7722 \cdot 10^{-3}$	$1.8973 \cdot 10^{3}$
7	$2.6157 \cdot 10^{-5}$	$1.5891 \cdot 10^{1}$

Table 7.1: Obtained material parameters by Genetic Algorithm

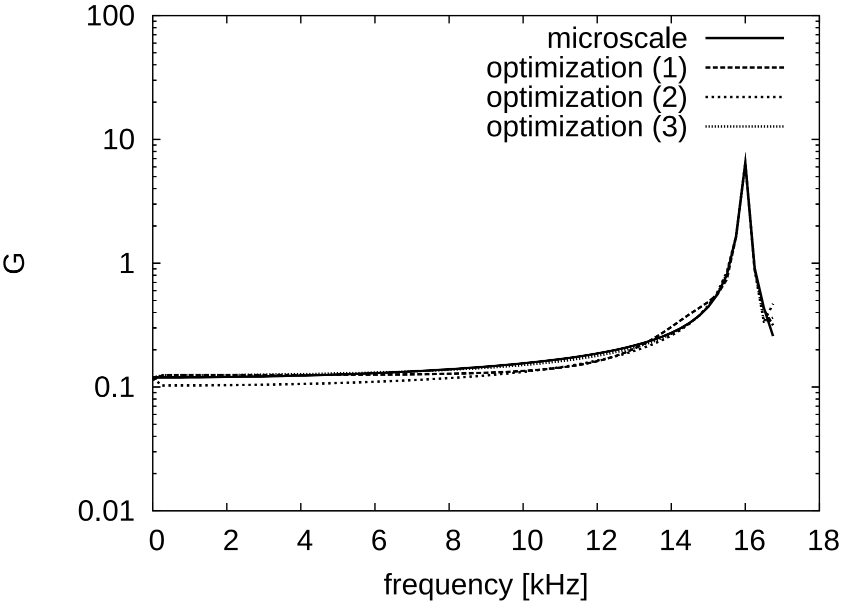

Figure 7.3: Genetic Algorithm results on the micro- and macroscale

- Random values are used as starting points
- The optimization stops if $f < 10^{-5}$ or a maximum of 10000 iterations is reached
- Formulation as *unconstrained problem*, i.e., no constraints for values of p_k and q_k are made.

The courses of three optimization runs are shown in Figure 7.4. The fitness value is plotted versus the number of iterations. As can be seen, the optimization did not end with an optimal value close to 0 in all three runs. One optimization run found a local minimum of the optimization function, which is due to a 'wrong' starting point. The calculated material parameters and final values of the optimization function are given in Table 7.2.

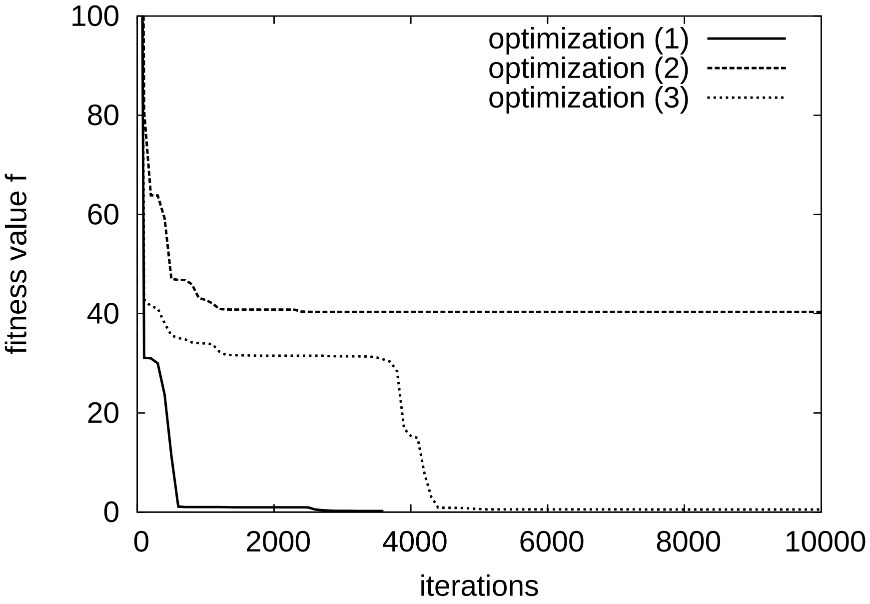

Figure 7.4: Optimization using Simplex algorithm

Analogously to the Genetic Algorithm, Figure 7.5 shows the comparison of the micro- and macroscale. For the first and third optimization run, the micro- and macroscale results fit relatively well. The calculated parameters of the second run, however, show a rather poor fit, which could have already been expected from the final value of the optimization function ($f = 40.36443$).

7.1.3 SQP - Sequential Quadratic Programming

The Sequential Quadratic Programming method is used to minimize the optimization function (7.6). The following parameters were used:

- Random values are used as starting points
- The optimization stops if $f < 10^{-5}$ or a maximum of 1000 iterations is reached

optimization (3) $f = 0.02313$

k	q_k	p_k
1	$-2.3120 \cdot 10^{-1}$	$8.7004 \cdot 10^{4}$
2	$9.9885 \cdot 10^{2}$	$9.9986 \cdot 10^{8}$
3	$-6.3275 \cdot 10^{0}$	$1.6585 \cdot 10^{6}$
4	$3.8550 \cdot 10^{0}$	$5.0101 \cdot 10^{5}$
5	$2.2212 \cdot 10^{0}$	$1.3758 \cdot 10^{6}$
6	$8.6224 \cdot 10^{-2}$	$-1.2021 \cdot 10^{4}$
7	$9.6364 \cdot 10^{-3}$	$5.3747 \cdot 10^{3}$

optimization (2) $f = 4.03644$

k	q_k	p_k
1	$4.2969 \cdot 10^{0}$	$4.6088 \cdot 10^{6}$
2	$3.7837 \cdot 10^{0}$	$-9.4540 \cdot 10^{6}$
3	$-4.3263 \cdot 10^{1}$	$-6.5015 \cdot 10^{6}$
4	$2.0501 \cdot 10^{1}$	$6.1724 \cdot 10^{6}$
5	$-5.3712 \cdot 10^{1}$	$-4.1837 \cdot 10^{6}$
6	$-1.1843 \cdot 10^{1}$	$1.6728 \cdot 10^{6}$
7	$-7.7912 \cdot 10^{0}$	$-1.8432 \cdot 10^{6}$

optimization (3) $f = 0.08141$

k	q_k	p_k
1	$-1.2788 \cdot 10^{-1}$	$-8.1114 \cdot 10^{4}$
2	$-2.4249 \cdot 10^{-1}$	$-3.2711 \cdot 10^{4}$
3	$-1.7395 \cdot 10^{-1}$	$-3.9820 \cdot 10^{4}$
4	$-4.3973 \cdot 10^{-2}$	$-2.8295 \cdot 10^{4}$
5	$-1.0598 \cdot 10^{-1}$	$-3.9454 \cdot 10^{4}$
6	$-4.0095 \cdot 10^{-2}$	$-1.1223 \cdot 10^{2}$
7	$-3.0264 \cdot 10^{-4}$	$-1.5512 \cdot 10^{2}$

Table 7.2: Obtained material parameters by Simplex Algorithm

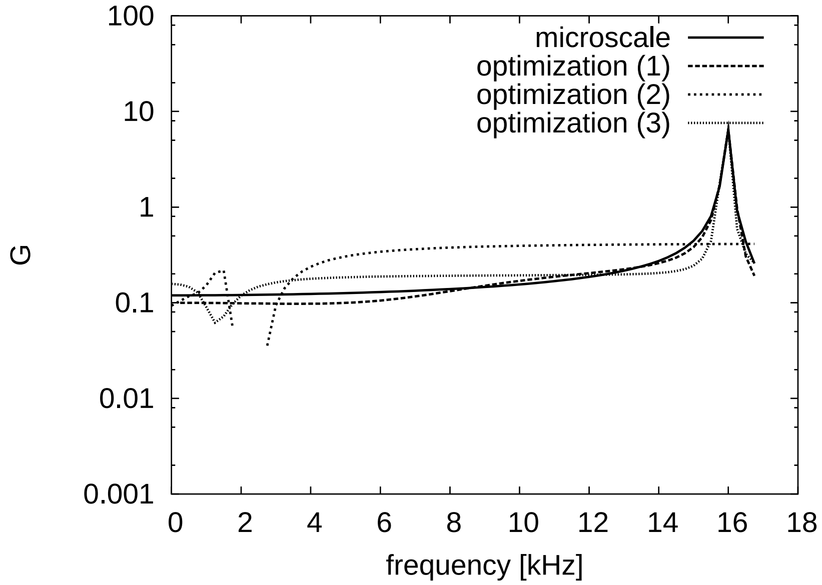

Figure 7.5: Simplex results on the micro- and macroscale

- Formulation as *unconstrained problem*, i.e., no constraints for values of p_k and q_k are made

Figure 7.6 shows typical optimization runs. The fitness value is plotted versus the number of iterations. The SQP method was able to obtain a value $f < 1$ in two runs. One optimization run was only able to find a local minimum of the function. This can be seen from the final value of the optimization of $f = 31.2730$ and also from the results for $G(\omega)$ on micro- and macroscale. See Table 7.3 for the obtained values for the parameters p_k and q_k and Figure 7.6 for results on both scales.

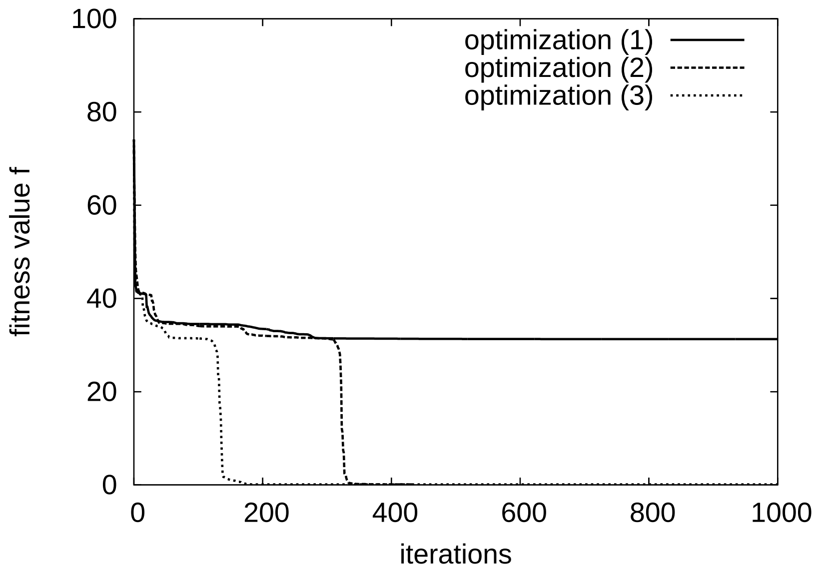

Figure 7.6: Optimization using SQP algorithm

7.1.4 Discussion of results

All three optimization procedures were able to find adequate material parameters on the macroscopic scale. It can already be seen from the fitness value or final value of the optimization function, respectively, how good the parameters fit the microscopic properties. The Simplex Algorithm and the Sequential Quadratic Programming method both have problems with local minima. If a 'wrong' starting point is used for the optimization, they may deliver poor results. The Simplex Algorithm is much slower than the SQP method, which is obvious since it does not use the first derivatives of the optimization function. The Genetic Algorithm is the most reliable of all optimization procedures. No starting point is required, and it always delivers good results. However, it takes much more computing time to obtain results.

optimization (1) $f = 31.2730$

k	q_k	p_k
1	$2.3801 \cdot 10^{3}$	$1.7790 \cdot 10^{6}$
2	$-2.1948 \cdot 10^{4}$	$2.9126 \cdot 10^{6}$
3	$-3.5378 \cdot 10^{4}$	$9.0371 \cdot 10^{4}$
4	$-2.0615 \cdot 10^{4}$	$-9.9309 \cdot 10^{5}$
5	$-6.5232 \cdot 10^{3}$	$-1.7844 \cdot 10^{2}$
6	$-9.5146 \cdot 10^{2}$	$5.9092 \cdot 10^{3}$
7	$1.1842 \cdot 10^{4}$	$1.2702 \cdot 10^{0}$

optimization (2) $f = 0.0942$

k	q_k	p_k
1	$2.7349 \cdot 10^{8}$	$2.3917 \cdot 10^{11}$
2	$-7.8132 \cdot 10^{8}$	$-2.5963 \cdot 10^{11}$
3	$3.0370 \cdot 10^{8}$	$-1.1559 \cdot 10^{11}$
4	$3.0801 \cdot 10^{8}$	$-4.0479 \cdot 10^{10}$
5	$1.2956 \cdot 10^{8}$	$7.1634 \cdot 10^{10}$
6	$-3.1951 \cdot 10^{6}$	$-2.2324 \cdot 10^{8}$
7	$4.4835 \cdot 10^{5}$	$2.8131 \cdot 10^{8}$

optimization (3) $f = 0.0961$

k	q_k	p_k
1	$-1.7145 \cdot 10^{-1}$	$-1.2534 \cdot 10^{2}$
2	$-6.7364 \cdot 10^{-1}$	$-1.0430 \cdot 10^{2}$
3	$-9.4824 \cdot 10^{-1}$	$4.1414 \cdot 10^{1}$
4	$1.6859 \cdot 10^{0}$	$1.8603 \cdot 10^{1}$
5	$-1.8562 \cdot 10^{-1}$	$-1.0769 \cdot 10^{2}$
6	$2.6000 \cdot 10^{-5}$	$-2.8079 \cdot 10^{-2}$
7	$-6.5400 \cdot 10^{-4}$	$-4.2114 \cdot 10^{-1}$

Table 7.3: Obtained material parameters by SQP

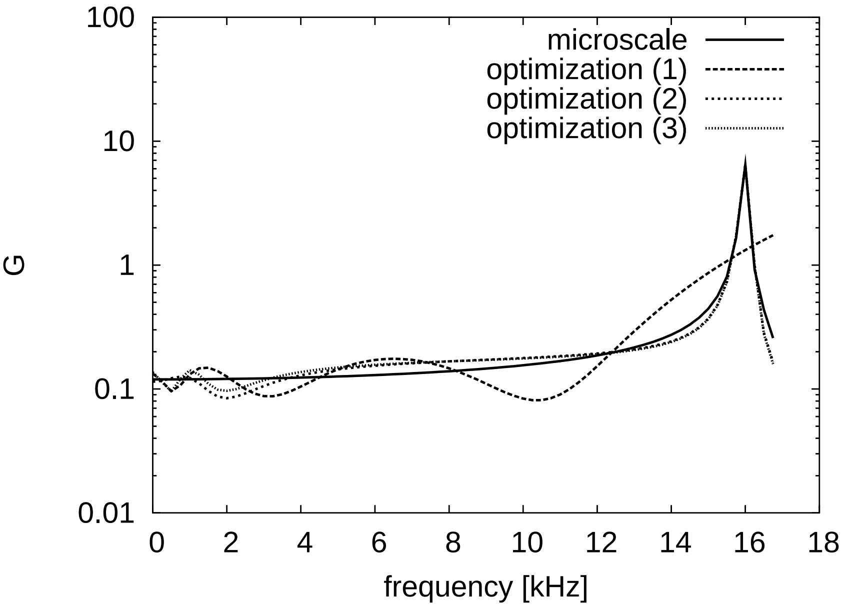

Figure 7.7: SQP results on the micro- and macroscale

7.2 Beam cells in large frequency range

Effective properties for a broader frequency range are determined for both auxetic and non-auxetic microstructures in this chapter. The following two microstructures given in Figure 7.8 are used for the numerical study. Both cells consist of beams with a quadratic cross section of $0.1\ell \times 0.1\ell$. The microstructure material is PMMA with a slight damping (see Appendix D). A frequency range from 0 up to 3×10^3 kHz is chosen. Due to the existence of higher eigenmodes for more than one unit cell (see section 4.2.5), the microstructures are calculated multiple times. Calculations were done for 1, 2×2, ...$n \times n$ unit cells up to $n = 5$ and the results were averaged. The loadcase for both cells is given in Figure 7.9. Again, a displacement amplitude is applied on the left and right hand side of the cell.

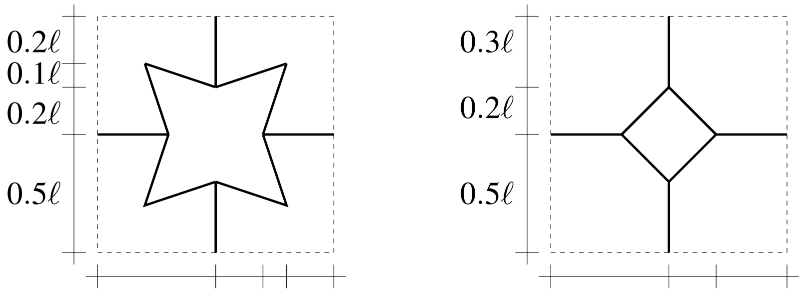

Figure 7.8: Auxetic and non-auxetic microstructures

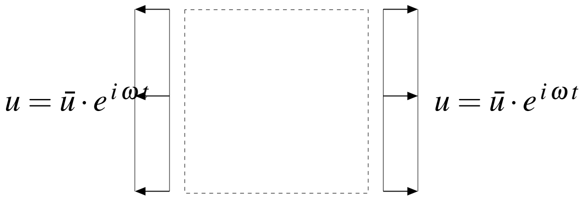

Figure 7.9: Loadcase

On the macroscale, the constitutive equation

$$\sigma_{ij}(\omega) = \frac{E(\omega)}{(1+\nu(\omega))} \varepsilon_{ij}(\omega) + \frac{\nu(\omega)E(\omega)}{(1+\nu(\omega))(1-2\nu(\omega))} \delta_{ij} \varepsilon_{kk}(\omega) \tag{7.8}$$

is applied. For Young's modulus, the viscoelastic model

$$E(\omega) = \bar{E} \frac{1+q_1(i\omega)^{\alpha_1}+q_2(i\omega)^{\alpha_2}}{1+p_1(i\omega)^{\alpha_1}+p_2(i\omega)^{\alpha_2}} \quad . \tag{7.9}$$

with fractional derivatives and 7 parameters is used. The same model but with possible different parameters is used for Poisson's ratio

$$\nu(\omega) = \bar{\nu} \frac{1+\tilde{q}_1(i\omega)^{\tilde{\alpha}_1}+\tilde{q}_2(i\omega)^{\tilde{\alpha}_2}}{1+\tilde{p}_1(i\omega)^{\tilde{\alpha}_1}+\tilde{p}_2(i\omega)^{\tilde{\alpha}_2}} \quad . \tag{7.10}$$

Again, the choice of these models is somewhat arbitrary. For the considered frequency range, they have shown to be sufficient. A number of trials with fewer parameters were not successful, as well as models with more parameters, yet without fractional derivatives.

From the results of the previous chapter, it can be stated that the Genetic Algorithm is the most reliable optimization procedure to obtain the sought material parameter. The gradient-based optimization techniques were quicker, however, the results are not reliable. Thus, a Genetic Algorithm is applied here. The following parameters were used to determine the material parameters:

- A population size of 1000 individuals is chosen
- The starting population is created randomly
- New individuals are created via 2-point-crossover
- The mutation of an individual is done accordingly to the standardized normal distribution, mutation probability is 10%
- 150 individuals are created newly in one generation, the remaining 850 are created as offspring of the previous generation
- The optimization is stopped after a maximum of 50000 iterations or if the best fitness value $f < 10^{-5}$.

The results of the optimization are depicted in the following Figures. Figures 7.10 and 7.11 show the Young's modulus and Poisson's ratio for the auxetic microstructure, while in Figures 7.12 and 7.13, Young's modulus and Poisson's ratio for the non-auxetic microstructure are shown. In each diagram, the microscopic and macroscopic results are plotted versus the frequency.

As can be seen, the optimization was not able to fit each single eigenfrequency of the microstructure results. However, the general tendency is preserved. In all four result plots, it can be seen that for small frequencies, the fitted parameters converge into the static solution. The obtained material parameters for ν and E are given in Table 7.4 for the auxetic microstructure and in Table 7.5 for the non-auxetic material.

The slightly viscoelastic material on the microscopic scale had virtually no effect on the homogenization process. There were still eigenfrequencies on the microscale which cause that the search of the material parameters is very difficult.

For the optimization, it can be observed that there is no difference whether an auxetic or non-auxetic microstructure is used as input data. This could have been expected à priori, because the same mathematical problem (with slightly different parameters) needs to be solved by the optimization procedure.

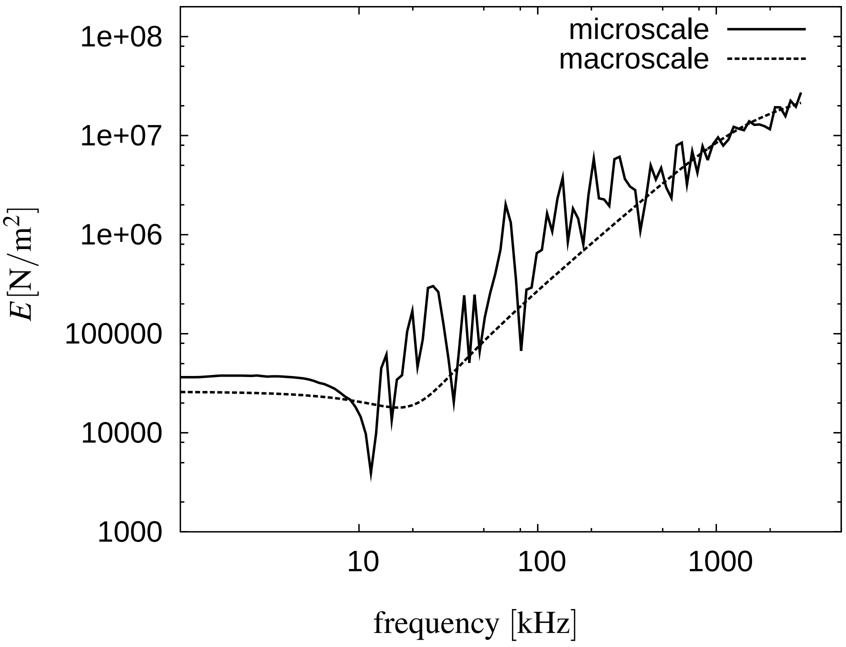

Figure 7.10: Young’s modulus for auxetic microstructure

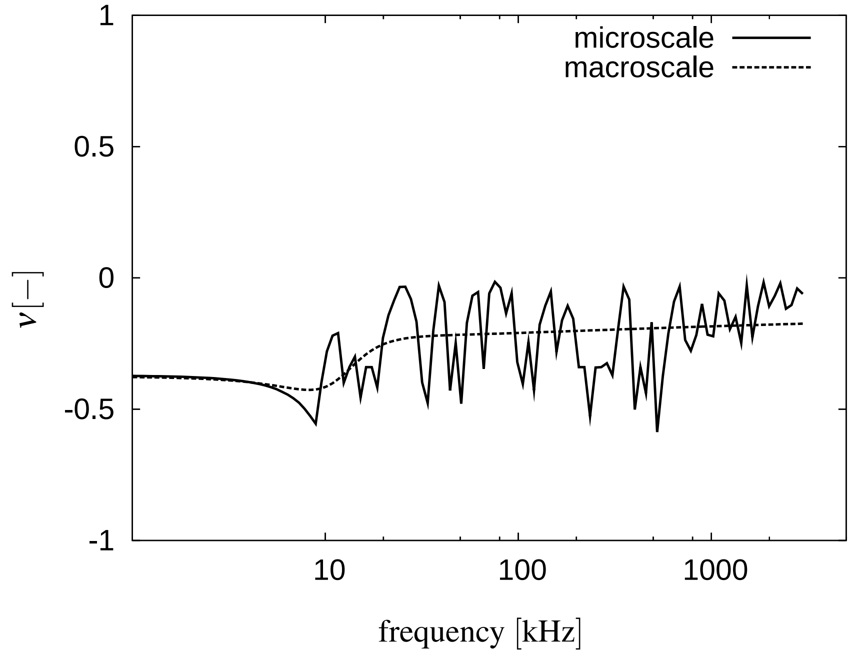

Figure 7.11: Poisson’s ratio for auxetic microstructure

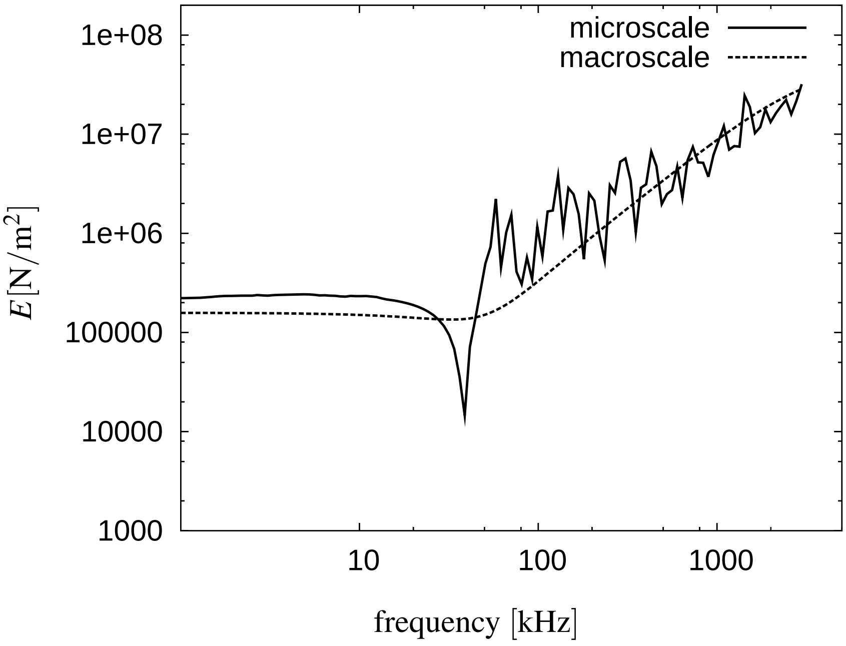

Figure 7.12: Young’s modulus for non-auxetic microstructure

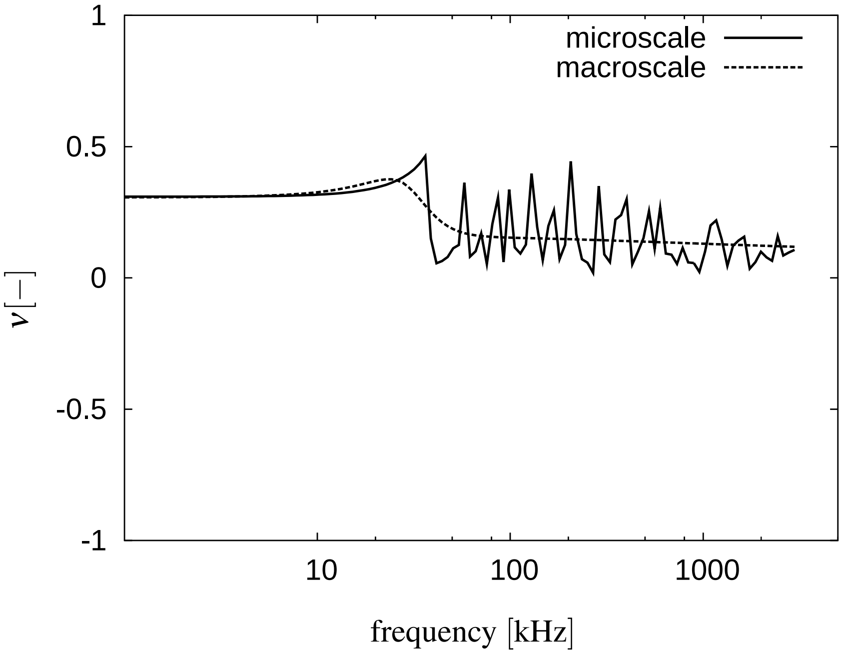

Figure 7.13: Poisson’s ratio for non-auxetic microstructure

Young's modulus

k	$\bar{E}$	p_k	q_k	α_k
1	$2.560 \cdot 10^{4}$	$2.358 \cdot 10^{-6}$	$1.842 \cdot 10^{-8}$	$1.057 \cdot 10^{0}$
2		$2.432 \cdot 10^{-8}$	$1.448 \cdot 10^{-12}$	$1.099 \cdot 10^{0}$

Poisson's ratio

k	$\bar{\nu}$	$\tilde{p}_k$	$\tilde{q}_k$	$\tilde{\alpha}_k$
1	-0.376	$4.995 \cdot 10^{-8}$	$1.598 \cdot 10^{-8}$	$1.497 \cdot 10^{0}$
2		$1.534 \cdot 10^{-8}$	$1.162 \cdot 10^{-7}$	$1.335 \cdot 10^{0}$

Table 7.4: Obtained material parameters for auxetic material

Young's modulus

k	$\bar{E}$	p_k	q_k	α_k
1	$1.581 \cdot 10^{5}$	$1.057 \cdot 10^{-6}$	$2.666 \cdot 10^{-8}$	$1.057 \cdot 10^{0}$
2		$1.448 \cdot 10^{-12}$	$1.856 \cdot 10^{-8}$	$1.389 \cdot 10^{0}$

Poisson's ratio

k	$\bar{\nu}$	$\tilde{p}_k$	$\tilde{q}_k$	$\tilde{\alpha}_k$
1	0.307	$1.869 \cdot 10^{-11}$	$1.407 \cdot 10^{-8}$	$1.424 \cdot 10^{0}$
2		$5.147 \cdot 10^{-9}$	$8.443 \cdot 10^{-10}$	$1.573 \cdot 10^{0}$

Table 7.5: Obtained material parameters for non-auxetic material

7.3 Plate cells

Until here, a number of beam-type examples were presented in dynamics. In addtion to that, a plate in plane stress is now investigated. The same geometry as in section 6.2 is used. For comparison, a plate without a hole is calculated. The discretization of the plates are given in Figure 7.14. Again, the Boundary Element Method is used for the calculation so that only the edges of the structure have to be discretized. For the cell with the star-shaped hole, the same discretization as in statics is used with 20 elements on each of the outer edges and 10 elements on one part of the inner edge. The plate without hole only has 20 elements on each outer edge. The loading of the cells is also done accordingly to section 6.2, however, with a harmonic excitation on the left and right hand side (see Figure 7.15). The material of the plate is steel with a Young's modulus of $E = 2.1 \times 10^{11}\text{N/m}^2$ and a Poisson's ratio of 0.3.

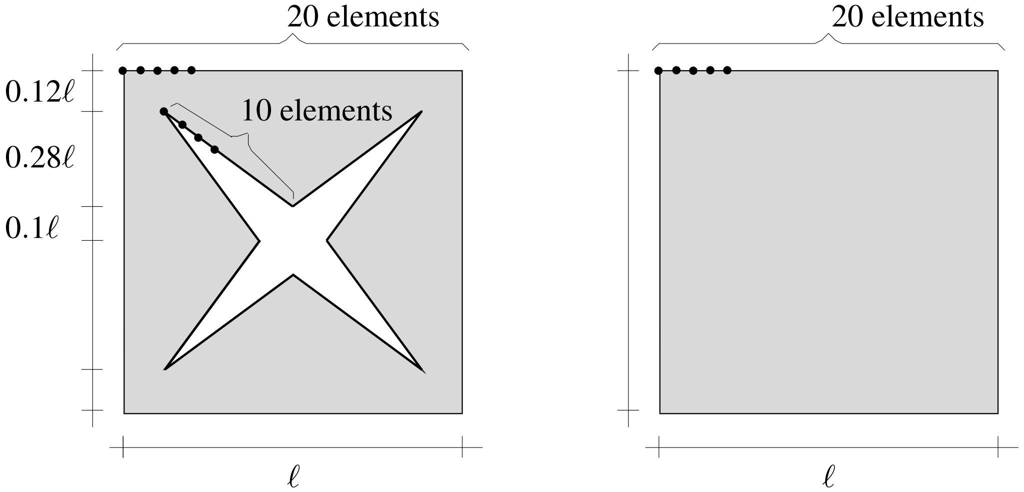

Figure 7.14: Microstructures for numerical study

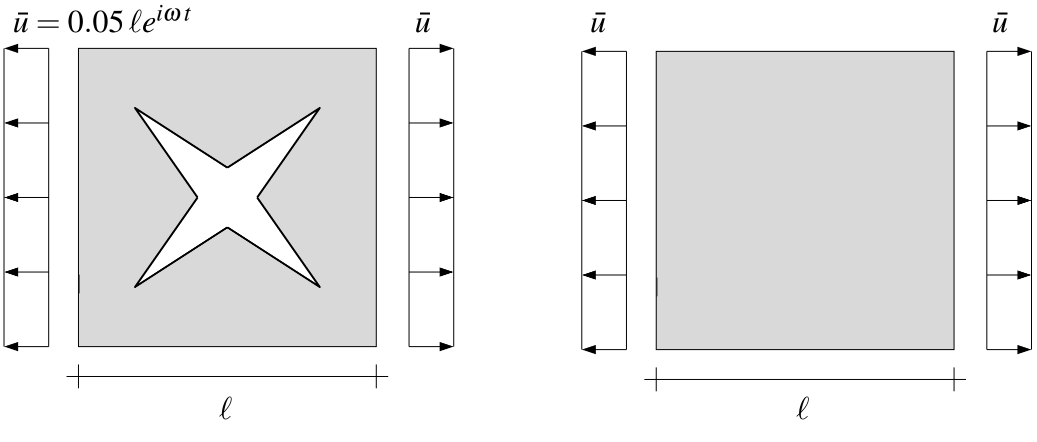

Figure 7.15: Loading of microstructures

Just like in the previous considerations, a surface averaging of the stresses and strains is done. With theses stresses and strains, Young's modulus and Poisson's ratio can be calculated on the microscale via the constitutive equation

$$\sigma_{ij}^{micro}(\omega) = \frac{E(\omega)}{(1+\nu(\omega))}\,\varepsilon_{ij}^{micro}(\omega) + \frac{\nu(\omega)E(\omega)}{(1+\nu(\omega))\,(1-2\nu(\omega))}\,\delta_{ij}\,\varepsilon_{kk}^{micro}(\omega) \tag{7.11}$$

The next step to be done is, of course, to find adequate parameters for Young's modulus and Poisson's ratio on the macroscopic scale, e.g. parameters of viscoelastic models like the ones calculated in section 7.2

$$E(\omega) = \bar{E}\frac{1+q_k(i\omega)^{\alpha_k}}{1+p_k(i\omega)^{\alpha_k}} \qquad k = 1,..,n \tag{7.12}$$

$$\nu(\omega) = \bar{\nu}\frac{1+\tilde{q}_k(i\omega)^{\tilde{\alpha}_k}}{1+\tilde{p}_k(i\omega)^{\tilde{\alpha}_k}} \qquad k = 1,..,n \quad . \tag{7.13}$$

However, the results of the microscale computation do not allow a computation of macroscopic parameters like in case of the beam-type structures. In Figures 7.16 and 7.17, both Young's modulus and Poisson's ratio on the microscale are plotted versus the frequency for the two considered microstructures.

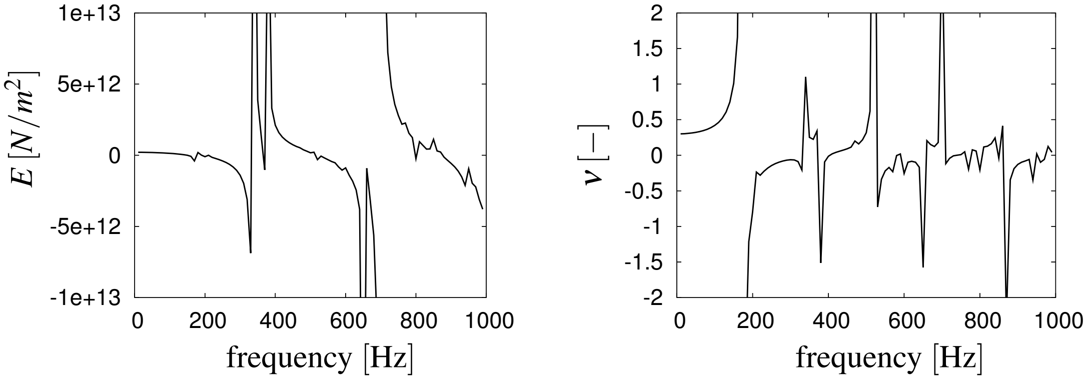

Figure 7.16: Young's modulus and Poisson's ratio on microscale for plate

It can be seen that E and ν converge to the static solution in the low frequencies. In the case of the the plate without hole, Young's modulus is $E = 2.1 \times 10^{11}\mathrm{N/m^2}$ and Poisson's ratio is $\nu = 0.3$ for frequencies close to 0, according to the input data of the plate. The plate with the star-shaped hole converges into the static solution of $E = 7.50 \times 10^{10}\mathrm{N/m^2}$ and $\nu = -0.143$ given in section 6.2. Thus, the frequency solution in the low frequency range is well confirmed.

In higher frequencies, however, all four plots expose a behavior which can not be used for a macroscopic material model. Contrary to the results of the beam-type cells, the results do not show a general tendency, i.e., they do not lie in the vicinity of a specific

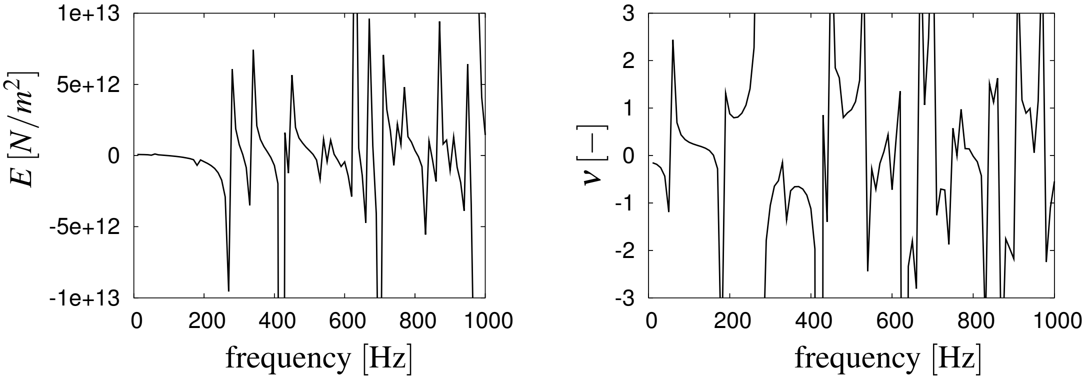

Figure 7.17: Young's modulus and Poisson's ratio on microscale for plate with hole

value. The eigenfrequencies of the structure cause an extremly oscillating course over the frequency. Physically not admissible values (e.g. $E \ll 0$, $\nu \gg 0.5$) are included in the frequency response of the structure, which makes the finding of adequate parameters of a macrocopic material model impossible or at least not meaningful.

Thus, with the proposed method which uses a frequency domain calculation and an averaging procedure of the surface values, the homogenization process can not be done for the plates. It seems that the frequency response of a plate is, because of its oszillating shape caused by the eigenfrequencies, not admissible to serve as input data for the homogenization process. A number of test calculations showed that even if a microstructure material with an extremely high damping can not improve this oszillating shape. Therefore, it must be stated that other techniques have to be developed to calculate effective properties of a plate in dynamics.

One way which could be discussed to obtain effective properties of the plate structures is the calculation of the microstructure in time domain instead of frequency domain. In this context, however, other problems arise. One problem to be solved is the finding of adequate boundary conditions for the unit cell calculation. Within the method presented in this work, the periodicity condition is fulfilled, i.e., the fact that neighboring cells behave equally can be accounted for in the microstructure calculation. In a time domain calculation, however, within the unit cell wave propagation phenomena take place, which means that periodicity can in general not be fulfilled. In addition to that, the size of the unit cell can not be varied like in the procedure given in section 4.2.5.

8 CONCLUSIONS

Virtually all materials expose a specific microstructure. The microstructure constituents of a material, of course, determine the macroscopcic properties of the material. Certain microstructures cause a material to expand on a macroscopic scale when transversely stretched and contract when transversely compressed. These materials are termed *auxetic* materials. The microstructural effect which cause this effect can be explained with simple kinematic mechanisms of beam-type microstructures. A number of auxetic materials have been fabricated. Besides the cellular microstructures, also foams with a negative Poisson's ratio have been produced.

Within the scope of this work, a new numerical procedure for the calculation of plane truss structures was developed. A big variety of computation algorithms exist for this problem. However, the proposed boundary element formulation is superior to the existing procedures with respect to accuracy since it delivers analytical exact results in statics and in frequency domain. In the context of this work, the procedure was used for the computation of the beam-type microstructures. Thus, the microstructure results are as precise as possible.

The computation of effective, macroscopic parameters of a material with a specific microstructure is termed *homogenization*. Homogenization techniques and the corresponding publications are only centered on the static case, therefore, an approach with a dynamical formulation for this problem is introduced. The calculation of the microscale is done in frequency domain, accounting for the fact that the considered materials are composed of equally shaped cells. Thus, periodicity must be preserved which is not possible in a time domain formulation because of wave propagation phenomena.

Within the proposed homogenization procedure, a numerical optimization procedure is needed to calculate effective material properties. Two gradient-based procedures, a Simplex algorithm and a SQP algorithm, were used. These optimization procedures have problems with local minima, which makes them unreliable for the given problem. Depending on the starting point of the optimization, they might run into a local minimum and only deliver poor results. A Neural Network was also applied to the homogenization problem. For a Neural Network to deliver good results, it must be trained properly. Since a very large number of training examples are needed for the training, the Neural Network is not suitable for the given problem. À priori, there is no information about the range in which the values for the material parameters lie. Thus, a very broad range of numerical values for a parameter must be covered, which makes the training extremly extensive. The most reliable results were accomplished by the Genetic Algorithm. Although the numerical cost is – compared to the gradient-based procedures – relatively high, the Genetic Algorithm delivers good, reliable results.

A number of numerical examples were presented. Effective properties in the static case were determined with the four different optimization procedures. Here, an optimization is actually not necessary, however, the optimization procedures were tested with respect to what they can accomplish. Next, the homogenization was performed in dynamics, i.e., viscoelastic material properties were determined for different microstructures. The first problem which needs to be solved for the homogenization in dynamics is the choice of a proper constitutive equation. The constitutive equation must be able to reflect microstructural effects properly. Since the behavior on the microscopic scale is frequency dependent, a viscoelastic constitutive equation was chosen. However, the choice of how many parameters are to be used is somewhat arbitrary. For a small frequency range, a total number of 14 parameters was sufficient. For a broader frequency range, a viscoelastic model with fractional derivatives and 7 parameters for Young's modulus and Poisson's ratio was sufficient. The homogenization of the plane stress microstructure could not be accomplished due to the strongly oscillating frequency response of the structure. This problem should be subject to further research.

A MATHEMETICAL PRELIMINARIES

A.1 Kronecker delta

The Kronecker Delta is defined by

$$\delta_{ij} = \begin{cases} 1 & : \quad i = j \\ 0 & : \quad \text{else} \end{cases} \tag{A.1}$$

A.2 Dirac delta distribution and Heaviside function

Sometimes it is also referred to as the unit impulse function although it is not a function as defined in the strictest mathematical sense. The Delta Dirac distribution has the property

$$\delta(x-\xi) = 0 \quad \forall x \neq \xi \quad . \tag{A.2}$$

At $x = \xi$ it has a certain value such that

$$\int_{-\infty}^{\infty} \delta(x-\xi)\mathrm{d}x = 1 \tag{A.3}$$

holds. The integral of the Dirac delta distribution is the Heaviside function.

$$H(x) = \int_{-\infty}^{x} \delta(x)\mathrm{d}x = \begin{cases} 0 & : \quad x < 0 \\ 1 & : \quad x > 0 \end{cases} \quad . \tag{A.4}$$

In Figure A.1, Dirac distribution and Heaviside function are shown for $\xi = 0$.

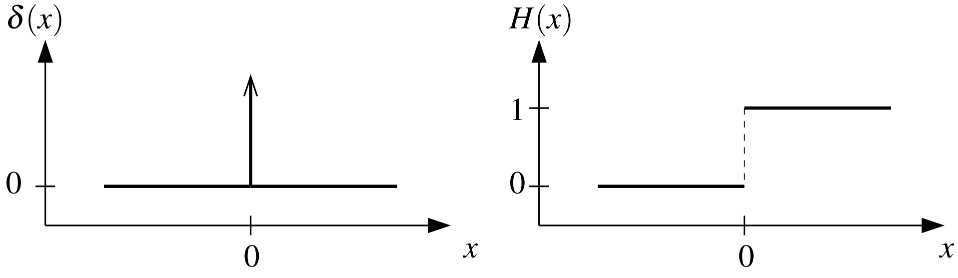

Figure A.1: Dirac delta distribution and Heaviside function

A.3 Matrix of Cofactors

The matrix of cofactors of an $n \times n$ square matrix $\mathbf{A}$ is defined as

$$\mathbf{A}^{co} = \begin{bmatrix} a_{11}^{co} & \cdots & a_{1n}^{co} \\ \vdots & \ddots & \vdots \\ a_{n1}^{co} & \cdots & a_{nn}^{co} \end{bmatrix}^T \tag{A.5}$$

where a_{ij}^{co} is the cofactor of element a_{ij} of the matrix $\mathbf{A}$. The cofactor is the determinant of the matrix with row i and column j deleted, prefixed with a sign depending on the element position, i.e.,

$$a_{ij}^{co} = (-1)^{i+j} \begin{vmatrix} a_{11} & \cdots & a_{1\,j-1} & a_{1\,j+1} & \cdots & a_{1n} \\ \vdots & \ddots & \vdots & \vdots & \ddots & \vdots \\ a_{i-1\,1} & \cdots & a_{i-1\,j-1} & a_{i-1\,j+1} & \cdots & a_{i-1\,n} \\ \\ a_{i+1\,1} & \cdots & a_{i+1\,j-1} & a_{i+1\,j+1} & \cdots & a_{i+1\,n} \\ \vdots & \ddots & \vdots & \vdots & \ddots & \vdots \\ a_{n\,1} & \cdots & a_{n\,j-1} & a_{n\,j+1} & \cdots & a_{n\,n} \end{vmatrix} . \tag{A.6}$$

One of the most important properties of the cofactor matrix is its relation to the inverse matrix

$$\mathbf{A}^{-1} = \frac{1}{\det(\mathbf{A})}\mathbf{A}^{co} \quad . \tag{A.7}$$

B FORCES AND BENDING MOMENTS OF FUNDAMENTAL SOLUTIONS

The fundamental solution $\hat{N}^*(x,\xi)$ is [21]

$$\hat{N}^*(x,\xi) = -\frac{r_{,x}}{2}\cos\left(\frac{\omega}{c_\ell}\right) \quad . \tag{B.1}$$

The shear forces and bending moments are for $\omega^2 > \kappa GA/\rho I$, i.e., $\lambda_1 < \lambda_2 < 0$

$$\begin{aligned}
\hat{Q}^*_q(x,\xi) &= \frac{r_{,x}}{2(\lambda_2-\lambda_1)}\left[\left(\lambda_1 - \frac{-\rho I\omega^2}{EI}\right)\cos(\sqrt{-\lambda_1}r)-\right. \\
&\quad \left.\left(\lambda_2 - \frac{-\rho I\omega^2}{EI}\right)\cos(\sqrt{-\lambda_2}r)\right] && \text{(B.2a)} \\
\hat{M}^*_q(x,\xi) &= \frac{-1}{2(\lambda_2-\lambda_1)}\left[\sqrt{-\lambda_1}\sin(\sqrt{-\lambda_1}r) - \sqrt{-\lambda_2}\sin(\sqrt{-\lambda_2}r)\right] && \text{(B.2b)} \\
\hat{Q}^*_m(x,\xi) &= \frac{-S_1}{2EI(\lambda_2-\lambda_1)}\left[\frac{\sin(\sqrt{-\lambda_1}r)}{\sqrt{-\lambda_1}} - \frac{\sin(\sqrt{-\lambda_2}r)}{\sqrt{-\lambda_2}}\right] && \text{(B.2c)} \\
\hat{M}^*_m(x,\xi) &= \frac{r_{,x}}{2(\lambda_2-\lambda_1)}\left[\left(\lambda_1 - \frac{\rho A\omega^2}{\kappa GA}\right)\cos(\sqrt{-\lambda_1}r)-\right. \\
&\quad \left.\left(\lambda_2 - \frac{\rho A\omega^2}{\kappa GA}\right)\cos(\sqrt{-\lambda_2}r)\right] \quad , && \text{(B.2d)}
\end{aligned}$$

and for $\omega^2 < \kappa GA/\rho I$, i.e., $\lambda_1 < 0 < \lambda_2$

$$\begin{aligned}
\hat{Q}^*_q(x,\xi) &= \frac{r_{,x}}{2(\lambda_2-\lambda_1)}\left[\left(\lambda_1 - \frac{-\rho I\omega^2}{EI}\right)\cos(\sqrt{-\lambda_1}r)-\right. \\
&\quad \left.\left(\lambda_2 - \frac{-\rho I\omega^2}{EI}\right)\cosh(\sqrt{\lambda_2}r)\right] && \text{(B.3a)} \\
\hat{M}^*_q(x,\xi) &= \frac{-1}{2(\lambda_2-\lambda_1)}\left[\sqrt{-\lambda_1}\sin(\sqrt{-\lambda_1}r) + \sqrt{\lambda_2}\sinh(\sqrt{\lambda_2}r)\right] && \text{(B.3b)} \\
\hat{Q}^*_m(x,\xi) &= \frac{-S_1}{2D_2(\lambda_2-\lambda_1)}\left[\frac{\sin(\sqrt{-\lambda_1}r)}{\sqrt{-\lambda_1}} - \frac{\sinh(\sqrt{\lambda_2}r)}{\sqrt{\lambda_2}}\right] && \text{(B.3c)} \\
\hat{M}^*_m(x,\xi) &= \frac{r_{,x}}{2(\lambda_2-\lambda_1)}\left[\left(\lambda_1 - \frac{\rho A\omega^2}{\kappa GA}\right)\cos(\sqrt{-\lambda_1}r)-\right. \\
&\quad \left.\left(\lambda_2 - \frac{\rho A\omega^2}{\kappa GA}\right)\cosh(\sqrt{\lambda_2}r)\right] \quad , && \text{(B.3d)}
\end{aligned}$$

see also [21].

The element equation (3.31) in detailed form is

$$
\left[\begin{matrix}
1-\hat{N}^*(0,0) & 0 & 0 & \hat{u}^*(0,0) & 0 & 0 \\
0 & 1-\hat{Q}_q^*(0,0) & \hat{M}_q^*(0,0) & 0 & \hat{w}_q^*(0,0) & \hat{\varphi}_q^*(0,0) \\
0 & \hat{Q}_m^*(0,0) & 1-\hat{M}_m^*(0,0) & 0 & \hat{w}_m^*(0,0) & \hat{\varphi}_m^*(0,0) \\
\hat{N}^*(0,\ell) & 0 & 0 & \hat{u}^*(0,\ell) & 0 & 0 \\
0 & \hat{Q}_q^*(0,\ell) & \hat{M}_q^*(0,\ell) & 0 & \hat{w}_q^*(0,\ell) & \hat{\varphi}_q^*(0,\ell) \\
0 & \hat{Q}_m^*(0,\ell) & \hat{M}_m^*(0,\ell) & 0 & \hat{w}_m^*(0,\ell) & \hat{\varphi}_m^*(0,\ell)
\end{matrix}\right. \cdots
$$

$$
\cdots \left.\begin{matrix}
\hat{N}^*(\ell,0) & 0 & 0 & -\hat{u}^*(\ell,0) & 0 & 0 \\
0 & \hat{Q}_q^*(\ell,0) & \hat{M}_q^*(\ell,0) & 0 & -\hat{w}_q^*(\ell,0) & -\hat{\varphi}_q^*(\ell,0) \\
0 & \hat{Q}_m^*(\ell,0) & \hat{M}_m^*(\ell,0) & 0 & -\hat{w}_m^*(\ell,0) & -\hat{\varphi}_m^*(\ell,0) \\
1+\hat{N}^*(\ell,\ell) & 0 & 0 & -\hat{u}^*(\ell,\ell) & 0 & 0 \\
0 & 1+\hat{Q}_q^*(\ell,\ell) & \hat{M}_q^*(\ell,\ell) & 0 & -\hat{w}_q^*(\ell,\ell) & -\hat{\varphi}_q^*(\ell,\ell) \\
0 & \hat{Q}_m^*(\ell,\ell) & 1+\hat{M}_m^*(\ell,\ell) & 0 & -\hat{w}_m^*(\ell,\ell) & -\hat{\varphi}_m^*(\ell,\ell)
\end{matrix}\right]
\begin{bmatrix}
\hat{u}(0) \\ \hat{w}(0) \\ \hat{\varphi}(0) \\ \hat{N}(0) \\ \hat{Q}(0) \\ \hat{M}(0) \\ \hat{u}(\ell) \\ \hat{w}(\ell) \\ \hat{\varphi}(\ell) \\ \hat{N}(\ell) \\ \hat{Q}(\ell) \\ \hat{M}(\ell)
\end{bmatrix}
$$

$$
= \int\limits_0^\ell
\begin{bmatrix}
\hat{u}^*(x,0) & 0 & 0 \\
0 & \hat{w}_q^*(x,0) & \hat{\varphi}_q^*(x,0) \\
0 & \hat{w}_m^*(x,0) & \hat{\varphi}_m^*(x,0) \\
\hat{u}^*(x,\ell) & 0 & 0 \\
0 & \hat{w}_q^*(x,\ell) & \hat{\varphi}_q^*(x,\ell) \\
0 & \hat{w}_m^*(x,\ell) & \hat{\varphi}_m^*(x,\ell)
\end{bmatrix}
\begin{matrix}
\hat{n}(x) \\ \hat{q}(x) \\ \hat{m}(x)
\end{matrix}
\; dx \quad . \tag{B.4}
$$

C CUBIC LAGRANGE ELEMENT MATRIX

In [30], the following stiffness matrix for a Timoshenko beam element is derived

$$\mathbf{K}_{element} = \begin{bmatrix} 12\Psi & -12\Psi & -6\ell\Psi & -6\ell\Psi \\ -12\Psi & 12\Psi & 6\ell\Psi & 6\ell\Psi \\ -6\ell\Psi & 6\ell\Psi & \ell^2(1+3\Psi) & \ell^2(-1+3\Psi) \\ -6\ell\Psi & 6\ell\Psi & \ell^2(-1+3\Psi) & \ell^2(1+3\Psi) \end{bmatrix} \quad , \tag{C.1}$$

with the element length ℓ and the shear factor

$$\Psi = \frac{1}{1+12\frac{EI}{\ell^2 \kappa GA}} \quad . \tag{C.2}$$

The Timoshenko element turns into an Euler-Bernoulli element if the shear factor is set to $\Psi = 1$.

D MATERIAL DATA FOR PMMA

The following material data were measured at the PTB (Physikalisch-Technische Bundesanstalt) in Braunschweig.

k	$E_k[N/m^2]$	$G_k[N/m^2]$	$b_k[s^{-1}]$
0	$3.393 \cdot 10^9$	$1.316 \cdot 10^9$	$0.000 \cdot 10^0$
1	$8.147 \cdot 10^8$	$1.913 \cdot 10^8$	$8.813 \cdot 10^0$
2	$5.143 \cdot 10^8$	$1.214 \cdot 10^8$	$9.535 \cdot 10^1$
3	$2.535 \cdot 10^8$	$6.245 \cdot 10^7$	$4.036 \cdot 10^2$
4	$2.172 \cdot 10^8$	$3.804 \cdot 10^7$	$1.843 \cdot 10^3$
5	$4.819 \cdot 10^7$	$1.946 \cdot 10^7$	$9.014 \cdot 10^3$
6	$1.562 \cdot 10^8$	$2.180 \cdot 10^8$	$9.859 \cdot 10^3$
7	$1.473 \cdot 10^7$	$2.548 \cdot 10^7$	$7.642 \cdot 10^4$
8	$1.508 \cdot 10^8$	$2.229 \cdot 10^8$	$9.484 \cdot 10^4$

REFERENCES

[1] H. Altenbach, J. Altenbach, and J. Rikards. *Einführung in die Mechanik der Laminat- und Sandwichtragwerke*. Deutscher Verlag für Grundstoffindustrie, Stuttgart, 1996.

[2] S. Alvermann, H. Antes, and M. Schanz. Vibrations of plane frames. In R. Gallego and M.H. Aliabadi, editors, *Advances in Boundary Element Techniques IV*, pages 225–230, London, 2003.

[3] H. Antes. Fundamental solution and integral equations for timoshenko beams. *Computers & Structures*, 81:383–396, 2003.

[4] K.J. Bathe. *Finite-Elemente Methoden*. Springer Verlag, Berlin Heidelberg New York, 2002.

[5] H. Böhm. Introduction to continuum micromechanics. *Course notes for CISM course on Mechanics of Microstructured Materials*, pages 1–39, 2003.

[6] N. Chan and K.E. Evans. Fabrication methods for auxetic foams. *Journal of Materials Science*, 32:5945–5953, 1997.

[7] C.P. Chen and R.S. Lakes. Dynamic wave dispersion and loss properties of conventional and negative poisson's ratio polymeric cellular materials. *Cellular Polymers*, 8:343–369, 1989.

[8] C.P. Chen and R.S. Lakes. Dynamic wave dispersion and loss properties of conventional and negative poisson's ratio polymeric cellular materials. *Cellular Polymers*, 8:343–369, 1989.

[9] A. H.-D. Cheng and H. Antes. On free space green's function for high order helmholtz equations. *Proc. IABEM91, Boundary Element Methods*, 1:67–71, 1992.

[10] J.B. Choi and R.S. Lakes. Design of a fastener based on negative Poisson's ratio foam adapted. *Cellular Polymers*, 10:205–212, 1991.

[11] R.M. Christensen. *Theory of Viscoelasticity*. Academic Press, New York, San Francisco, London, 1st edition, 1971.

[12] G.R. Cowper. The shear coefficient in Timoshenko's beam theory. *Journal of Applied Mechanics*, 33:335–340, 1966.

[13] C. Döbert. *Meso-Makromechanische Modellierung von Faserverbundwerkstoffen mit Schädigung*. Dissertation, Universität Hannover, Hannover, 2001.

[14] K.E. Evans and A. Alderson. Auxetic materials: Functional materials and structures from lateral thinking! *Advanced Materials*, 12:617–628, 2000.

[15] K.E. Evans and K. L. Alderson. Auxetic materials: the positive side of being negative. *Engineering Science and Education Journal*, 9:148–154, 2000.

[16] P. Fleming and R.C. Purshouse. Evolutionary algorithms in control systems engineering: a survey. *Control Engineering Practice*, 10:1223–1241, 2002.

[17] W. Flügge. *Vislo-elasticity*. Springer Verlag, Berlin, Heidelberg, New York, 2nd edition, 1976.

[18] C. Geiger and C. Kanzow. *Theorie und Numerik restringierter Optimierungsaufgaben*. Springer-Verlag, Berlin, 2002.

[19] D. Gross, W. Hauger, W. Schnell, and P. Wriggers. *Technische Mechanik 4 Hydromechanik, Elemente der Höheren Mechanik, Numerische Methoden*. Springer, Berlin, Heidelberg, New York, 3nd edition, 1999.

[20] D. Gross and Th. Seelig. *Bruchmechanik mit einer Einführung in die Mikromechanik*. Springer-Verlag, Berlin, Heidelberg, New York, 2001.

[21] M. Schanz H. Antes and S. Alvermann. Dynamic analyses of plane frames by integral equations for bars and timoshenko beams. *Journal of Sound and Vibration*, 276:807–836, 2004.

[22] E.P. Hadjigeorgiou and G.E. Stavroulakis. The use of auxetic materials in smart structures. *Computational Methods in Science and Technology*, 10:147–160, 2004.

[23] Z. Hashin. Analysis of composite materials - a survey. *Journal of Applied Mechanics*, 50:481–504, 1983.

[24] J. Hohe. *Elastizitätsverhalten von Sandwich-Zellkernen und zweidimensionalen Modellschäumen*. Shaker Verlag, Aachen, 2003.

[25] J. Hohe and W. Becker. A mechanical model for two-dimensional cellular sandwich cores with general geometry. *Computational Materials Science*, 19:108–115, 2000.

[26] J. Hohe and W. Becker. An energetic homogenisation procedure for the elastic properties of general cellular sandwich cores. *Composites: Part B*, 32:185–197, 2001.

[27] J. Hohe and W. Becker. Effective stress-strain relations for two-dimensional cellular sandwich cores: Homogenization, material models, and properties. *Applied Mechanics Reviews*, 55:61–87, 2002.

[28] L. Hörmander. *Linear Partial Differential Operators*. Springer, Berlin, 1963.

[29] K.L. Alderson and V.R. Simkins. Us. patent no. 6878320. http://www.freepatentsonline.com/6878320.html.

[30] K. Knothe and H. Wessels. *Finite Elemente, Eine Einführung für Ingenieure*. Springer, Berlin, Heidelberg, 2nd edition, 1992.

[31] R.C. Koeller. Applications of fractional calculus to the theory of viscoelasticity. *Journal of Applied Mechanics*, 51:299–307, 1984.

[32] R. Lakes. Materials with structural hierarchy. *Nature*, 361:511–515, 1993.

[33] R.S. Lakes. Making negative poisson's ratio foam. http://silver.neep.wisc.edu/ lakes/PoissonRecipe.html.

[34] R.S. Lakes. Foam structures with a negative poisson's ratio. *Science*, 235:1038–1040, 1987.

[35] C. Lees, J. F. V. Vincent, and J. E. Hillerton. Poisson's ratio in skin. *Biomed. Mat. Eng.*, 1:19–23, 1991.

[36] A. Lowe and R.S. Lakes. Negative poisson's ratio foam as seat cushion material. *Cellular Polymers*, 19:157–167, 2000.

[37] S. Nemat-Nasser and M. Hori. *Micromechanics: overall properties of heterogeneous materials*. North-Holland, Amsterdam, 1993.

[38] B. Nolte, S. Kempfle, and I. Schäfer. Does a real material behave fractionally? applications of fractional differential operators to the damped structure borne sound in viscoelastic solids. *Journal of Computational Acoustics*, 11:451–489, 2003.

[39] D.W. Overaker and A.M. Cuitiño. Elastoplastic micromechanical modeling of two-dimensional irregular convex and nonconvex (re-entrant) hexagonal foams. *Journal of Applied Mechanics, ASME*, 65:748–757, 1998.

[40] J.M. Parkinson and D. Hutchinson. An investigation into the efficiency of variants of the simplex metod. In F.A. Lootsma, editor, *Numerical Methods For Non-linear Optimization*, pages 115–136, London and New York, 1972.

[41] A. Reuss. Berechnung der fließgrenze von mischkristallen auf grund der plastiztätsgrenze für einkristalle. *Zeitschrift für Angewandte Mathematik und Mechanik*, 9:49–58, 1929.

[42] R.J. Roark. *Formulas for Stress and Strain*. McGraw-Hill, 3rd edition, 1954.

[43] M. Ruzzene, L. Mazzarella, P. Tsopelas, and F. Scarpa. Wave propagation in sandwich plates with auxetic core. *Journal of Intelligent Material Systems and Structures*, 13:587–597, 2002.

[44] M. Ruzzene and F. Scarpa. Control of wave propagation in sandwich beams with auxetic core. *Journal of Intelligent Material Systems and Structures*, 14:443–453, 2003.

[45] M. Schanz and H. Antes. A boundary integral formulation for the dynamic behavior of a Timoshenko beam. In M. Denda, M.H. Aliabadi, and A. Charafi, editors, *Advances in Boundary Element Techniques II*, pages 475–482, Geneva, 2001. Hoggar.

[46] A. Schmidt and L. Gaul. Bestimmung des komplexen elastizitätsmoduls eines polymers zur identifikation eines viskoelastischen stoffgesetzes mit fraktionalen zeitableitungen. *Journal*, 1:1–1, 2000.

[47] C.W. Smith, J.N. Grima, and K.E. Evans. A novel mechanism for generating auxetic behavior in reticulated foams: missing rib foam model. *Acta materialia*, 48:4349–4356, 2000.

[48] P. Spellucci. *Numerische Verfahren der nichtlinearen Optimierung*. Birkhäuser Verlag, Basel, 1993.

[49] G.E. Stavroulakis, M. Engelhardt, M. Schanz, and H. Antes. Defect identification in 3-d elastostatics using a genetic algorithm. *Optimization and Engineering*, 7:63–79, 2006.

[50] The Numerical Algorithms Group. Nag c library 2006.

[51] P.S. Theocaris, G.E. Stavroulakis, and P.D. Panagiotopoulos. Negative poisson's ratios in composites with star-shaped inclusions: a numerical homogenization approach. *Archive of Applied Mechanics*, 67:274–286, 1997.

[52] S.P. Timoshenko. On the correction for shear of the differential equation for transverse vibrations of prismatic bars. *Philisophical Magazine*, 41(6):744–746, 1921.

[53] S.P. Timoshenko. *Strength of Materials*, volume I. Van Nostrand Comp., New York, 2nd edition, 1940.

[54] T.C.T. Ting and T. Chen. Poisson's ratio for anisotropic elastic materials can have no bounds. *The quarterly journal of mechanics and applied mathematics*, 58:73–82, 2005.

[55] D. R. Vermda and R. A. Wertman. Mechanical characteristics of skin-finite deformation. *Journal of Biomechanics*, 3:111–124, 1970.

[56] W. Voigt. über die beziehung zwischen den beiden elastizitätskonstanten isotroper körper. *Wiedmanns Annalen der Physik und Chemie*, 38:573–587, 1889.

[57] J. L. Williams and J. L. Lewis. Properties and an anisotropic model of cancellous bone form the proximal tibial epiphysis. *Journal of Biomechanical Engineering*, 104:50–56, 1982.

[58] O.C. Zienkiewicz. *Methode der finiten Elemente*. Hanser Verlag, München, 1984.

[59] T.I. Zohdi and P. Wriggers. Computational micro-macro material testing. *Archives of Computational Methods in Engineering*, 8:131–228, 2001.

[60] T.I. Zohdi and P. Wriggers. *Lecture Notes in Applied and Computational Mechanics 20: Introduction to Computational Micromechanics*. Springer-Verlag, Berlin, Heidelberg, New York, 2004.

Monographic Series TU Graz

Computation in Engineering and Science

Volume 1
Steffen Alvermann
Effective Viscoelastic Behaviour of Cellular Auxetic Materials
2008, *ISBN 978-3-902465-92-4*

Volume 2
Sendy Fransiscus Tantono
The Mechanical Behavior of a Soilbag under Vertical Compression
2008, *ISBN 978-3-902465-97-9*

Volume 3
Thomas Rüberg
Non-conforming FEM/BEM Coupling in Time Domain
2008, *ISBN 978-3-902465-98-6*